



Fluid-mediated element cycling in subducted oceanic lithosphere: The orogenic serpentinite perspective

Thomas Pettke^{*}, Annette Bretscher

University of Bern, Institute of Geological Sciences, Baltzerstrasse 3, CH-3012 Bern, Switzerland

ARTICLE INFO

Keywords:

Subduction zones
Serpentinite
Geochemistry
Fluid mobile trace elements
Dehydration fluids
Metamorphic petrology

ABSTRACT

Serpentinites are central to water (re)cycling in subduction zones and thus effect fluid-mediated element transfer between the hydrosphere and the Earth's mantle and back into continental crust via calcalkaline magmatism. Diverse and often controversial models exist on the relevance of various source contributions to the budget of fluid mobile elements of hydrous peridotites and how these evolve during the subduction cycle. This work offers novel constraints on ongoing debates. We present a comprehensive bulk rock and silicate mineral major to trace element study covering the antigorite dehydration reaction based on Cerro del Almirez antigorite-serpentinites and chlorite-harzburgites, including the systematics of As, Sb, B, W, Li, In, Tl, Bi, Cd, and Sn - so far unavailable for Almirez, and there exist only few such data for orogenic serpentinites in general. We integrate these with reviewed literature data and develop a general model for the geochemical systematics of subducting hydrous slab mantle covering magmatic peridotite conditioning, element enrichment upon oceanic hydration, compositional evolution with progressive subduction to peak temperature antigorite dehydration, and retrograde metasomatism upon exhumation.

Pre-hydration magmatic processes produce strong compositional variations on centimetre to metre to kilometre scales. Serpentinisation via seawater and sediment-equilibrated pore fluids produces highly variable fluid-mobile element (FME) bulk rock enrichments in B, As, Sb, W, Cs, \pm Li, \pm Bi, \pm Pb, \pm U exceeding primitive mantle concentrations. Hydration enrichment numbers represent a novel concept introduced in this work to refine the extent of hydration-mediated FME enrichment. They represent the measured ratio of fluid-mobile element over a fluid-immobile element of closely comparable magmatic compatibility normalised to its corresponding primitive mantle abundance ratio. Hydration enrichment numbers are highest for Sb and As (up to 650) and lowest for Ba and Rb (down to 0.06) for Almirez data, quantifying fractions of minimal enrichment (values >1) and minimal prograde subduction loss (values <1). FME enrichment occurred primarily in ocean floor to trench to shallow forearc settings where sediment-equilibrated pore fluids are relevant, while addition from deeper sediment metamorphic dehydration fluids with progressive subduction is subordinate at best. Prominent fractions of As, Sb, B, Rb, Sr, Cs, Ba, Pb, Zn, Cl, Br, Li, Na, K, and Ca are then lost to the fluid upon serpentinite dehydration including the antigorite-out reaction. We find no evidence in support of significant fluid-mediated element addition (e.g., Th, U, Ta, Sr, Pb, Cs, Rb, Li) upon antigorite dehydration as has been postulated in literature by simple comparison between Atg-serpentinite and Chl-harzburgite coexisting at Almirez. Magmatic pre-conditioning prior to serpentinisation can account for the differences in HFSE between Atg-serpentinite and Chl-harzburgite, while prominent FME addition upon retrogression as measured on retrograde serpentine and talc is demonstrated for Cs, Pb, Sr and Ba, thus adulterating bulk rock systematics for certain FME.

This work concludes that oceanic serpentinisation dominates the FME imprint of subducting slab serpentinites and that progressive subduction goes along with successive FME loss. We propose that serpentinites from fluid-dominated, highly hybridised and oxidised plate interface melange materials displaying spectacular FME enrichments with a sedimentary flavour are distinctly overrepresented in our sample record. Therefore, the combined data set of hydrous peridotites from Almirez and Erro Tobbio may offer a more representative compositional estimate of the bulk mass of subducted slab serpentinite, to be used in modelling of the geochemical impact of serpentinite-derived matter on fluid-mediated chemical cycling in subduction zones.

^{*} Corresponding author.

E-mail address: pettke@geo.unibe.ch (T. Pettke).

<https://doi.org/10.1016/j.earscirev.2021.103896>

Received 23 August 2021; Received in revised form 6 December 2021; Accepted 13 December 2021

Available online 16 December 2021

0012-8252/© 2021 The Authors.

Published by Elsevier B.V. This is an open access article under the CC BY-NC-ND license

(<http://creativecommons.org/licenses/by-nc-nd/4.0/>).

1. Introduction

Serpentinites play a major role in the fluid-mediated element cycling in subduction zones, owing to their capacity of carrying prominent masses of mineral lattice-bound water along with fluid mobile elements (FME) to depths well exceeding 50 km (e.g., Ulmer and Trommsdorff, 1995; Scambelluri et al., 1995, 2004a, 2014, 2019; Scambelluri and Philippot, 2001; Rüpke et al., 2004; Hattori and Guillot, 2007; Kendrick et al., 2011, 2013; Deschamps et al., 2013). Upon serpentinite dehydration (primarily brucite-out, antigorite-out, and chlorite-out reactions), up to ~12 wt% H₂O (depending on the degree of initial hydration) along with FME are released, to eventually trigger arc magmatism via flux melting in the overlying mantle wedge (e.g., Spandler and Pirard, 2013), to likely aid in metasomatising lithospheric mantle portions (e.g., Downes, 2001), and to affect rheological and seismic properties of the subducting slab and the slab to wedge interface, as well as the dynamics of UHP rock exhumation (e.g., Hermann et al., 2000; Guillot et al., 2015; Agard et al., 2018).

The geochemical cycle related to serpentinites, from their formation on the ocean floor to modifications during early subduction stages to partial or complete dehydration deep down in subduction zones has recently become much better constrained (e.g., Scambelluri et al., 2001, 2004a, 2004b, 2014, 2015, 2019; Hattori and Guillot, 2003, 2007; Deschamps et al., 2010, 2011, 2012, 2013; Kodolányi and Pettke, 2011; Kodolányi et al., 2012; Kendrick et al., 2011, 2013; Andreani et al., 2013; Marchesi et al., 2013; Debret et al., 2013; Lafay et al., 2013; Barnes et al., 2014; Kahl et al., 2015; Cannao et al., 2015, 2016; Klein et al., 2014, 2017; Peters et al., 2017, 2020; Schwarzenbach et al., 2018a, 2018b; Gilio et al., 2019, 2020; Albers et al., 2020). This work has identified a series of FME characteristic for serpentinites and anhydrous silicates crystallised upon prograde metamorphism, most importantly B, As, Sb, U, W, Cs, Li, and the halogens. These elements often occur at concentrations much higher than primitive mantle (PM) in hydrated mantle rocks showing variably depleted compositions prior to hydration (e.g., Niu, 2004). A large fraction of these FME are incorporated upon ocean floor hydration at mid ocean ridge (MOR), passive margin, and trench to forearc settings (e.g., Kodolányi et al., 2012, and references therein); however, prominent element addition may also occur during initial subduction stages (e.g., Hattori and Guillot, 2007; Deschamps et al., 2011; Debret et al., 2013; Lafay et al., 2013; Scambelluri et al., 2014; Cannao et al., 2015, 2016), notably for rocks lining the subduction plate interface. With progressive subduction, serpentinites undergo specific mineral transformations all associated with aqueous fluid, and elements are redistributed between the coexisting product fluid and mineral phases. Investigations focusing on the B cycle have revealed that ocean floor hydration causes orders of magnitude B enrichments in product serpentine (lizardite - chrysotile; e.g., Thompson and Melson, 1970; Kodolányi et al., 2012) and that upon the transformations of (i) lizardite - chrysotile to antigorite ± H₂O, (ii) brucite + antigorite decomposition to olivine + chlorite + H₂O, and (iii) final antigorite decomposition to olivine + orthopyroxene ± chlorite + H₂O, significant fractions of B are lost to the aqueous fluid phase (e.g., Scambelluri et al., 2004a, 2004b; Tenthorey and Hermann, 2004; Kodolányi and Pettke, 2011; Deschamps et al., 2011). Nevertheless, a prominent B enrichment is still preserved in nominally anhydrous (Mg, Fe)-silicates formed from antigorite dehydration (e.g., Scambelluri et al., 2004b; Tenthorey and Hermann, 2004) that can be recycled to the convecting mantle. The B example illustrates the trace element serpentinite cycle that is largely controlled by B uptake on the ocean floor and its redistribution during progressive subduction to subarc depths and beyond.

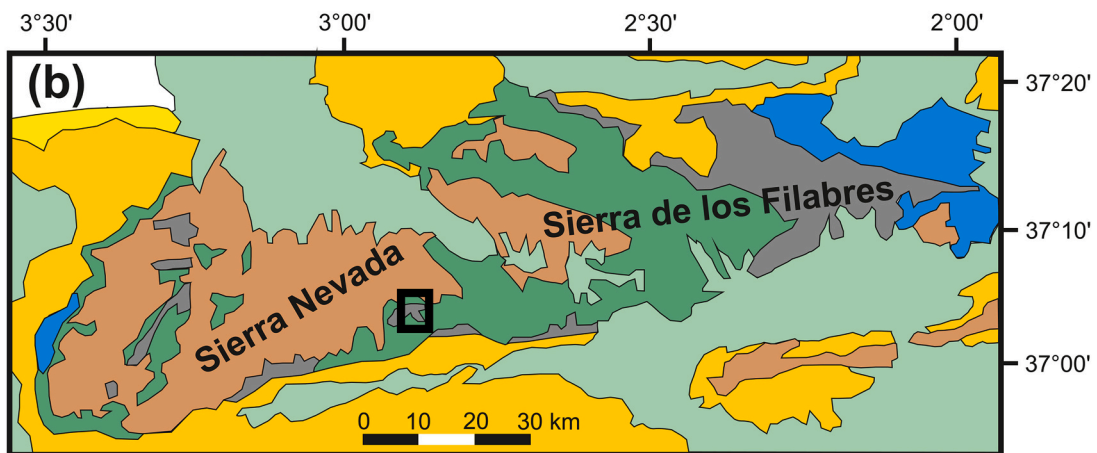
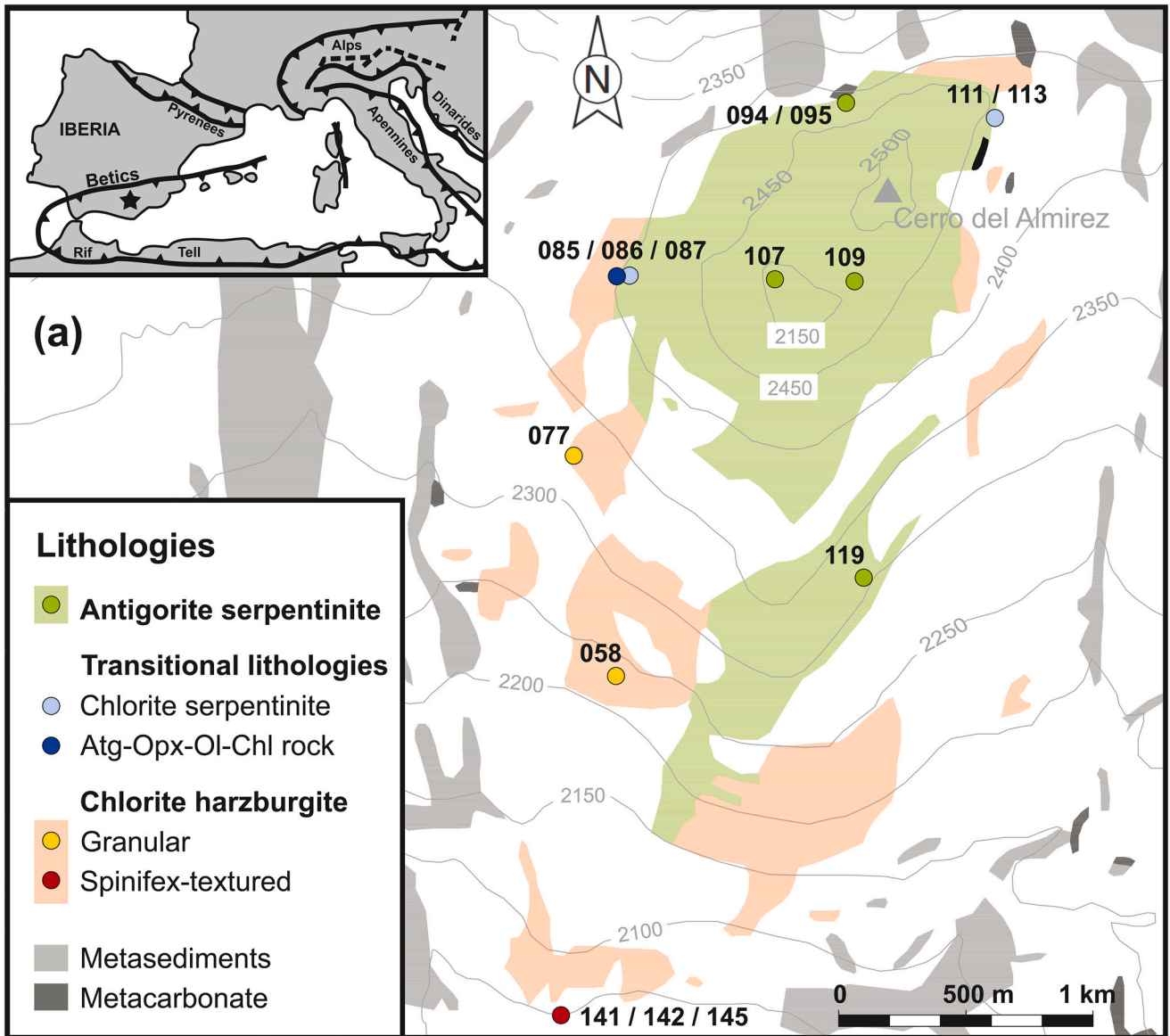
The two chalcophile elements As and Sb also display characteristic enrichments in serpentinites; however, their chemical cycle is more complex and less well constrained. Importantly, chalcophile elements may be prominently added upon serpentinitisation on the ocean floor (e.g., Kodolányi et al., 2012; Andreani et al., 2014) as well as during early

stages of subduction where serpentinites equilibrate with aqueous fluids that obtained their chemical inventory from prior exchange with sediments (e.g., black shales) entrained along the subduction channel (e.g., Hattori and Guillot, 2007; Deschamps et al., 2011; Lafay et al., 2013; Scambelluri et al., 2014). A compilation of data for serpentinites from diverse geotectonic settings (ocean floor, subduction) has revealed orders of magnitude element concentration variations (Deschamps et al., 2013), thus documenting the great diversity of serpentinite geochemical compositions. Part of this variability originates from the commonly complex pre-serpentinitisation magmatic history of melt extraction and refertilization by melt-rock reactions (e.g., Niu, 2004), and additional variability is produced upon ocean floor serpentinitisation. While concentrations and systematics for lithophile elements (e.g., the rare earth elements, REE) are well constrained, the systematics of notably some chalcophile elements have remained vaguely understood, both on bulk rock and individual mineral scales. This is in part due to analytical difficulties, including polyatomic interferences, instrumental memory issues, as well as sometimes poorly constrained standard reference material (SRM) element concentrations (most recently e.g., Peters and Pettke, 2017). Consequently, which phases are most important in controlling for example the As and Sb cycling has remained poorly constrained, but evidence points towards important contributions of both hydrated silicate as well as possibly sulphide phases. Moreover, linking chalcophile and lithophile element systematics at bulk rock and mineral scales has often not been attempted rigorously.

This paper offers a comprehensive assessment of the major to trace element systematics of orogenic serpentinites, from magmatic melt depletion to refertilization followed by oceanic hydration and by progressive subduction transformation to peak antigorite breakdown, and selective refertilization upon retrogression. We use the terminology of hydration and dehydration throughout the manuscript in order to emphasize the perspective of metamorphic mineral reactions that control element distribution between minerals and aqueous fluids involved. Bulk rock and mineral trace element budgets then offer insights into (i) the diverse types of metasomatism involved, (ii) the mineral sinks for specific trace elements, (iii) at which stages of the progressive subduction evolution a given element may be lost to dehydration fluids that may eventually trigger calcalkaline magmatism, and (iv) which trace element enrichments may be carried down into and metasomatise convecting mantle portions.

The hydrous mantle rock units at Cerro del Almirez (Betic Cordillera, S-Spain) offer a unique natural opportunity to document and quantify the geochemistry of a body of oceanic high-pressure antigorite serpentinite (Atg-serpentinite) and coexisting chlorite harzburgite (Chl-harzburgite) formed via antigorite dehydration. Comprehensive bulk rock and petrologically well controlled in-situ mineral compositional data are presented in this work, with an emphasis on elements for which data are globally scarce, and generally unavailable for Almirez, including As, Sb, B, Tl, Bi, W, Li, Mo, Cd, In, and Sn. Integrating literature data with our new data we document the prominent impact of magmatic refertilization prior to oceanic serpentinitisation as well as retrogression upon exhumation on the trace element systematics. We propose to quantify element enrichments upon hydration on individual sample scales, rather than inter-sample comparisons as done so far, via hydration enrichment numbers that are highest for As, Sb, B, W, and Cs for the present sample suite. Hydration enrichment numbers are then used to better constrain extents of element enrichment upon hydration (oceanic versus early subduction) and of element loss with progressive dehydration during subduction. Regarding the often proposed sedimentary FME source input to serpentinites, we argue that sedimentary pore fluids are relevant as opposed to metamorphic sediment dehydration fluids that seem subordinate except for a few plate interface melange settings.

Our synthesis then places the Almirez case into an oceanic lithosphere scale setting, offering a conceptual model that accounts for the great compositional diversity of subducted, hydrated mantle rocks and their variable fluid-rock interaction histories during the subduction and



(caption on next page)

Fig. 1. (a) Geological outcrop map of the largest ultramafic rock body and its enclosing paragneisses at Cerro del Almirez, Spain (based on Schönbächler, 1999). The inset shows the Almirez location (black star) in the framework of the Alpine orogeny. Colour-coded dots and numbers represent ultramafic rock samples (Alm06-XXX; Table 1) investigated in this study. Modified after Bretscher et al. (2018). (b) Medium-scale geological map of the Nevado-Filábride Complex, the lowermost tectonometamorphic unit of the Internal Zones of the Betic Cordillera (southern Spain). The black box identifies the location of Almirez, enlarged in figure (a). Simplified after Padrón-Navarta et al. (2011). (For interpretation of the references to colour in this figure legend, the reader is referred to the web version of this article.)

exhumation cycle. We finally propose that the extensive, combined data set for Almirez (this work) and Erro Tobbio (Peters et al., 2020), characteristic of a typical slow-spreading oceanic lithosphere, may serve as a model geochemical reservoir of average subducted slab serpentinite, to be used in future modelling of subduction zone geochemical cycling.

2. Geological setting and metamorphic evolution of ultramafic rock types

The hydrous mantle rock units at Cerro del Almirez belong to the Nevado-Filábride Complex, the lowermost tectonometamorphic unit of the Internal Zones of the Betic Cordillera (southern Spain; Fig. 1). In a larger scale they are part of the Betic Ophiolite Association showing exhumed slices of the slow-spreading Piemont-Ligurian Ocean which dominated the paleogeographic setting prior to Alpine oceanic subduction (Trommsdorff et al., 1998; Puga et al., 1999). The ultramafic rock units consist of ~200 m thick foliated Atg-serpentinites underlain by ~200 m thick Chl-harzburgites, embedded in metasediments (metapelites, metacarbonates, marbles, gneisses; Fig. 1; compare Schönbächler, 1999), locally associated with ophicarbonates (Menzel et al., 2019).

Breakdown of antigorite at eclogite facies conditions (670 °C and ~1.6 GPa, Bretscher et al., 2018; 1.6–1.9 GPa and 680–710 °C, Padrón-Navarta et al., 2010; ≤695 °C, ≤2.0 GPa, López Sánchez-Vizcaíno et al., 2005) was driven by Alpine subduction in the middle Miocene as revealed by U-Pb zircon ages of 15.0 ± 0.6 Ma in meta-clinopyroxenite from Cerro del Almirez (López Sánchez-Vizcaíno et al., 2001). An oceanic origin of the Almirez hydrous mantle rocks is evidenced by the occurrence of meta-rodinities (e.g., Trommsdorff et al., 1998), by trace element systematics (e.g., Marchesi et al., 2013; Peters et al., 2017), and by bulk rock H, C, O, S isotopic compositions (Alt et al., 2012).

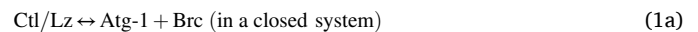
The Almirez massif consists of 3 ultramafic bodies, the largest hydrous mantle rock outcrop measuring 1.1×2.5 km (Fig. 1) from where our samples originate. The lithologies at Cerro del Almirez are spectacular because they preserve the high-pressure antigorite dehydration reaction as a tectonically non-disturbed contact between Atg-serpentinites and Chl-harzburgites (Trommsdorff et al., 1998; Schönbächler, 1999; Padrón-Navarta et al., 2011). This contact has recently been interpreted to represent the antigorite dehydration reaction front, imaging an oxidation front established upon serpentinisation at the ocean floor (Bretscher et al., 2018), rather than representing a classical metamorphic isograd. Specifically, it is the Mg# of reactant antigorite ($\text{Mg-number} = 100 \cdot [\text{Mg}/(\text{Mg} + \text{Fe})]_{\text{molar}}$, where all Fe is considered to be Fe^{2+}) that determined whether antigorite reacted out (low Mg#) or not (high Mg#; stable to higher temperatures). The Mg# of serpentine minerals forming upon oceanic hydration increases with increasing extent of bulk rock oxidation to a first order. This is because production of progressively more ferric iron eventually leads to magnetite crystallisation, thereby depleting coexisting serpentine minerals in Fe, thus increasing their Mg#. Major to trace element systematics of magnetite in Atg-serpentinite reveal that magnetite in these samples crystallised upon oceanic hydration and recrystallised during subduction (Vieira Duarte et al., 2021). Consequently, an Atg-serpentinite rock mass containing domains of variable bulk rock oxidation formed upon oceanic hydration will contain antigorite with variable Mg#. Because antigorite dehydration represents a continuous reaction dictated largely by antigorite Mg#, there exists a narrow temperature interval - for Almirez between circa 665 and 675 °C - where

serpentinites containing high-Mg# antigorite stably coexist with Chl-harzburgites that used to be serpentinites containing low-Mg# antigorite. Consequently, different extents of bulk rock oxidation upon oceanic hydration exerted the dominant control on whether or not antigorite dehydrated at Almirez (see Bretscher et al., 2018, for more details).

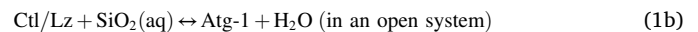
The petrology of these ultramafic rocks has been documented in detail previously (Trommsdorff et al., 1998; Schönbächler, 1999; López Sánchez-Vizcaíno et al., 2005; Padrón-Navarta et al., 2010, 2011; Marchesi et al., 2013; Bretscher et al., 2018; Vieira Duarte et al., 2021). Samples analyzed here for their geochemical systematics correspond to those characterised in detail in Bretscher et al. (2018); hence, only a brief summary is provided here. The sequence of prograde rock types across the antigorite dehydration reaction front is Atg-serpentinite → Chl-serpentinite → Atg-Opx-Ol-Chl-rock → Chl-harzburgite (nomenclature after Padrón-Navarta et al., 2011; mineral abbreviations after Whitney and Evans, 2010). Meta-ophicarbonates (Menzel et al., 2019) associated locally were not considered for this study. Rocks with macroscopically minimal retrograde overprint formed during uplift and exhumation were chosen; however, retrogression of the rocks is variably prominent and will be addressed separately below.

The prograde metamorphic evolution of Almirez rocks covers the formation of metamorphic antigorite, olivine, clinopyroxene, and tremolite along with magnetite recrystallisation in the Atg-serpentinite, onset of antigorite recrystallisation (chlorite-in), followed by continuous antigorite breakdown producing olivine, orthopyroxene, chlorite, and even magnetite (for thin section images of our samples refer to Bretscher et al., 2018; and Vieira Duarte et al., 2021, for oxides and sulphides). Fig. 2 summarises the successive mineral crystallisation stages, mineral assemblages, and the corresponding prograde and retrograde mineral reactions (red numbers; not balanced).

Prograde reactions are:



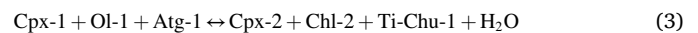
(“Antigorite-in”, e.g., Evans, 2004)



(“Antigorite-in”, e.g., Evans, 2004)



(“Olivine-in” or “brucite-out”; after Trommsdorff and Evans, 1974)



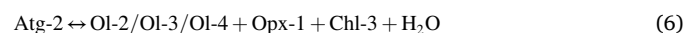
(Formation of metamorphic clinopyroxene; after Trommsdorff and Evans, 1980)



(Formation of tremolite; after Trommsdorff and Evans, 1974)



(“Chlorite-in”; after Padrón-Navarta et al., 2011)



(“Orthopyroxene-in” or “antigorite-out”; after Trommsdorff et al., 1998)

And the retrograde reactions are:



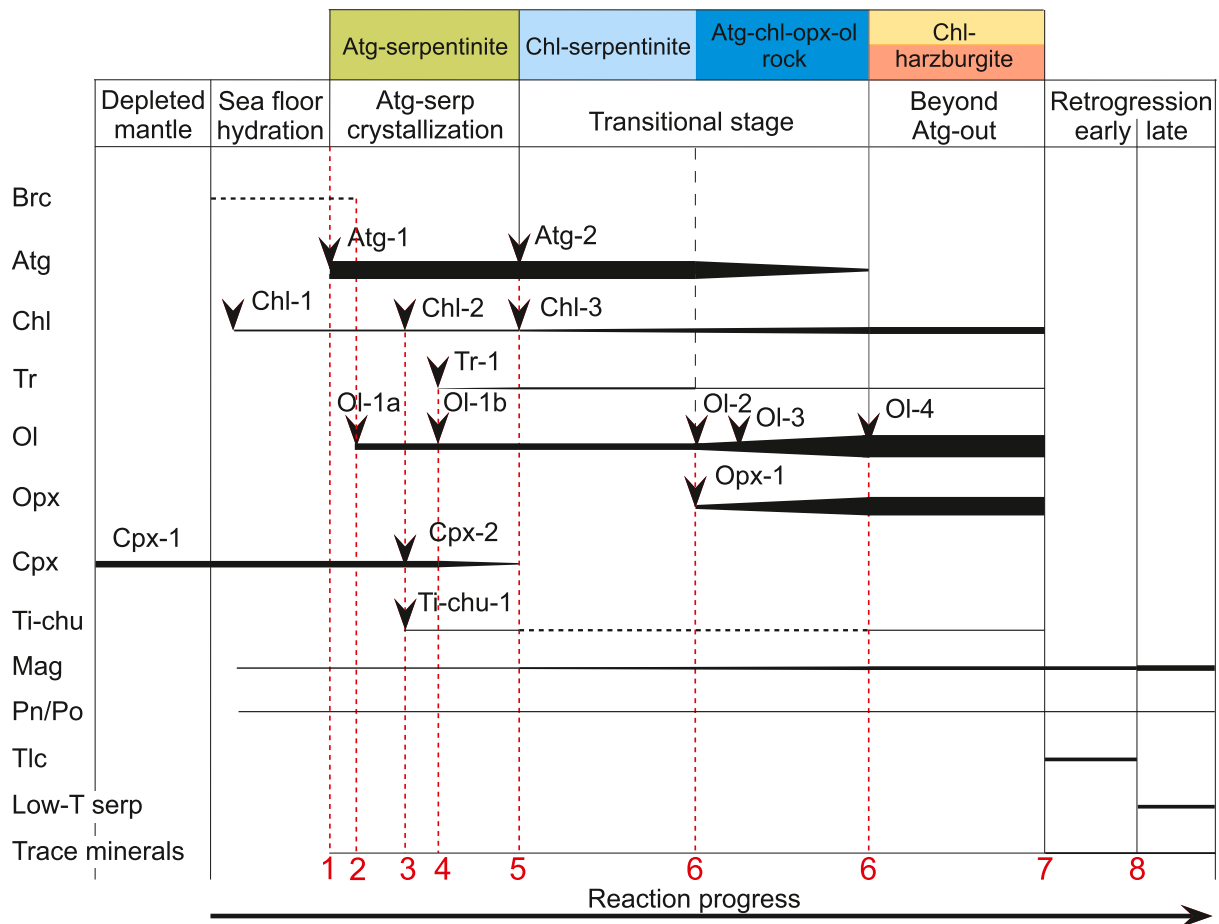


Fig. 2. Schematic prograde mineral crystallisation stages of ultramafic rocks at Almirez (based on [Bretscher et al., 2018](#), and [Vieira Duarte et al., 2021](#)). First appearance of a mineral is marked with an arrowhead and labelled. Thicknesses of the lines are proportional to average modal abundances of the minerals (compare [Table 1](#)). Dashed lines indicate stability of the respective minerals but they were not observed in our samples. Retrogression is split into early and late, emphasizing that retrogression occurred until final exhumation of the ultramafic bodies. Trace phases are often retrograde petrographically and include isolated, small grains of ilmenite (some of which belong to the prograde mineral assemblages), hematite, pyrite, chalcopyrite, sulphates, carbonates, and phosphates ([Vieira Duarte et al., 2021](#)) and are not separated here for simplicity. Numbers 1 to 8 refer to metamorphic reactions explained in the text. Olivine 1a and 1b are produced in different prograde reactions but cannot be distinguished in thin section. Colour coding in the figure header is that used in data plots throughout the manuscript (for Chl-harzburgites separating the spinifex-textured and granular variants). Mineral abbreviations are after [Whitney and Evans \(2010\)](#). (For interpretation of the references to colour in this figure legend, the reader is referred to the web version of this article.)

(Formation of retrograde talc; after [Trommsdorff and Evans, 1974](#))



(Formation of retrograde, yellow, low-T serpentine)

Of the prograde mineral reactions, reactions 1, 2, and 6 are most relevant.

Weakly to strongly foliated At-serpentinites predominate over massive ones, and olivine and magnetite modes vary significantly ([Table 1](#); [Vieira Duarte et al., 2021](#)). Atg-serpentinites consist of antigorite, porphyroblastic olivine, sometimes relic clinopyroxene with clear prograde recrystallization rims, rare tremolite, magnetite clots rarely associated with chlorite, pentlandite (SEM-EDX), Ti-clinohumite, and traces of Fe—Ti oxides (SEM-EDX) and pyrrhotite. Dusty clinopyroxene (Cpx-1) is the only relic mantle mineral, showing occasional magnetite lamellae. Magnetite (up to 500 µm clusters) occurs dispersed throughout the antigorite matrix. Ti-clinohumite (Ti-Chu-1) forms small grains dispersed throughout the matrix and is overgrown by antigorite blades. Rare olivine-titanoclinohumite-magnetite veins representing prograde fluid circulation pathways are also observed (compare [López Sánchez-Vizcaíno et al., 2005](#)).

The up to ~1 m thick contact zone between Atg-serpentinite and Chl-harzburgite (compare with [Padrón-Navarta et al., 2011](#)) documents

antigorite breakdown and is characterised by Chl-serpentinites and Atg-Opx-Ol-Chl rocks displaying gradual contacts that are oblique to regional foliation. This contact zone documents a stepwise antigorite dehydration process. Variably foliated antigorite from Atg-serpentinite (Atg-1) recrystallises into coarser and randomly oriented antigorite (Atg-2) associated with chlorite (Chl-3; “chlorite-in”) to produce Chl-serpentinite. Atg-2 then decomposes continuously across the temperature interval between orthopyroxene-in and antigorite-out, covering less than 15 °C at ca. 660 °C ([Bretscher et al., 2018](#); their Fig. 8). Tremolite and Ti-clinohumite remained stable across the antigorite dehydration reaction, while clinopyroxene was never observed in transitional rocks nor in Chl-harzburgite. The main differences between the Chl-serpentinite and the subsequent Atg-Opx-Ol-Chl rock are (i) the appearance of orthopyroxene (Opx-1), (ii) abundant flaky chlorite not overgrown by antigorite (Chl-3, in addition to subordinate Chl-3-Atg-2 intergrowths with thin Atg-rims), (iii) reduction in Atg-content to below 10 vol-% along with disappearance of fine-grained antigorite (Atg-1), and (iv) the development of a locally granular texture. Variable modes of magnetite and pentlandite occur along with ±pyrrhotite and ± ilmenite in all lithologies ([Vieira Duarte et al., 2021](#)).

Chl-harzburgite occurs in two distinct textural appearances, as granular and spinifex-textured, massive rocks ([Trommsdorff et al., 1998](#);

Schönbächler, 1999; Puga et al., 1999; Ruiz Cruz et al., 1999). Both textural varieties share an identical mineralogy devoid of antigorite, with only slightly variable modal abundances of olivine, orthopyroxene, and chlorite. Magnetite persists throughout along with pentlandite and traces of ilmenite, hemo-ilmenite and ilmeno-hematite, and magnetite is even produced across the antigorite dehydration reaction (Vieira Duarte et al., 2021). The spatial distribution of granular and spinifex-textured Chl-harzburgite relative to the contact with Atg-serpentinite is not systematic except for the fact that granular rocks are more abundant near the contact to Atg-serpentinites. Transitions between granular and spinifex-textured Chl-harzburgites can occur across a few centimetres. Trommsdorff et al. (1998) reported granoblastic Ti-clinohumite several mm in size in the Chl-harzburgites, typically associated with chlorite, Cr-magnetite, and ilmenite, and López Sánchez-Vizcaíno et al. (2005) document 3 textural varieties of Ti-clinohumite in the Chl-harzburgite sequence. A few coarse magnesite crystals in equilibrium with olivine and orthopyroxene were observed in granular Chl-harzburgite Alm06-077.

Retrogression of the peak mineral assemblages encompasses a sequence of retrograde mineral crystallisation and primarily affected Chl-harzburgites while Atg-serpentinites largely escaped it (compare Vieira Duarte et al., 2021). Early retrograde features include talc pseudomorphically replacing orthopyroxene or progressively consuming it along grain boundaries and cleavage planes (Fig. 3g in Bretscher et al., 2018). Talc also occurs interstitially between chlorite-antigorite intergrowths in Chl-serpentinite where it replaces Atg-2 as indicated by irregular grain boundaries between the two minerals. Inclusions of orthopyroxene and olivine in euhedral tremolite were confirmed by RAMAN spectroscopy, thus documenting that some tremolite also crystallised during retrogression. Wormy exsolutions of hematite occur in grain centres of ilmenite (Vieira Duarte et al., 2021). Talc also occurs along diffuse veins and crack fillings penetrating the rock where it is associated with yellow serpentine, oxides (mostly magnetite), sulphides, and rare sulphates (barite). Olivine in Chl-harzburgite often shows domains with yellow mesh serpentine associated with microcrystalline magnetite.

3. Analytical techniques

Samples with minimal weathering were analyzed by optical microscopy based on thin sections with a standard thickness of $\sim 30 \mu\text{m}$, and mineral identification was assisted by scanning electron microscopy (SEM-EDX) and RAMAN spectroscopy. Mineral modes were obtained by point counting and then refined for some samples based on bulk rock major element compositions. Clinopyroxene abundance was adjusted to fit the measured CaO content (Atg-serpentinites), the major hydrous phases antigorite (Atg-serpentinites) and chlorite (Chl-harzburgites) were adjusted to fit the measured Al_2O_3 concentrations, and the abundances of the hydrous phases were varied to better correspond to the measured loss on ignition (LOI). Ti-clinohumite was added to the mineral assemblage, even if it was not observed in every thin section, in order to better fit the measured concentrations of Nb, Ta, and Ti. Mineral modes are presented for 15 samples in Table 1.

3.1. Bulk rock compositions

Bulk rock chemical analysis was performed with laser ablation (LA-) ICP-MS on pressed powder pellets (PPP) following procedures detailed in Peters and Pettke (2017) and Garbe-Schönberg and Müller (2014). For the fabrication of the pellets the sawing and weathering surfaces of the samples were chipped away. After crushing the samples to obtain fragments smaller than 5 mm they were dry milled with a RETSCH 250 ml agate planetary ball mill and subsequently wet milled with a RETSCH 50 ml agate planetary ball mill, in order to obtain a $\sim 1 \mu\text{m}$ sample powder. The powder was then mixed with a binder (microcrystalline cellulose), and pressed to pellets of 10 mm diameter and $\sim 1 \text{ mm}$

thickness. Pellets were measured by LA-ICP-MS at conditions outlined below for mineral compositions. Data were reduced employing SILLS (see below) by normalizing to 100 wt% major element oxides minus volatile content ($\text{H}_2\text{O} + \text{CO}_2$) as determined by LOI obtained by heating the dried sample powder at 1050°C during 1.5 h.

3.2. Mineral compositions

Major element concentrations of the rock forming minerals were determined by electron probe microanalysis (EPMA) using a JEOL JXA-8200 instrument at the Institute of Geological Sciences, University of Bern. The acceleration voltage was 15 keV and the beam current 20 nA. Beam sizes were $1 \mu\text{m}$ for olivine, orthopyroxene, and Ti-clinohumite, $3 \mu\text{m}$ for clinopyroxene, 5 or $10 \mu\text{m}$ for chlorite, antigorite, and tremolite, and $10 \mu\text{m}$ for talc. Natural or synthetic silicate and oxide minerals were used as standards. A PhiRhoZ routine was used for matrix correction.

Mineral trace element measurements were conducted by LA-ICP-MS with a Geolas Pro 193 nm ArF excimer laser system coupled to an ELAN DRC-e quadrupole ICP-MS instrument at the Institute of Geological Sciences, University of Bern. Instrument optimization procedures, analytical strategies and data reduction closely followed those outlined in Pettke et al. (2012). Beam sizes were chosen as large as possible (up to $160 \mu\text{m}$) to lower the limits of detection (LOD), which were calculated for each analyte and each measurement spot individually following the formulation detailed in Pettke et al. (2012). External standardization was against the glasses SRM610 and 612 from NIST or GSD-1G from USGS, employing values from GeoRem, V18 (2021) and those reported in Peters and Pettke (2017). Internal standardization used major element concentrations determined by EPMA on mineral grains of the same textural position. Data reduction was done with the SILLS program (Guillong et al., 2008).

Ablation rates were tuned to about $0.15 \mu\text{m}$ per pulse at $\sim 5 \text{ J cm}^{-2}$ fluence via attenuation of the laser output beam; the laser repetition rate was 10 Hz. Background intervals were about 1 min, and signal intervals were manually set such as to avoid potential contributions from surface dirt and/or inclusions. Uncertainties on the external measurement reproducibility are of the order of 1–2% (2SD, on GSD-1G) unless signal intensities were low, where counting statistics uncertainties may increase to a few tens of percent near the respective LODs. Measurements of SRM 610 or 612 or GSD-1G served to check for analytical accuracy of mineral measurements, lacking perfectly characterised mineral standards. Deviations from reference values in our study are comparable to those reported for pressed powder pellet bulk rock measurements (Peters and Pettke, 2017). Note that these deviations are much less than the range in compositions documented for minerals of the same textural position and for bulk rocks and therefore not significant for the geological interpretations presented here.

4. Results

Element concentration data were acquired for major to trace elements, with emphasis on trace elements for which data for orogenic serpentinites are scarce in the literature in general and no data exist so far for Almiraz ultramafic rocks, namely As, Sb, B, Tl, Bi, W, Li, In, Cd, and Sn.

4.1. Bulk rock major to trace elements

Major to trace element bulk rock data (53 elements) are reported in Table A1 and illustrated in Figs. 3 and 4. These 15 samples cover all lithotypes across the antigorite-out reaction. Rock water contents as determined by loss on ignition (LOI) at the general absence of carbonate decrease across the antigorite-out reaction, from up to 11.3 wt% H_2O in Atg-serpentinites down to 4.1 wt% H_2O in Chl-harzburgites.

Hydrous mantle bulk rock compositions at Cerro del Almiraz span a broad compositional range from near lherzolititic to harzburgitic/dunitic

Table 1
Sample list and mineral abundances.

Lithology	Subtype	Sample	Texture	UTM coordinates	Modal abundances of minerals (vol%), from point counting											
					Opaque ^a	Atg	Chl	Tr	Ol ^b	Opx	Cpx ^b		Ti-Chu	Tlc	Cb ^c	Srp ^d
											Relic	Metam.		Retrog.		Retrog.
Atg-Serpentinite	With relic and metamorphic Cpx	Alm06-094	Foliated	508,035 / 4,105,134	4	57	1	–	26	–	6	5	0.4	–	–	1
		Alm06-107	Foliated	507,909 / 4,104,834	3	56	x	x	24	–	9	7.6	–	–	–	1
		Alm06-109 ^e	Foliated	508,049 / 4,104,825	2	72	2	–	12	–	3.6	8	0.2	–	–	1
	Cpx-free	Alm06-119 ^e	Massive	508,052 / 4,104,304	1	64	–	1	28	–	–	4	0.3	–	–	1
		Alm06-095 ^e	Foliated	508,035 / 4,105,134	3	89	–	0.4	7	–	–	–	0.3	–	–	1
Chl-serpentinite		Alm06-085	Foliated	507,704 / 4,104,828	2	52	9	5	14	–	–	–	–	7	–	11
		Alm06-111	Foliated	508,272 / 4,105,105												
		Alm06-113	Foliated	508,272 / 4,105,105	3	55	5	7	30	–	–	–	–	–	–	1
Atg-Chl-Opx-Ol-rock		Alm06-086	Weakly foliated	507,704 / 4,104,828	6	10	10	x	46	1	–	–	–	13	–	14
		Alm06-087	Massive, granular	507,704 / 4,104,828	2	4	16	x	48	7	–	–	–	11	–	12
Chl-harzburgite		Alm06-058	Massive, granular	507,623 / 4,104,150	2	–	24	x	36	24	–	–	–	1	x	14
		Alm06-077 ^e	Massive, granular	507,540 / 4,104,530	2	–	23	0.4	22	33	–	–	0.6	9	x	11
		Alm06-141	Massive, spinifex-textured	507,589 / 4,103,527	1											
		Alm06-142	Massive, spinifex-textured	507,589 / 4,103,527	4	–	19	–	37	30	–	–	–	1	–	11
		Alm06-145 ^e	Massive, spinifex-textured	507,589 / 4,103,527	1	–	20	0.3	33	31	–	–	0.2	6	–	9

Notes: Mineral abbreviations after [Whitney and Evans \(2010\)](#).

– : not observed.

x: Observed in thin section but not detected during point counting (abundance below 0.5 vol%).

^a Mainly magnetite with minor sulphides and rare Fe-Ti-oxide (details in [Vieira Duarte et al., 2021](#)).

^b Olivine and metamorphic clinopyroxene in Atg-serpentinities were counted as one phase during point counting (due to difficulties in reliably distinguishing them). The fraction of clinopyroxene was then calculated from the bulk rock CaO, assuming that all CaO is in clinopyroxene (at absence of carbonate).

^c Rare coarse peak-metamorphic carbonate.

^d Late retrograde mesh serpentine.

^e Modal abundances refined based on measured bulk rock data.

(this work; Marchesi et al., 2013; Padrón-Navarta et al., 2011; Garrido et al., 2005; López Sánchez-Vizcaíno et al., 2005; Schönbacher, 1999). Major element data reveal that our samples are variably depleted mantle rocks with Mg# ranging between 87.7 and 90.9 (no rock-type dependent trend seen; Table A1). Some of the samples are displaced towards slightly lower MgO/SiO₂ relative to the mantle melt depletion trend in an Al₂O₃/SiO₂ vs. MgO/SiO₂ diagram, and this displacement does not correlate with bulk rock Mg# (Fig. A1). A variable CaO depletion relative to that in Al₂O₃ is observed (Bretscher et al., 2018). Relatively elevated CaO concentrations for some Atg-serpentinites correlate with elevated clinopyroxene modes (of which part is relic mantle clinopyroxene). On the other hand, no correlation is apparent between Mg# and SiO₂ concentrations.

REE data reveal variable trends for the ultramafic rocks in chondrite-normalised representation (Fig. 3a). All samples show variable, relative enrichment in LREE, variably U-shaped patterns (as often seen for oceanic and orogenic serpentinites; e.g., Paulick et al., 2006; Kodolányi et al., 2012; Deschamps et al., 2013), and variably negative Eu anomalies (except for one Atg-serpentinite) down to 0.52. Four serpentinite samples tend to increase slightly from HREE to LREE and have chondrite-normalised REE contents above 1. The three Atg-serpentinites contain relic clinopyroxene, and the Chl-serpentinite is Tr-bearing, with modest CaO depletion only, and shows a distinct negative Eu-anomaly. All other samples have subchondritic REE contents except for the HREE. These data compare well to those reported in Marchesi et al. (2013), but the U-shape of the REE pattern is more pronounced for our sample suite.

Of all trace elements Zr and Hf show the lowest PM-normalised values (Fig. 3b; also observed by Marchesi et al., 2013). Of the more incompatible elements, Rb–Ba and La–Ce show the lowest PM-normalised abundances. Incompatible elements known to be little mobile in aqueous fluids (e.g., Th, Nb, Ta, LREE) display concentration variations of up to a factor of 30, while typical FME (e.g., Cs, Rb, U, B, Pb, As, Sb; except for Ba and W) display an overall lower variability. Interestingly, some of the FME (e.g., Rb and Ba) display lower concentrations than do the fluid-immobile, incompatible HFSE (Th, Nb, Ta). Elements absolutely enriched include the lithophile elements B (8–54 PM), Cs (1.2–13 PM), Li (up to 5 PM, but no enrichment in Atg-serpentinites), sometimes U (up to 4 PM), the chalcophile elements As (5–82 PM), Sb (7–78 PM), Bi (up to 4 PM, where significantly detected),

and Pb and In for some samples, and finally the siderophile element W (1.4–33 PM). Atg-serpentinite samples without relic clinopyroxene have B and As concentrations distinctly higher than those with relic clinopyroxene, of the order of those characteristic for the partially dehydrated rocks.

For Sn, data (measured near the respective LOD of ~0.05 μg g⁻¹) suggest moderate enrichment to near-PM concentrations in some samples, notably for the Chl-harzburgite samples that tend to be higher than the Atg serpentinites. For Tl, three significant concentration data of <0.01 μg g⁻¹ were obtained, indicating approximate PM concentration levels; however, most measurements were below LOD of ~0.005 μg g⁻¹. No bulk rock data are available for Cd because of a measurement error. Beryllium was also recorded during measurement but hardly any significant data were obtained (LOD for Be ~0.08 μg g⁻¹; not reported in Table A1). Large ion lithophile elements (LILE) surprisingly show prominently different extents of enrichments, with maxima for Cs (1.2–13 PM) and minima for Rb (0.04–0.4 PM) and Ba (0.04–2 PM). The overall pattern of enrichment/depletion compares well to that reported for trench to forearc serpentinites drilled on the ocean floor (Kodolányi et al., 2012).

Trace element correlation diagrams based on concentrations and on element abundance ratios (Fig. 4, A3) reveal the following trends. Concentration trends are positive between FME (e.g., Rb vs. Cs and As vs. B). Elements plotted versus fluid immobile but incompatible Th show positive trends for Ce, Nb, In, and U, where the three spinifex-textured Chl-harzburgite samples are offset to higher U concentrations. The plot of La/Sm vs. Th/La reveals two distinct correlations, a steep slope for Atg-Opx-Ol-Chl rocks and Chl-harzburgite together with a gentle slope for Atg-serpentinite and Chl-serpentinite. No trend is observed for chalcophile elements with incompatible lithophile elements Rb, Cs, and Ba (not shown). Moreover, As vs. Sb reveals scatter, as do plots of B vs. W and Cs vs. W. Element abundance ratio trends normalised to Cs/U (not shown) reveal positive linear trends for In/U, Sn/U, Rb/U, and Li/U.

4.2. Mineral major to trace elements

EPMA and LA-ICP-MS measurements were performed on antigorite, chlorite, tremolite, olivine, orthopyroxene, clinopyroxene, and Ti-clinohumite from the prograde sequence, and on retrograde talc and

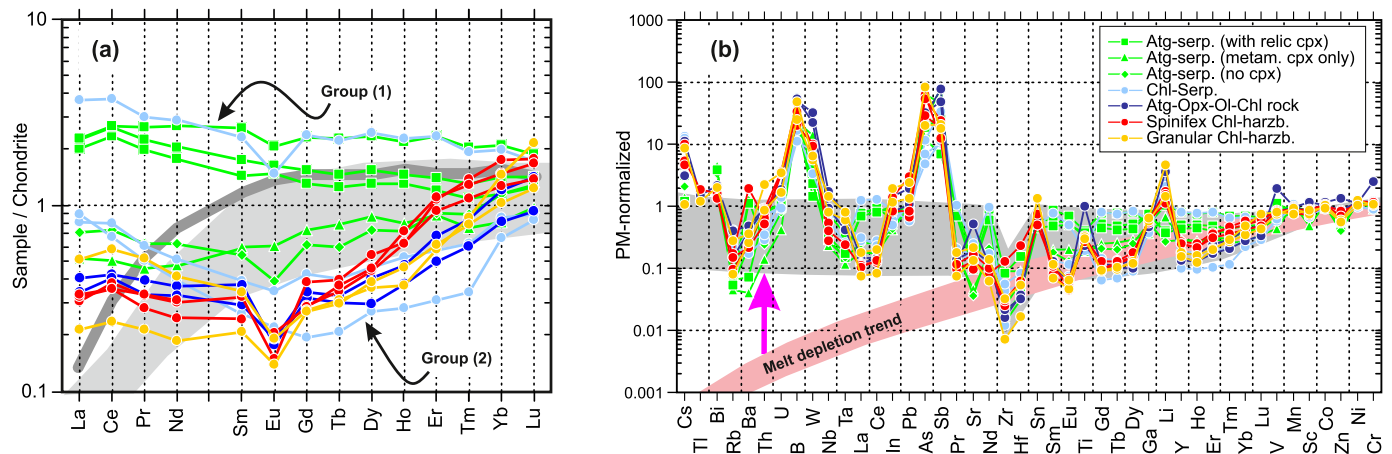


Fig. 3. Bulk rock trace element diagrams of ultramafic rocks from Almiraz. (a) Chondrite-normalised REE patterns, overlain on the grey field representing antigorite serpentinites from Erro Tobbio (Liguria; Peters et al., 2020), and the grey line represents the REE pattern of spinel peridotite VEP-2 from the Upper Platta Unit (Müntener et al., 2010), typical of a rifted continental margin with minimal melt-rock reaction overprint. Metaperidotite Groups (1) and (2) are discussed in text. (b) Primitive mantle (PM) normalised trace element distribution diagram overlain on the red band representing a mantle melt depletion trend. The grey band represents the inferred range in trace element patterns of Almiraz rocks prior to serpentinisation that reveal prominent refertilisation upon melt rock reaction (pink arrow, exemplified for the incompatible and fluid-immobile Th) following variable melt extraction. The sequence of elements on the x-axis is based on the leftwards decreasing ratio of element concentrations in depleted mantle (Salters and Stracke, 2004) to primitive mantle (Palme and O'Neill, 2014), thus approaching the mantle rock element compatibility trend (left = incompatible, right = compatible). Colour-coding refers to rock types defined in Figs. 1, 2 and will be used throughout this paper. (For interpretation of the references to colour in this figure legend, the reader is referred to the web version of this article.)

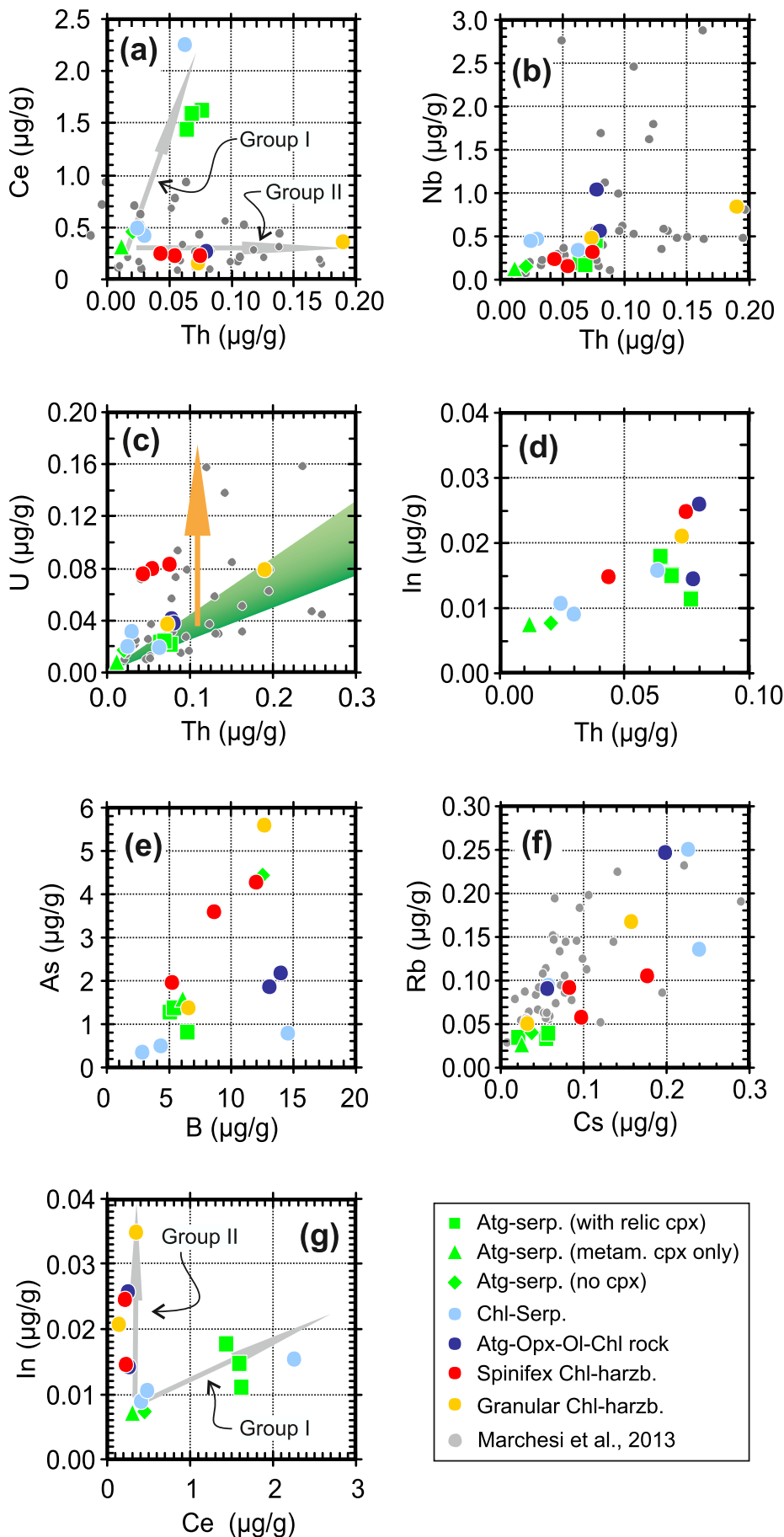


Fig. 4. Bulk rock trace element correlation diagrams. (a) Th vs. Ce, showing two trends (grey arrows) for Group I and Group II metaperidotites as defined on the basis of bulk rock REE patterns (Fig. 3a). (b) Th vs. Nb, showing an overall positive trend. (c) Th vs. U, superposed onto the Th/U depleted mantle array; the green fan spans Th/U of between 4.0 (old convecting mantle, dark green) and 2.3 (young convecting mantle, light green; e.g., Elliott et al., 1999). The orange arrow indicates the direction of pure U addition upon ocean floor peridotite hydration. (d) Th vs. In, showing a positive trend, indicating that In concentrations in the hydrous mantle rocks are strongly influenced by pre-hydration magmatic processes. (e) B vs. As, with good positive correlation notably for the Chl-harzburgites, suggesting a common hydration source. (f) Cs vs. Rb, documenting a good positive trend at variable slopes between the two alkali elements. (g) Ce vs. In, displaying again two different trends for Group I and Group II metaperidotites. Where available, published hydrous metaperidotite data for Almiraz (Marchesi et al., 2013) are given as small grey circles for comparison. (For interpretation of the references to colour in this figure legend, the reader is referred to the web version of this article.)

yellow serpentine. Major element systematics for these samples were presented in part by Bretscher et al. (2018), and we complete here their documentation where relevant. Measurement data document chemical evolutions along with successive mineral growth stages as defined in Fig. 2. PM-normalised trace element distribution diagrams (Figs. 5–7) reveal variable melt depletion and refertilization trends along with an overall comparable pattern of fluid-mobile element enrichment relative to primitive mantle concentrations, as for bulk rock compositions (Fig. 3b), indicating that these elements including the chalcophile ones are significantly hosted in rock-forming silicates. Our measurements also document that a given mineral growth stage can have highly different trace element concentrations for different rock samples. Data are now presented for hydrous minerals first, followed by olivine and the pyroxenes, and completed by retrograde talc and serpentine. The complete dataset of major and minor element mineral compositions is reported in Tables A2 to A18, and measurements containing inclusions are explicitly marked in Tables A11, A13, A15.

4.2.1. Antigorite

Successive antigorite crystallisation stages in the Atg-serpentinites and the transitional lithologies delineate a compositional range along a negative Si–Al correlation that reflects Tschermak exchange ($1.89\text{--}1.97\text{ Si pfu}$, $0.09\text{--}0.23\text{ Al pfu}$), corresponding to $39.91\text{--}44.12\text{ SiO}_2$ and $1.82\text{--}4.26\text{ Al}_2\text{O}_3$. Antigorite in transitional lithologies (Atg-1 and Atg-2) has distinctly lower Mg# than antigorite in Atg-serpentinite (Table A2). Chondrite-normalised REE patterns (Fig. 8a) reveal a variable overall LREE depletion and a negative Eu anomaly. Atg-1 from Atg-serpentinites displays progressively more pronounced U-shaped REE spectra with increasing LREE concentrations. The PM-normalised trace element distribution diagram (Fig. 5a) illustrates absolute enrichments for all antigorite growth stages in B (31–73 PM), As (10–33 PM), Sb (6–74 PM), Cs (1.4–6 PM) and Bi (up to 6 PM). Enrichments relative to

elements of similar compatibility during mantle melting are furthermore evident for U (i.e., slightly elevated U/Th), W, and Li (except Atg-1 from one Atg-serpentinite), and less prominently so for Pb. Overall, negative anomalies appear to be present for Ba, Sr, and Zr in all antigorite generations (similar to those reported by Marchesi et al., 2013). Data for Cd, where detected, range from 1.5 to 13 PM.

4.2.2. Chlorite

Chlorite compositions correspond to near Mg-endmember clinocllore. Mg# range between 93.4 and 95.5 (Table A4). The highest REE concentrations along with a U-shaped spectrum (Fig. 8b) are observed for chlorite associated with magnetite (Chl-1). LREE concentrations of prograde to peak chlorite are distinctly lower (and often below LOD) in transitional lithologies and in Chl-harzburgites. All chlorite growth stages are strongly enriched in B (7–13 PM), As (up to 33 PM), Sb (up to 17 PM), and Bi (up to 8 PM; Fig. 5b). Additionally, some chlorite generations show variable enrichments in Cs, Cr, V, and Sc. Lithium is up to two orders of magnitude enriched compared to elements of similar compatibility, Sr is generally depleted (as opposed to data from Marchesi et al., 2013). Data for Cd show concentrations of up to 9 PM.

4.2.3. Tremolite

Rare tremolite occurs in all rock types (all Tr-1) as small crystals with a Mg# of between 96 and 99.5 (Table A6). REE patterns of tremolite (Fig. 8c) are LREE depleted (HREE ≤ 10 Chondrite) for granular Chl-harzburgite and slightly convex for tremolite rimming clinopyroxene and for transitional Atg-Opx-Ol-Chl rock. All REE patterns show a variably negative Eu anomaly. Tremolite rimming relic mantle clinopyroxene displays up to one order of magnitude lower REE concentrations than the other tremolite types. Trace element enrichments in tremolite are variable for the different lithologies but prominent absolute enrichments in tremolite are evident for B (17–134 PM) in all rock types,

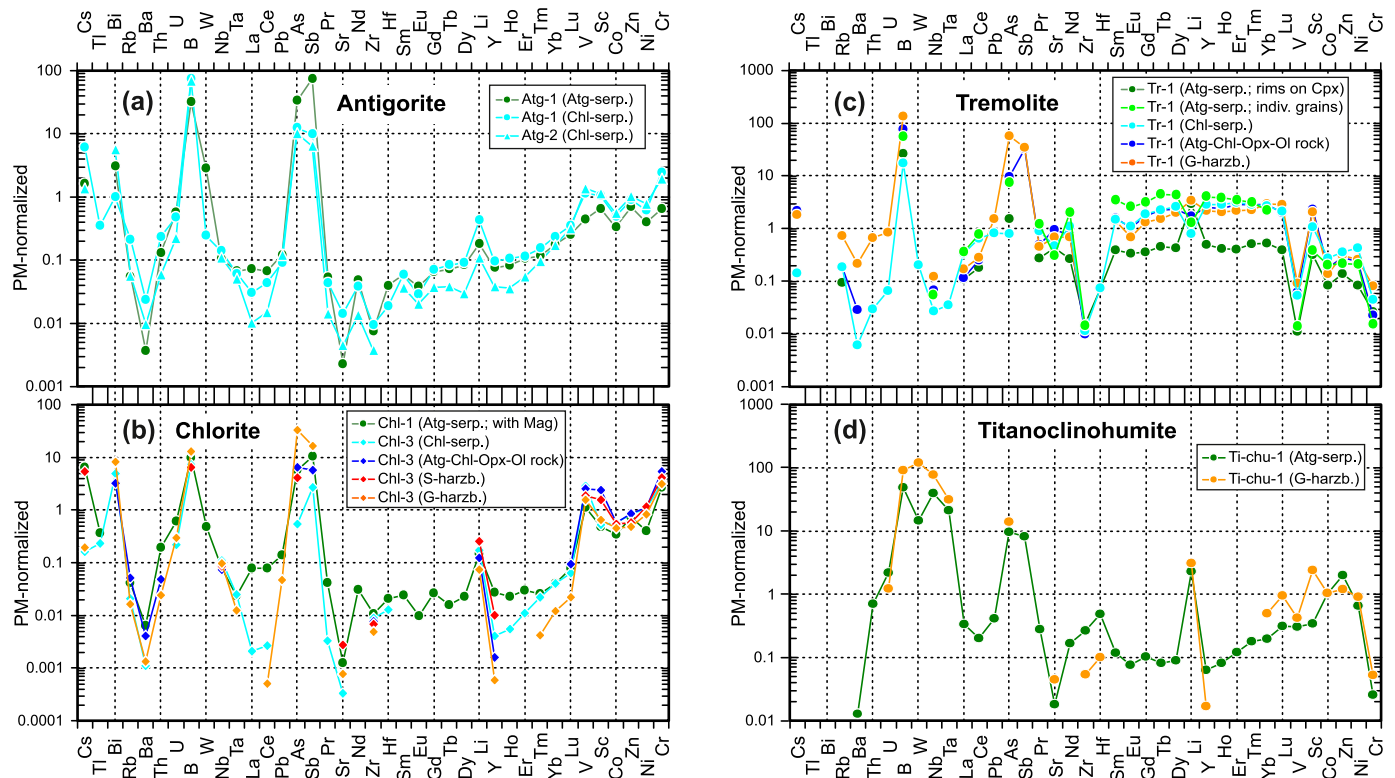


Fig. 5. Primitive mantle normalised trace element diagrams for hydrous minerals of Almirez metaperidotites. Mineral labels of the legends refer to mineral growth stages displayed in Fig. 2, complemented with textural positions where relevant. Primitive mantle (PM) values are from Palme and O'Neill (2014). Note that mineral trace element concentrations can vary significantly between different samples of the same rock type (Tables A3, A5, A7, A9), and averages for rock types are plotted here for simplicity. (For interpretation of the references to colour in this figure legend, the reader is referred to the web version of this article.)

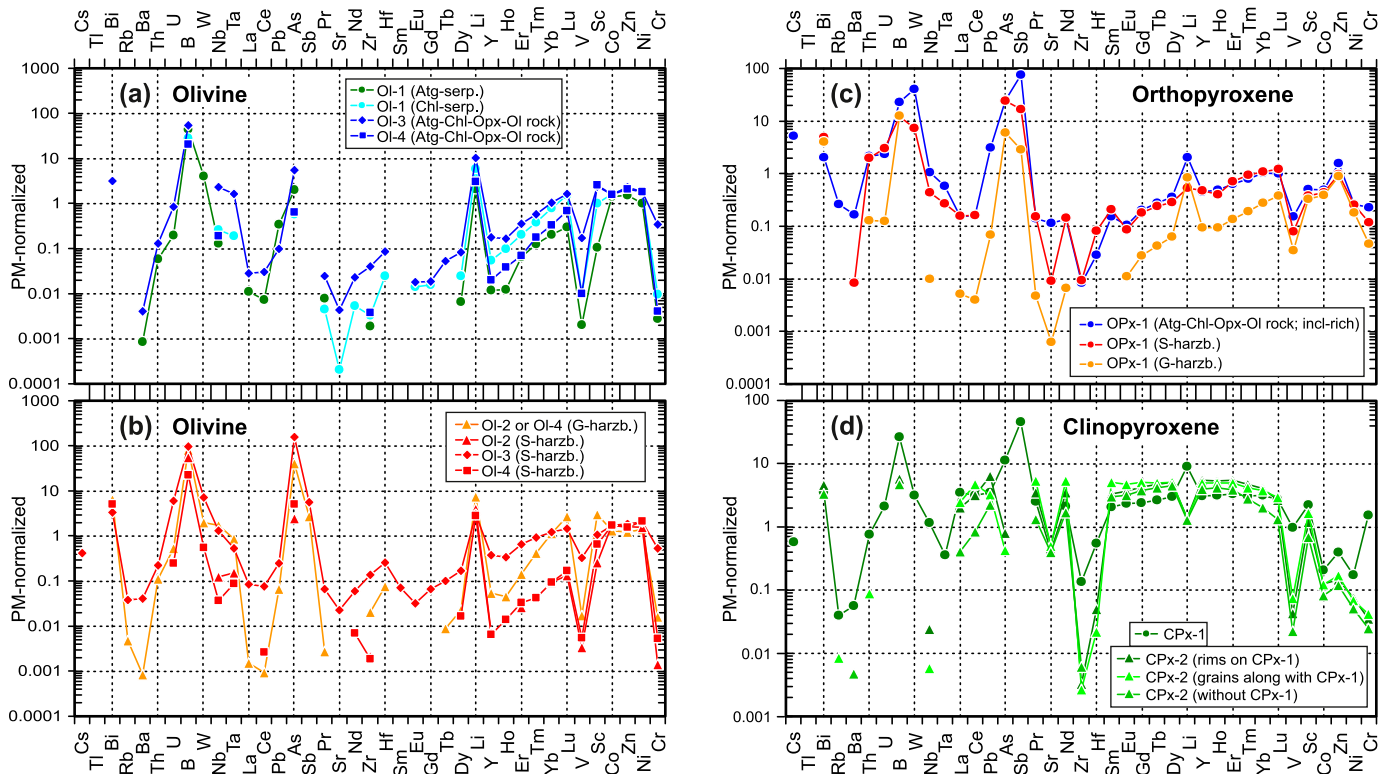


Fig. 6. Primitive mantle normalised trace element diagrams for anhydrous minerals from Almirez metaperidotites. Mineral labels of the legends refer to mineral growth stages displayed in Fig. 2, complemented with textural positions where relevant. Primitive mantle (PM) values are from Palme and O'Neill (2014). Note that mineral trace element concentrations can vary significantly between different samples of the same rock type (Tables A11, A13, A15), and averages for rock types are plotted here for simplicity. (For interpretation of the references to colour in this figure legend, the reader is referred to the web version of this article.)

and for As (up to 56 PM) and Sb (up to 34 PM) in transitional lithologies and Chl-harzburgite (Fig. 5c). Lithium displays variably positive or negative anomalies as a function of textural growth stage. Negative anomalies are conspicuous for Zr, V, and Cr.

4.2.4. Ti-clinohumite

Data are few for pure Ti-clinohumite (Tables A8, A9), reflecting its rare occurrence in small crystals rich in inclusions in our rock samples. Ti-clinohumite in Atg-serpentinite has TiO_2 concentrations of 4.5 to 5.5 wt%, FeO ranges between 6 and 8 wt%, and SiO_2 between 37 and 38.5 wt%, and it shows subchondritic REE concentrations with a U-shaped pattern (not shown). Absolute trace element enrichments are observed for B (49–92 PM), W (15–121 PM), Nb (40–78 PM), Ta (22–32 PM), As (10–14 PM), Sb (up to 8 PM), and Li (up to 3 PM) (Fig. 5d).

4.2.5. Olivine

Mg# range between 88 and 93.5 (Table A10, similar to those reported in Padrón-Navarta et al., 2011). In a plot of Mg# versus Ni, different textural types of olivine form distinct clusters (Bretscher et al., 2018). The highest Mg# of up to 93.5 at low Ni are observed for clear olivine from Atg-serpentinites. In contrast, clear olivine cores (Ol-2) from spinifex-textured Chl-harzburgites and clear olivine from Chl-serpentinites have Mg# extending down to 88, at higher Ni. Clear olivine from granular Chl-harzburgite clusters around $89.5 < \text{Mg}\# < 91.0$ and shows the narrowest range (at variable Ni). Finally, brown olivine (Ol-3) and its clear olivine overgrowth (Ol-4) from spinifex-textured Chl-harzburgite range narrowly between 90.0 and 91.5 and overlap with the most Mg-rich clear olivine cores from this rock. REE patterns (Fig. 8e) are distinctly HREE enriched and variably low in LREE, Ol-4 from granular Chl-harzburgite showing the lowest LREE contents and the steepest REE patterns. Incompatible trace element enrichments are more prominent for olivine from Chl-harzburgites

(notably for the brown Ol-3) than from Atg-serpentinite and transitional rocks (Fig. 6a, b). Fluid-mobile element enrichments include B (up to 93 PM), As (up to 150 PM), Sb (up to 5 PM), Bi (up to 6 PM), W (up to 7 PM), and Li (up to 10 PM), while relative enrichments occur for Pb, Cs, Nb, Ta, and \pm U.

4.2.6. Orthopyroxene

Mg# cluster around 89.5 to 91 for orthopyroxene (Table A12) and thus vary considerably less than for olivine. Orthopyroxene REE-patterns mimic those of coexisting olivine. The patterns for transitional Atg-Opx-Ol-Chl rock and the spinifex-textured Chl-harzburgite are identical (Fig. 8f) at higher concentrations than that for orthopyroxene from granular Chl-harzburgite. Trace element distribution diagrams (Fig. 6c) reveal that orthopyroxene is absolutely enriched in B (12–23 PM), As (6–25 PM), Sb (3–74 PM), Bi (up to 5 PM), W (up to 40 PM), and \pm Th, \pm U, \pm Pb (for inclusion rich samples), along with a variably positive Li anomaly. Cadmium can be as high as 15 times PM for inclusion-rich measurements. Orthopyroxene in granular Chl-harzburgite shows the overall lowest trace element concentrations.

4.2.7. Clinopyroxene

Clinopyroxene Mg# are between 94 and 99, with a few measurements extending down to 91 (Table A14). Metamorphic clinopyroxene (Cpx-2 neoblasts) cluster at the high Mg# end. REE patterns (Fig. 8g) are variably convex except for relic mantle clinopyroxene that is slightly U-shaped with apparent LREE enrichment. To the contrast, metamorphic clinopyroxene not associated with relic Cpx-1 displays up to one order of magnitude lower LREE concentrations. A negative Eu anomaly is never developed. Relic Cpx-1 has highest incompatible trace element contents (Fig. 6d) and possesses the most prominent enrichments in B (up to 26 PM), As (up to 11 PM), Sb (up to 45 PM), Bi (up to 4 PM), W (up to 3 PM), and a positive Li anomaly (up to 9 PM). Compared to magmatic relics,

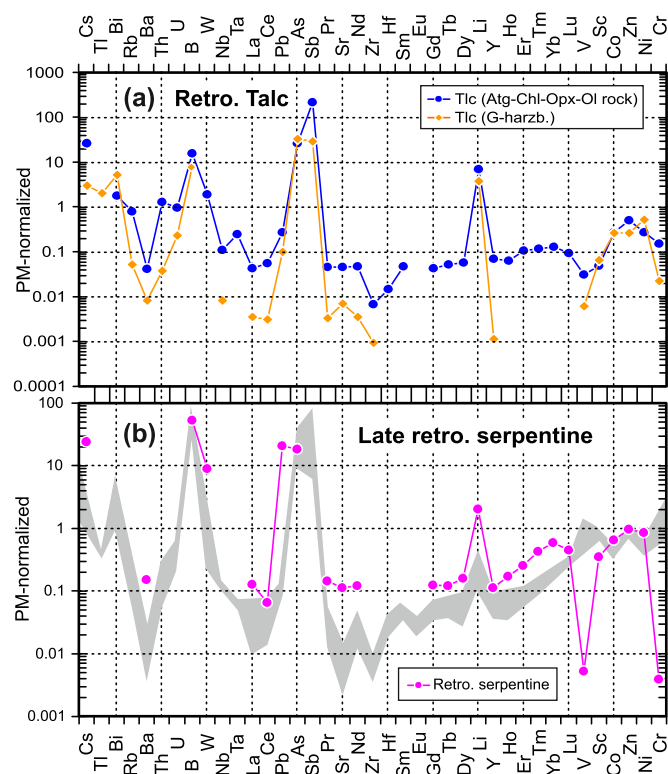


Fig. 7. Primitive mantle normalised trace element diagrams for retrograde hydrous minerals from Almirez metaperidotites. Mineral labels of the legends refer to mineral growth stages displayed in Fig. 2. The grey field in (b) shows the pattern for prograde antigorite (Fig. 5a) for comparison, illustrating prominent enrichment in Pb, Cs, and Sr in late retrograde serpentine. Primitive mantle (PM) values are from Palme and O'Neill (2014). Note that mineral trace element concentrations can vary significantly between different samples of the same rock type (Tables A17, A18), and averages for rock types are plotted here for simplicity. (For interpretation of the references to colour in this figure legend, the reader is referred to the web version of this article.)

metamorphic clinopyroxene has overall lower incompatible element concentrations at a largely similar pattern except for a negative Li anomaly. Cadmium can have up to 15 times PM concentrations.

4.2.8. Retrograde talc

Talc is characterised by $97.6 < \text{Mg}\# < 99.6$ and $60 < \text{SiO}_2 < 63$ wt%, irrespective of rock type (Table A16). The REE pattern is HREE enriched with flat MREE to LREE, with much higher concentrations in Atg-Opx-Ol-Chl rocks compared to Chl-harzburgites (Fig. 8d), mimicking REE concentrations in orthopyroxene that it retrogresses. Talc is strongly enriched (Fig. 7a) in As (up to 33 PM), Sb (up to 221 PM), B (up to 16 PM), Bi (up to 5 PM), Cs (up to 26 PM), and Li (up to 7 PM). Trace element patterns of retrograde talc and orthopyroxene from which it grew are comparable. However, concentrations in talc tend to be lower compared to those of orthopyroxene in REE, Nb, Th, U, Co, Zn, and Cr; while Cs, Ti, Rb, Ba, Pb, As, Sb, Sr, and Li are higher (comparison based on the granular Chl-harzburgite Alm06-077). Cadmium can be enriched up to 3 times PM.

4.2.9. Retrograde serpentine after olivine

The few clean serpentine measurements replacing olivine along grain boundaries and cracks have returned significant trace element concentrations mostly for transition metals and REE (Table A18). The REE pattern is HREE enriched with flat MREE to LREE (like that for talc; Fig. 8d) and shows a negative Ce anomaly, at higher overall REE concentrations than antigorite (Fig. 8a). Of the FME, B ($10\text{--}18 \mu\text{g g}^{-1}$), As ($0.5\text{--}2 \mu\text{g g}^{-1}$), Sr ($2\text{--}3 \mu\text{g g}^{-1}$), Cs ($0.3\text{--}0.6 \mu\text{g g}^{-1}$), Ba ($0.9\text{--}1.3 \mu\text{g g}^{-1}$),

and Pb ($0.7\text{--}6 \mu\text{g g}^{-1}$) were detected. Importantly, the FME Pb, Ba, Cs, and Sr are distinctly higher in concentration when compared to prograde antigorite (Fig. 5a).

4.3. Predominant silicate mineral hosts for trace elements

Trace element concentrations (Tables A3 to A18) combined with the respective mineral modes (Table 1) were used to calculate which fraction of a given trace element is hosted in which major rock forming silicate mineral as illustrated in Fig. 9. Note that the mass balance calculations are influenced by the fact that some trace element measurements in some silicates were below the respective LODs. In these cases, we adopted a zero concentration to calculate the bulk silicate trace element inventories (elements marked with * in Fig. 9). This figure reveals the predominant silicate mineral sinks for given trace elements in typical hydrous meta-peridotites equilibrated at ca. 50 km depth. For some elements (e.g., some transition metals) small modes of oxide and sulphide minerals can be relevant if not dominant for the bulk rock inventory; corresponding detailed oxide systematics are addressed in Vieira Duarte et al. (2021), and the impact of minor sulphides stable at peak-metamorphic conditions will be discussed elsewhere.

Fig. 9a,b,c reveals that antigorite is a major host for most trace elements unless metamorphic clinopyroxene is stable and takes up significant portions of the REE, Sr, and Pb. Metamorphic olivine, present in strongly variable modes in Atg-serpentinites (Table 1) depending on original brucite modes (Peters et al., 2020; Kempf et al., 2020), can be relevant for some incompatible elements, B, Li, and for some transition metals. Titanoclinohumite hosts much of the bulk silicate Ti, Nb, Ta, Zr (and Hf), despite its trace abundances (below 1%). Chlorite is not relevant in bulk Atg-serpentinite as a trace element host, due to its mostly low trace element contents (Fig. 5b) combined with low modes. Metamorphic tremolite may only be relevant for Sr and, to a lesser extent, the REE in pyroxene-free Atg-serpentinite. Fig. 9a illustrates the impact of ~3.6% relic Cpx-1 that subordinately contributes to many trace elements of the bulk silicate inventories. By far the most prominent bulk rock trace element host, notably for FME including Cs, Bi, Rb, U (but little Th), B, As, Sb, and Zn in addition to some transition metals is antigorite whose destabilisation can liberate these elements to be incorporated into reaction product minerals or to leave the system in the escaping fluid. In clinopyroxene-free Atg-serpentinite, antigorite is the primary host of almost all elements (Fig. 9c). Note that Pb is not enriched in Atg-1 (Fig. 5a); consequently, serpentinisation enriches mantle rocks in Pb only moderately at best (in line with Kodolányi et al., 2012; Pettke et al., 2018), as is also evident from bulk rock trace element distribution diagrams (Fig. 3b).

Fig. 9d,e illustrates the trace element distribution among the silicates in Chl-harzburgite produced from antigorite dehydration. Here, granular and spinifex-textured Chl-harzburgite samples need to be considered separately, because the latter contains brown, inclusion-rich olivine that could be included as a separate phase for the trace element distribution calculation. This brown Ol-3, to a first order, is equally relevant to orthopyroxene as a host for many trace elements (Fig. 9d). To the contrast, pure Ol-2 and Ol-4 are insignificant on a bulk silicate scale except for B and Li (and some transition metals) because of their low trace element concentrations (Fig. 6b). Chl-2/3 crystallised in response to antigorite breakdown can represent a relevant host for Cs and some transition metals, notably V, Cr, and Sc. As for Atg-serpentinites, minor Ti-Chu can be relevant for the silicate HFSE budgets, in both Chl-harzburgite textural types. For granular Chl-harzburgite, only pure Ol-2 and Ol-4 is present (i.e., brown, inclusion-rich Ol-3 is not observed), and this olivine is again similarly relevant for many trace elements as is orthopyroxene. Olivine furthermore contains some HREE and some of the transition metals. No measurements of inclusion-rich olivine were attempted for granular Chl-harzburgite because the conspicuously brown Ol-3 growth stage of spinifex-textured Chl-harzburgite cannot be recognised petrographically in granular Chl-harzburgite.

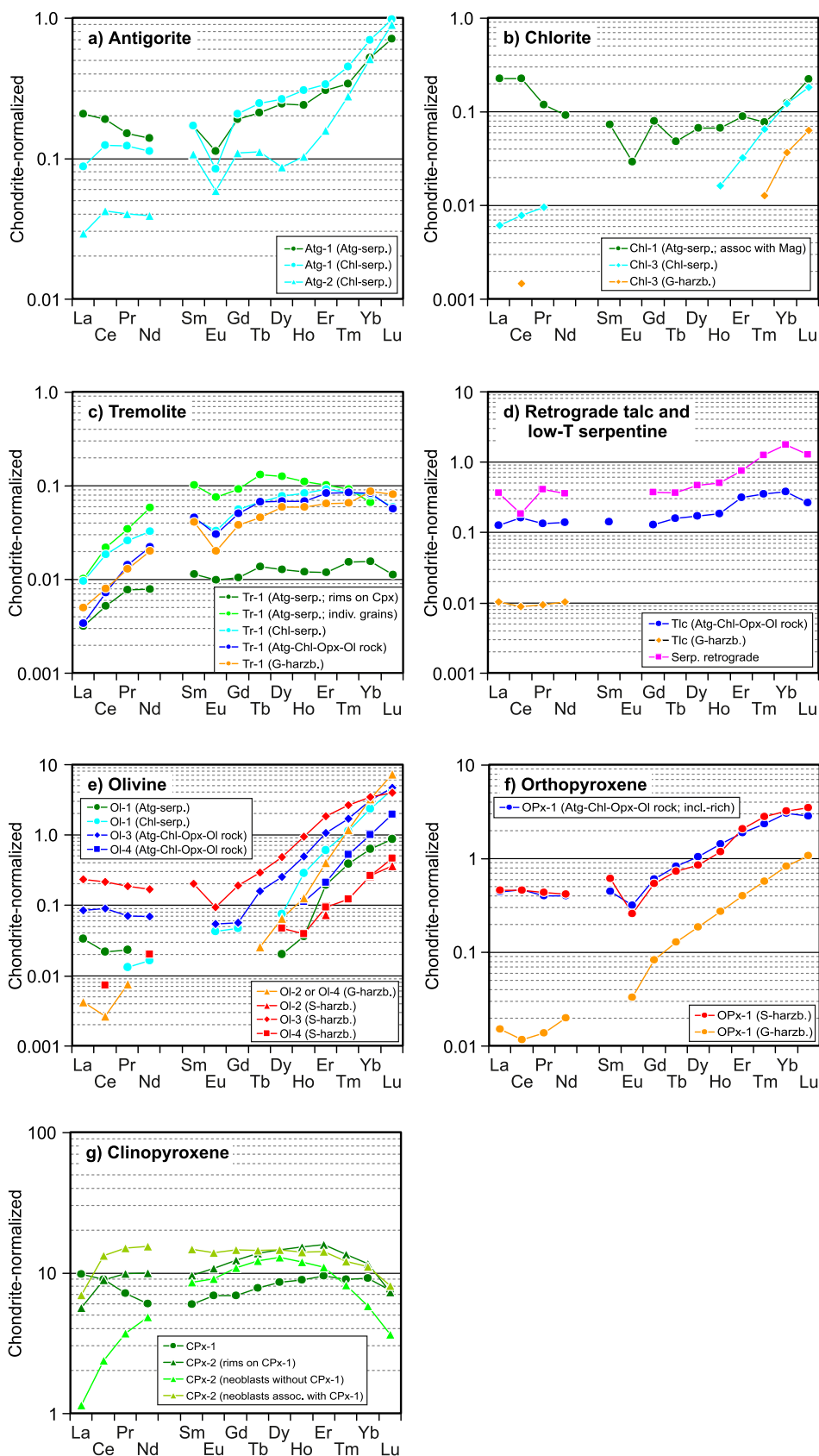


Fig. 8. CI Chondrite-normalised REE patterns of metaperidotite rock-forming minerals of Almirez. CI chondrite is from McDonough and Sun (1995). (For interpretation of the references to colour in this figure legend, the reader is referred to the web version of this article.)

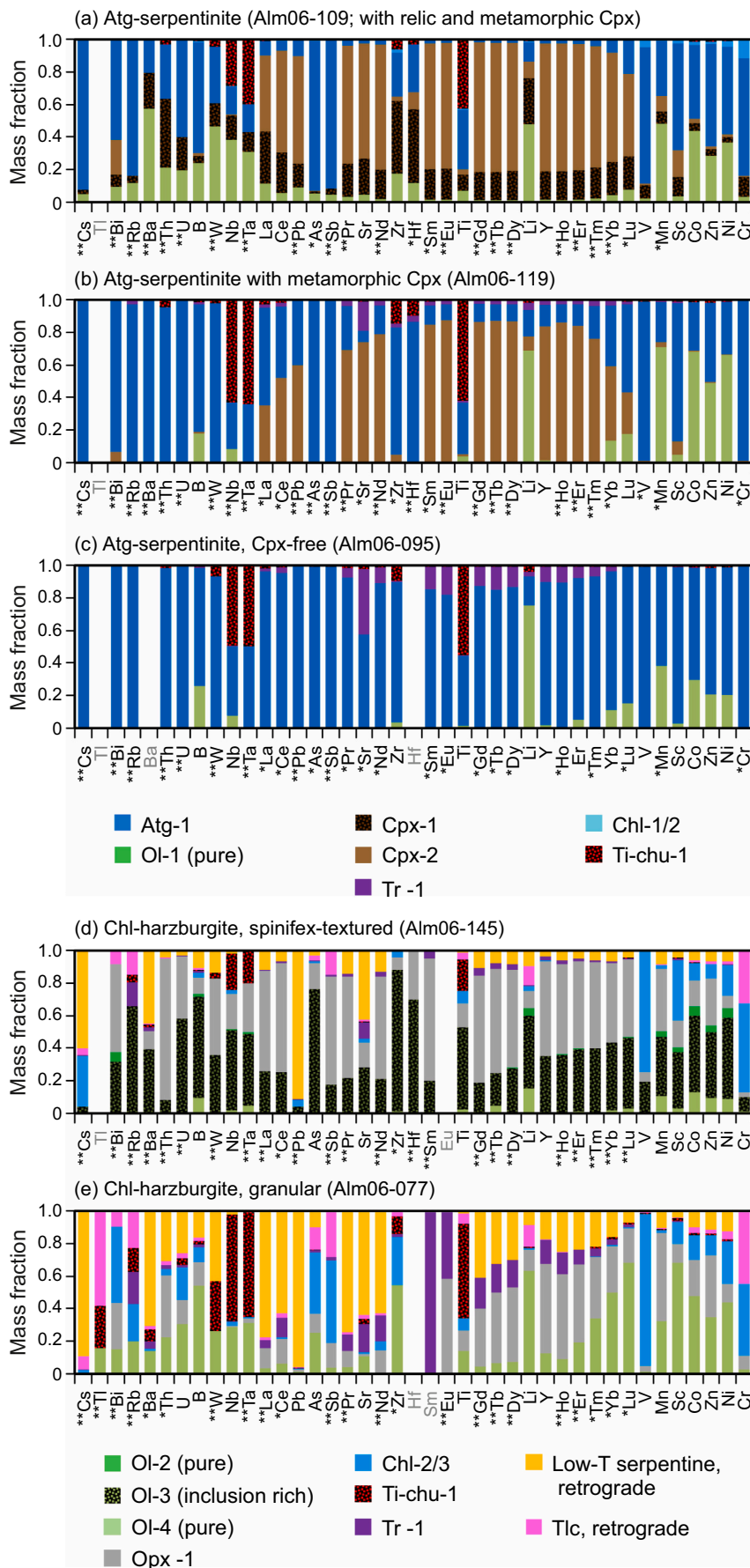


Fig. 9. Trace element silicate mineral mass balance diagrams. The mass fractions of trace elements for silicate minerals were calculated based on mineral modes (Table 1) and the corresponding measured trace element concentrations (Tables A3 to A18), for Atg-serpentinites (a-c) and Chl-harzburgites (spinifex-textured: d; granular: e). Note that for some elements in some minerals, element concentrations were below the respective LODs and these minerals thus enter the mass balance calculations with zero contribution. These elements are marked with one star (reflecting one silicate mineral below LOD) or two stars (reflecting two or more silicate minerals below LOD) on the X-axis. Elements with no significant silicate mineral measurement are set in grey on the X-axis. Measurements were made on petrographically pure minerals, and each measurement signal was screened for inclusions during data reduction in order to avoid such sections. Mineral data rich in inclusions are marked with a black dotted pattern fill (Cpx-1 in Atg-serpentinites, brown Ol-3 in spinifex-textured Chl-harzburgites, and Ti-chu-1 in all lithologies). These plots highlight the main prograde and retrograde silicate mineral sinks in bulk rock for a given trace element, and mineral stabilities control element (re)distribution during the subduction-exhumation cycle. (For interpretation of the references to colour in this figure legend, the reader is referred to the web version of this article.)

Orthopyroxene is relevant for MREE(-HREE) and Th but less so for U.

Retrograde silicates, notably serpentine, host significant fractions of many trace elements, including many FME. In fact, for granular Chl-harzburgite, retrograde serpentine (at modes of ~10%; Table 1) dominates the silicate trace element budgets for Cs, Ba, Pb, Sr, and the LREE, while only Cs, Pb, Ba, and Sr are relevant for spinifex-textured Chl-harzburgite. Retrograde talc is less important for the silicate trace element bulk rock budget, due to its usually low modes (Table 1), and because its trace element inventory mimics that of orthopyroxene which it retrogresses (compare Fig. 7a with Fig. 6c).

5. Discussion

Major to trace element systematics reveal the combined effects of (i) magmatic mantle history involving melt depletion and refertilisation, (ii) hydration along with metasomatism on the ocean floor and possibly in trench to forearc settings at the onset of subduction, (iii) partial element loss upon metamorphic dehydration during subduction notably at peak antigorite dehydration, and (iv) selective element gain upon retrograde hydration during exhumation. This discussion now evaluates these diverse contributions, in order to better define the geochemical systematics in this multistage process and to clarify tracer systematics for specific aspects of the overall evolution. As a result, we then present our preferred lithosphere scale model for the genesis and evolution of slab serpentinites with progressive subduction to beyond antigorite dehydration.

5.1. Geochemical consequences of retrogression during exhumation

Serpentinisation enriches mantle rocks in FME, and this can occur on the ocean floor, during early to peak subduction stages, and also “retrograde” during exhumation. Up to now, the latter contribution has commonly been neglected (for exceptions see e.g., Schwarzenbach et al., 2018a; Locatelli et al., 2019; Gilio et al., 2020; Vieira Duarte et al., 2021). However, at fluid-saturated conditions along high-permeability zones such as the subduction plate interface or shear zones between rock units that are active during exhumation, retrogression can be expected to be omnipresent, potentially erasing much of the prograde to peak metamorphic rock record (e.g., Gilio et al., 2020). Here, we document that even rocks without direct link to large-scale exhumation structures can also record significant retrogression.

At Almiraz, retrogression of partially dehydrated mantle rocks on exhumation is variably prominent, with potential for misinterpretation of geochemical data obtained for bulk rock samples. Partial retrograde hydration for our Chl-harzburgite samples is demonstrated by LOI values of between 4.1 and 4.9 wt% (and up to 8.6 wt% for bulk rock Chl-harzburgite data in Marchesi et al., 2013, also assuming absence of peak carbonate in their samples) that are higher than the ≤ 3.4 wt% bulk rock H₂O stored in peak chlorite for which maximum modes can be calculated based on measured bulk rock Al₂O₃ concentrations. Assuming for our bulk rock data (Table A1) that the unaccounted-for LOI after chlorite removal is water stored in retrograde serpentine and talc (assuming absence of carbonate and tremolite, whose modes are generally below 1%), this amounts to $\leq 10\%$ serpentine and variable talc modes (Table 1). These retrograde serpentine concentrations correspond to, or are slightly higher than, those determined by point counting. Atg-serpentinites show less petrographic signs of retrogression, but we caution that this cannot be quantified by the LOI mass balance approach.

Fig. 9e illustrates that retrograde serpentine may dominate the silicate mineral bulk rock trace element inventory notably for the incompatible FME in granular Chl-harzburgite, while for spinifex-textured Chl-harzburgite the impact of retrograde serpentine seems to be less important (Fig. 9d). We note that Pb and Cs concentrations in retrograde serpentine are the highest mineral concentrations measured along with elevated As for both textural Chl-harzburgite types (also distinctly higher than prograde antigorite; Fig. 5a). The observation that granular

Chl-harzburgite possesses much more relevant trace element fractions hosted in retrograde serpentine is interpreted here to partially result from the fact that prograde silicate minerals in granular Chl-harzburgite are well equilibrated and contain less (submicroscopic) inclusions. Opx-1 in granular Chl-harzburgite has distinctly lower overall trace element contents when compared to Opx-1 from spinifex-textured Chl-harzburgite (Fig. 6c), and the brown inclusion-rich Ol-3 occurs in spinifex-textured Chl-harzburgite only. As a consequence (and given similar modes of retrograde serpentine in both rock types), the impact of retrogression on the silicate trace element systematics is more relevant for granular Chl-harzburgite.

Our data also reveal significant enrichments in some FME for retrograde talc, while the other trace elements largely conserve the trace element pattern of orthopyroxene from which talc formed. These notably include Cs, As, and Sb, whose concentrations in talc are up to an order of magnitude higher than for orthopyroxene which it retrogresses (compare Fig. 7a with Fig. 6c).

Plotting LOI values in excess of that caused by chlorite presence (modes calculated assuming all Al₂O₃ is fixed in chlorite) versus bulk Chl-harzburgite Cs and Pb concentrations (Fig. A2) allows for testing whether retrogression dominates these element inventories in bulk rocks. The green field reveals variable excess in Pb (less so in Cs) bulk rock concentrations, indicative of at least one relevant source component introduced by the retrogressing fluid. Almiraz bulk rock data are offset from MOR and forearc trends in some FME correlation diagrams involving Cs (Peters et al., 2017); hence, this offset may therefore result in part from retrogression and partially mask their original ocean floor trace element imprint (recall that ocean floor hydration for Almiraz rocks is demonstrated by prominent rodingite occurrences; e.g., Trommsdorff et al., 1998; López Sánchez-Vizcaíno et al., 2005).

Our combined observations caution that a significant fraction of the bulk Pb, Cs, As, B, $\pm W$, $\pm Sb$ can be introduced along with the infiltrating fluid upon retrogression, even for rocks without direct link to large-scale exhumation structures such as shear zones, thus potentially producing scatter in data. As a consequence, claims for prominent sedimentary fluid involvement during initial serpentinisation or early subduction based on simple bulk rock enrichments of specific FME such as Cs, As, Pb may be grossly misleading. Even more seriously, source tracing based on bulk rock Pb isotope ratio systematics of orogenic peridotites can lead to erroneous implications when much of the Pb is introduced upon retrogression (also cautioned by Cannao et al., 2015). Along the same lines, Vieira Duarte et al. (2021) report prominent oxide mineral addition upon retrogression, which may lead to erroneous interpretations on peak-metamorphic f_{O_2} conditions. Clearly, geochemical signals relevant for ultimate source tracing also need to be well developed in exclusively prograde to peak major rock forming minerals (e.g., metamorphic Ol, Opx, or texturally early antigorite in Atg-serpentinites; see discussion below), thus, requiring in-situ measurement data.

5.2. Magmatic mantle history

The chemical signatures of abyssal peridotites prior to serpentinisation are the combined product of diverse melt depletion histories and variable refertilization upon melt rock interaction (e.g., Navon and Stolper, 1987; Niu, 2004; Bodinier and Godard, 2014; Müntener et al., 2004, 2010; Paulick et al., 2006; Deschamps et al., 2013). We now demonstrate that magmatic refertilization plays a dominant role for at least some of the Almiraz orogenic hydrous peridotites regarding their incompatible element chemistry, and we define these chemical imprints, in order to better constrain below the element additions upon serpentinisation and partial element loss during subduction.

Atg-serpentinites to Chl-harzburgites at Almiraz display variable MgO/SiO₂ for their given Al₂O₃/SiO₂ (Fig. A1), i.e., plot generally on or below the mantle melting residue trend (Jagoutz et al., 1979; compare Bretscher et al., 2018; Marchesi et al., 2013). Rocks plotting on the melting residue trend likely underwent near-isochemical

serpentinisation (except for H₂O addition) as documented for other orogenic serpentinites (e.g., Erro Tobbio, Peters et al., 2020), while those plotting variably below the melting residue trend rather fit on the oceanic array (Niu, 2004). The latter is typical for abyssal serpentinized peridotites (Niu, 2004; Kodolányi et al., 2012) sampled near the ocean floor, interpreted for example to represent addition of SiO₂ upon ocean floor hydration, which is our preferred interpretation (compare Paulick et al., 2006; Malvoisin, 2015; Schwarzenbach et al., 2021). Alternatively, this might reflect MgO loss during low temperature seafloor weathering (e.g., Snow and Dick, 1995; Klein et al., 2017); however, there is no correlation observed for our data between bulk rock Mg# and the extent of deviation from the mantle melting residue trend in support of Mg loss from the rocks upon serpentinisation (Fig. A1). Moreover, intense serpentinite weathering on the ocean floor goes along with progressive oxidation, including conversion of magnetite to hematite and Fe-hydroxide formation (e.g., Klein et al., 2017). Because our samples display a first order correlation between Mg# of (Mg,Fe)-silicates with magnetite modes (Bretscher et al., 2018; Vieira Duarte et al., 2021), the degree of bulk sample oxidation is interpreted here to represent a high-temperature seafloor hydration feature (compare Klein et al., 2014) and not the product of intense serpentinite weathering.

Bulk rock Mg# (87.7 < Mg# < 90.9) of our samples thus reflect primary magmatic signatures and reveal that the rocks are variably refractory (Bretscher et al., 2018). Alumina concentrations tend to be low, resulting in Al₂O₃/SiO₂ ratios that are typical for abyssal peridotites (0.03 > Al₂O₃/SiO₂ > 0.07; Niu, 2004) but higher than most mantle wedge serpentinites (Al₂O₃/SiO₂ < 0.03; Deschamps et al., 2013). Despite significant amounts of talc present in partial to complete antigorite breakdown product Chl-harzburgite, their SiO₂ concentrations do not display strong, systematic enrichment relative to the peridotite melting residue trend (Fig. A1). This is consistent with petrographic and geochemical evidence that talc directly retrogressed peak orthopyroxene and is thus not indicative of significant SiO₂ addition to bulk rock. In a plot of CaO vs. Al₂O₃, most samples reveal CaO depletion for their Al₂O₃ (Bretscher et al., 2018, their Fig. 5c; the same applies to data of Marchesi et al., 2013), resulting from CaO loss during ocean floor alteration (e.g., Coleman and Keith, 1971). However, many Atg-serpentinites of this work reveal excess in CaO for their Al₂O₃ (also documented for some Atg-serpentinites of Marchesi et al., 2013, and other high-P Atg-serpentinites such as Erro Tobbio; Peters et al., 2020). This reflects CaO addition upon prominent melt/rock interaction (Godard et al., 2000) that is conspicuous from REE patterns (discussed below). Indeed, none of the Atg-serpentinites investigated here contains prominent carbonate (despite the local occurrence of meta-ophicarbonates associated with Chl-harzburgites; Menzel et al., 2019), and the elevated CaO concentrations correlate with clinopyroxene abundances (Table 1). As expected for melt depletion/refertilization trends (and not illustrated here), MgO versus Cr, Ni, Co, show positive trends, while the trend of MgO versus V is negative, reflecting their compatibilities. Similarly, Yb correlates positively with Al₂O₃ and negatively with MgO.

Combined trace element evidence corroborates that variably prominent post-melting magmatic refertilization affected the Almirez meta-peridotites (compare Bodinier and Godard, 2014). This includes two distinct groups of patterns in bulk rock chondrite-normalised REE patterns (Fig. 3a), given that REE are not mobile upon serpentinisation (e.g., Allen and Seyfried, 2005) and given that there is no supporting evidence for significant serpentinite weathering. Overall, the LREE vary much more than do the HREE, and the REE patterns cannot be accounted for by simple melt extraction. Group (I) is characterised by LREE_N > HREE_N with a nearly flat, superchondritic pattern and encompasses Atg-serpentinites with relic clinopyroxene (with elevated CaO relative to their Al₂O₃), and one Chl-serpentinite. Such a signature likely identifies interstitial entrapment of melt that earlier lost its HREE inventory to peridotite minerals via reactive melt percolation, leaving behind a LREE and highly incompatible element enriched melt fraction different from

mid ocean ridge basalt (MORB) composition (Niu et al., 1997). Group (II) displays MREE_N < HREE_N along with MREE_N < LREE_N, i.e., a U-shaped pattern, skewed to LREE_N < HREE_N and with variably pronounced negative Eu anomalies (also reported by Marchesi et al., 2013). These rocks likely record cryptic refertilization in the thermal boundary layer by melts residual after plagioclase fractionation (indicated by the negative Eu anomaly), likely via porous flow (e.g., Niu et al., 1997; Niu, 2004). This duality in refertilization processes is conspicuously expressed in a diagram of La/Sm vs. Th/La (Fig. A3), where Atg-serpentinites and Chl-serpentinites display a trend of uniform Th/La with variable La/Sm and the rocks having undergone antigorite dehydration display a steep positive correlation. This observation suggests that preconditioning upon magmatic refertilization may have exerted partial control on the extent of ocean floor peridotite hydration and associated oxidation, which in turn dictated whether antigorite dehydrated or not in the Almirez ultramafic rock suite. Our result corroborates the interpretation by Bretscher et al. (2018) that the antigorite dehydration reaction front at Almirez corresponds to a prominent compositional boundary, a seafloor oxidation front established during serpentinisation that seems to have been preset at least in part by the type and extent of magmatic refertilization.

Positive trends between LREE and incompatible, fluid-immobile HFSE strengthen the above interpretations. For example, the diagram of Th vs. Ce (Fig. 4a) reveals two different slopes for groups (I) and (II), interpreted to again document the two different regimes at which melt-rock interaction occurred. Group (I) meta-peridotites show prominent LREE enrichments along with modest HFSE enrichments while Group (II) meta-peridotites show variable HFSE (that correlate well among each other) at uniform LREE. Melt-rock interaction trends are displayed in plots of Th vs. Nb (Fig. 4b) or Th vs. Ta and show weak trends in Th vs. Gd/Lu and Th vs. La diagrams (compare Paulick et al., 2006; Niu, 2004; not shown). The few outliers towards high Nb, Ta for a given Th can be accounted for by a nugget effect caused by scattered presence of Ti-clinohumite, since Ti-clinohumite has very high Nb and Ta along with low Th (Table A9). Altogether, our bulk rock data record variably prominent refertilization upon melt/rock reaction that occurred at least in part in the thermal boundary layer (e.g., Niu, 2004) from plagioclase-fractionated melts (Group (II)), superposed on a history of variable melt extraction. In fact, not only bulk rock geochemistry but also mineral trace element patterns (residual mantle Cpx, ocean floor Chl-1, and Atg-1; Fig. 8a,c,g) document geochemical characteristics of magmatic refertilization including variably prominent LREE enrichment.

Irrespective of which magmatic process dominated the final geochemical signatures of a given Almirez meta-peridotite sample (except for the FME; see below), the prominent variations recorded by the rocks document that materials of prominent geochemical diversity - on mm to likely km scales - were eventually hydrated and subducted. This is also characteristic for orogenic serpentinites from the European Alps (e.g., Müntener et al., 2004, 2010) and probably valid in general. Models invoking fluid-rock interaction with rodingites upon prograde subduction to account for the relative excesses of incompatible HFSE when compositions of Chl-harzburgites are directly compared to those of Atg-serpentinites (Garrido et al., 2005; Marchesi et al., 2013) are thus not required to account for the LREE-MREE-HFSE systematics as clarified here. These features can be explained entirely by the strongly variable pre-serpentinisation magmatic evolution. As demonstrated by our data, these fluid-immobile element characteristics largely survived subsequent serpentinisation on the ocean floor and partial dehydration during subduction to ~50 km depth. Fluid-immobile element systematics therefore represent the required baseline (illustrated in Fig. 3b as the grey band) in relation to which the fluid-mediated chemical modifications imposed upon ocean floor hydration and prograde metamorphism need to be evaluated.

5.3. Geochemical imprints upon peridotite hydration

5.3.1. Bulk rock scale

Ocean floor serpentinisation including at trench to shallow forearc settings produces characteristic element enrichments, either absolute ones to values exceeding PM concentrations or relative ones to elements of similar compatibility during mantle melting. Elements that can be absolutely enriched include B, As, Sb, U, W, Cl, Br, I, Sr, Li, and LILE, while relative enrichments are sometimes observed for Pb (compare Kodolányi et al., 2012; Vils et al., 2008; Savov et al., 2005, 2007; Paulick et al., 2006; Kendrick et al., 2013; Jöns et al., 2010; Deschamps et al., 2011; Boschi et al., 2013; Debret et al., 2013; Andreani et al., 2014; Barnes et al., 2014; Kahl et al., 2015; Peters et al., 2017; Albers et al., 2020; Hattori and Guillot, 2003; Bonatti et al., 1984; Thompson and Melson, 1970). However, data for a series of elements have remained scarce to date for ocean floor serpentinites including W, In, Bi, Sn, Cd, and Tl, of which notably the chalcophile elements Tl and Sn were documented to be strongly enriched in altered MORB (Jochum and Verma, 1996).

Comparison of measured hydrous metaperidotite trace element patterns with expected magmatic depletion trends in PM-normalised trace element distribution diagrams only offer a first order means to estimate fluid-mediated element enrichments for samples showing significant magmatic refertilization. This is because measured bulk rock samples are related to a geochemical reservoir of given composition (i. e., PM), which is demonstrably inappropriate for the Almiraz samples as revealed by the fact that bulk rock Th concentrations vary by over an order of magnitude for the entire sample set. Fig. 3b therefore attempts to mitigate this problem by displaying a sample set specific grey field illustrating the compositional characteristics and variations expected from combined melt depletion and refertilization. This field is significantly different from the expected melt depletion trend (also displayed in Fig. 3b) because it flattens out towards the incompatible elements. The widths of this grey band attempts to depict the prominent pre-hydration trace element variations as revealed on the basis of fluid-immobile, incompatible elements (e.g., Th or La) that may well exceed one order of magnitude. This still crude approach identifies a few elements with anomalies above the grey field for our data set, notably for B, W, As, Sb, and \pm Cs, \pm U, \pm Bi, \pm Pb, \pm In, and \pm Li. These elements thus unequivocally contain hydration-induced enrichments, most likely upon ocean floor serpentinisation (recall the numerous rodingites in the ultramafic rock bodies at Almiraz).

This general approach needs refinement, however, because it relates measured element concentrations of a given sample to the overall pre-hydration element concentration variations of the entire sample set, covering more than an order of magnitude variability (Fig. 3b). Such a refinement from the inter-sample perspective to an intra-sample approach can be achieved by ratioing FME concentrations over those of fluid-immobile elements with similar magmatic incompatibility, identifying fluid-mediated relative enrichments for specific elements individually for each sample. We quantify this here as dimensionless hydration enrichment numbers (HEN).

U/Th systematics serve as a prime example for illustration of the principle (Fig. 4c). Measured bulk rock data for Almiraz are related to the well-known range for mantle peridotite U/Th ratios (mantle array; green fan for U/Th between 0.25 and 0.44; Elliott et al., 1999). Of our samples, Group (I) ultramafic rocks largely plot inside this array, thus documenting that their Th—U budget can be accounted for entirely by magmatic processes as was demonstrated before for the prominent LREE enrichments. To the contrast, Group (II) samples display variable ocean floor hydration-related enrichment in U relative to their Th concentrations, most prominently so for the spinifex-textured Chl-harzburgites (U/Th up to 1.8). However, observed extents of U enrichment are modest when compared to serpentinites mostly originating from near the ocean floor (dredged or shallow drill cores; compare Niu, 2004; Kodolányi et al., 2012; Deschamps et al., 2011; Agraniér et al., 2007),

and this excess U is hosted predominantly in antigorite or in orthopyroxene of Chl harzburgite (Tables A3, A13). We interpret this modest U enrichment to be characteristic of near rock-buffered hydration conditions, likely at moderate water/rock ratios, whereby the hydrating fluid may have lost most of its U cargo via reduction prior to reaching the site of Almiraz peridotite hydration. This example illustrates the need to constrain trace element systematics on a per-sample basis in order to quantify fluid-mediated element enrichment systematics; element concentrations alone (even when normalised to PM for example) may not reveal these or may possibly lead to erroneous interpretations.

To arrive at a general quantification of the principle just illustrated, we define the calculation of hydration enrichment numbers for bulk rock data as follows:

$$\text{HEN} = (\text{FME}/\text{FIE})_{\text{meas}} / (\text{FME}/\text{FIE})_{\text{PM}} \quad (9)$$

where HEN stands for hydration enrichment number, FME stands for fluid mobile element, and FIE stands for fluid immobile element, both of closely comparable magmatic compatibility. Importantly, element pairs of very similar magmatic compatibility but very different fluid mobility need to be employed for this calculation. The magmatic compatibility sequence displayed on the X-axis of trace element variation diagrams (e. g., Fig. 3b) can thereby be approximated via dividing reservoir element concentration estimates for depleted mantle by those for primitive mantle (data from GERM data base, 2021); the lowest values correspond to elements with highest magmatic incompatibility and plot to the left of the X-axis. Experimental data from the literature then indicate whether a given element tends to be mobile or immobile in aqueous fluid at temperatures below ~ 425 °C (the maximum temperature invoked for peridotite serpentinisation on the ocean floor; e.g., Früh-Green et al., 2004). The measured ratio of fluid-mobile element over a fluid-immobile element of closely comparable magmatic compatibility, i.e., ideally neighbours on the X-axis of trace element distribution diagrams, is then normalised to its corresponding primitive mantle abundance ratio. This results for our example of U (fluid mobile at oxidising conditions) and Th (fluid immobile) in:

$$(\text{U}/\text{Th})_{\text{meas}} / (\text{U}/\text{Th})_{\text{PM}} \quad (10)$$

Numbers > 1 identify overall FME enrichments and numbers < 1 identify FME depletions (Table 2), illustrated in Fig. 10 for Almiraz bulk rock data. This concept assumes that the magmatic processes of melt depletion and refertilization prior to hydration produce mantle peridotite element abundance ratios largely dictated by element compatibility. This assumption is incorrect for Zr and Hf in our data set, however, because depletions in Zr and Hf relative to elements of similar compatibility (Fig. 3b) result from magmatic processes prior to serpentinisation that are not captured by simple melt extraction processes (compare discussions in Niu, 2004; Bodinier and Godard, 2014). Moreover, our sample set documents two different modes of magmatic refertilization (discussed above). Despite these limitations, the approach of determining the hydration enrichment number reliably and prominently reduces ambiguity in interpreting trace element variations plotted in conventional PM-normalised data representation (compare Fig. 3b). Before we elaborate on the systematics of selected FME, we now address which silicate minerals are the relevant hosts for a given FME, offering constraints on when FME enrichments occurred and when FME may be liberated from serpentinites with progressive subduction.

5.3.2. Silicate mineral trace element sinks

Central to the fate of FME with progressive subduction is which fraction of the total bulk rock content for a given element is hosted in which mineral. Mineral stabilities with progressive subduction then dictate how long a given trace element remains fixed in the rock, and metamorphic dehydration reactions represent variably discrete events during which part of the trace element rock inventory may be mobilised and escape the rock. Our evaluation for the silicates is now based on PM-

normalised trace element diagrams for hydrous silicates (Fig. 5), anhydrous silicates (Fig. 6), and retrograde talc and serpentine (Fig. 7). We note here that hydration enrichment numbers as employed for bulk rock data cannot be used for mineral data because we lack mineral/bulk rock element distribution coefficients for the relevant conditions of hydration / dehydration, and these are likely to be prominently variable for the different FME and FIE in the diverse minerals. Together with the diagrams illustrating element distributions among the major rock-forming silicates in Atg-serpentinites and Chl-harzburgites (Fig. 9), the following general implications can be drawn.

In Atg-serpentinites, clinopyroxene, when present, hosts most of the REE, along with Y, Sr, and Pb (Fig. 9a,b). This demonstrates that even for peridotites near-fully hydrated on the ocean floor relic Cpx-1 trace element systematics record the complex magmatic processes prior to hydration (Fig. 8g, and discussion above). Because relic clinopyroxene often contains now hydrated exsolution lamellae of former orthopyroxene, bulk relic pyroxene measurements also display variably prominent FME enrichments (including B, As, Sb, U, or Cs; Figs. 6d, 9). Fig. 9c reveals that once relic pyroxene is lost, Atg-1 is the major host for most of the trace element inventory in Atg-serpentinite (regardless of its degree of magmatic depletion), notably including most FMEs. Only the REE, Sr, and Pb may reside in metamorphic Cpx-2 if it crystallises (Fig. 9b). Antigorite thus represents the key FME carrier mineral to the deep subduction environment, redistributing this inventory to product minerals plus dehydration fluid notably upon antigorite breakdown somewhere between ~40 and ~150 km depth. Metamorphic Ol-1 in Atg-serpentinite can be relevant only for Li, B, some of the transition metals, and a subordinate fraction of the fluid-immobile HREE (Figs. 6a, 9a–c), and metamorphic Tr-1 and Chl-1/Chl-2 are generally irrelevant for the bulk rock trace element budget because of their low modes. Hydration-specific trace element signals stored in antigorite include prominent enrichments in B, As, Sb, Bi, Cs, W, and U (Fig. 5a). Importantly, U/Th ratios are strongly elevated in some antigorite measurements, thus documenting that it is the serpentine mineral that carries excess U down subduction zones. Given these prominent FME enrichments in antigorite, they had to be formed prior to or at prograde antigorite crystallisation.

Because our bulk rock data compare well to those reported for serpentinised peridotites dredged on the ocean floor (Niu, 2004) in Al₂O₃/SiO₂ vs. MgO/SiO₂ representation (Fig. A1), our major element data do not reveal a prominent SiO₂ enrichment as can be expected in a scenario where significant fluid-mediated trace element influx at elevated metamorphic conditions is postulated to enrich antigorite in As, Sb, and Cs derived from sedimentary fluids (e.g., Scambelluri et al., 2019, and reference therein). We therefore conclude that the prominent FME enrichments in hydrous peridotites of Almiraz, along with modest SiO₂ metasomatism, originate predominantly from ocean floor hydration.

In Chl-harzburgites, inclusion-bearing brown Ol-3 concentrates almost all elements relative to coeval Opx-1 and Chl-3 and shows overall higher trace element concentrations than Ol-2 and Ol-4 from the same rock (Fig. 6b). This reveals two aspects, (i) how relevant tiny inclusions in minerals are for Chl-harzburgite bulk rock trace element inventories, and (ii) that FME are prominently redistributed upon antigorite dehydration. Inclusion-free Opx-1 can host significant fractions of REE, Th, Bi, W, U, and some transition metals, but not alkali nor most FME (Fig. 6c), while inclusion-free olivine can be relevant for B, Li, Bi, W, ±As, and MREE-HREE (Fig. 6b). Chlorite is the last hydrous mineral stable beyond antigorite dehydration (besides humite group minerals), and the FME enrichment pattern of Chl-3 formed upon antigorite dehydration (Fig. 5b) is again closely comparable to that of reactant antigorite, albeit at overall lower concentrations. Chlorite is thus not relevant for the bulk rock FME budget of Chl-harzburgite, except possibly for Bi and Cs (Fig. 9d,e), as is the case for chlorite in Atg-serpentinite.

Our first order conclusions are that FME enrichments occurred upon early hydration in the rock's evolution and that the most prominent

Table 2
Hydration enrichment numbers.

	Cs/Th	Tl/Th	Bi/Th	Rb/Th	Ba/Th	U/Th	B/Th	W/Th	W/Nb	In/Ce	In/Th	Pb/Ce	Pb/Pr	As/Pr	Sb/Pr	Sr/Nd	Sn/Sm	Li/Y	Zn/Ni
Alm06-094	4.1			0.1	1.5	1.4	26	3.0	7.1	1.2	1.3	0.8	1.0	27	37	0.2	0.9	0.8	0.5
Alm06-107	1.3		4.3	0.1	0.2	1.1	28	1.6	1.9	0.7	0.7	1.4	1.4	13	8	0.2		1.3	0.5
Alm06-109	4.0		1.9	0.1	0.1	1.4	26	5.9	16.8	0.9	1.0	0.9	1.1	25	37	0.2	1.1	0.8	0.4
Alm06-119	10.1		32.5	0.3	0.3	3.0	169	101.7	60.6	2.4	3.0	7.8	8.5	147	515	0.3		2.3	0.5
Alm06-095	8.7		13.8	0.3	5.1	3.4	201	10.1	9.1	1.7	1.8	3.8	4.5	302	208	0.2		0.9	0.3
Alm06-085	4.4			0.2	0.6	1.2	75	96		0.7	1.2	0.5	0.6	11	32	0.3	0.6	1.5	0.6
Alm06-111	35.8			1.2	0.8	4.0	31	22.3	9.8	2.2	1.4	4.7	6.3	28	64	1.0		20.8	0.5
Alm06-113	46.3			0.8	0.6	3.2	58	11.4	4.3	2.2	2.1	3.6	4.8	34	49	0.9		12.3	0.4
Alm06-086	3.4			0.2	0.4	2.0	55	35.6	18.6	5.3	0.9	7.3	7.8	197	563	1.5	5.0	12.8	1.2
Alm06-087	11.7	1.6	2.3	0.4	0.5	1.8	57	23.5	23.4	10.0	1.5	13.5	16.5	272	407	4.6		20.5	0.7
Alm06-058	2.1			0.1	0.3	1.9	29	6.4	6.7	14.1	1.4	16.1	17.7	266	278	2.2		8.3	0.5
Alm06-077	3.9	0.5	0.9	0.1	0.2	1.6	22	2.9	4.6	9.7	0.9	12.1	13.6	458	100	1.5	11.4	29.5	0.5
Alm06-141	15.4			0.3	3.0	5.5	32	73	35.2	6.2	1.6	6.2	7.2	464	212	1.0		6.5	0.8
Alm06-142	9.0		2.7	0.3	0.4	6.5	65	18.4	23.1	11.2	1.6	24.7	31.3	648	129	1.6		4.5	0.6
Alm06-145	6.2	2.1	1.8	0.1	0.3	4.1	53	85										6.2	0.5

Note: Hydration enrichment numbers were calculated as: (X/Y)_{meas}/(X/Y)_{PM}, whereby X is a fluid mobile element and Y is a fluid immobile element of similar compatibility during mantle melting.

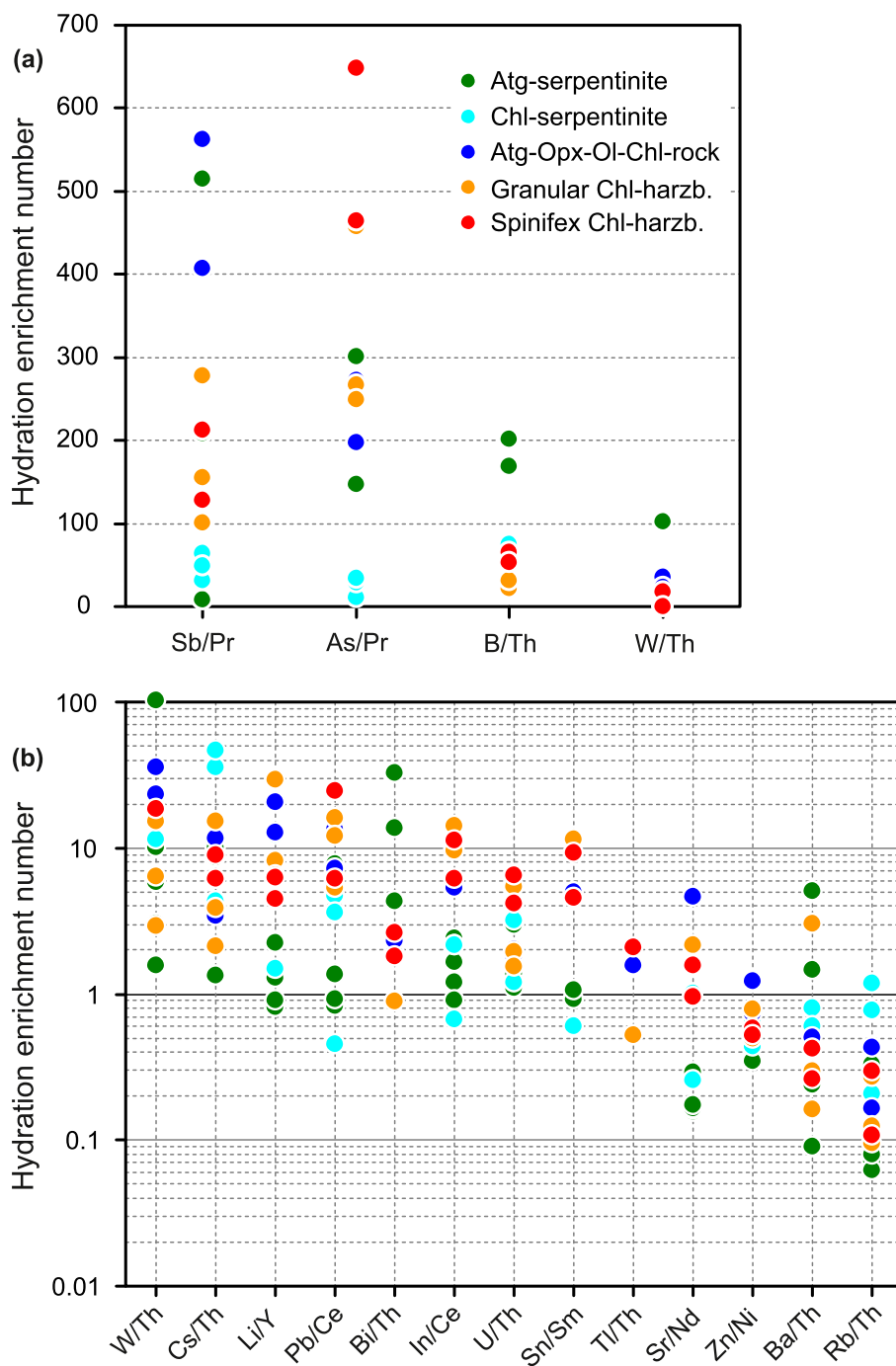


Fig. 10. Trace element hydration enrichment numbers for fluid mobile elements (as labelled in the numerator of the X-axis labels; denominators represent corresponding fluid immobile elements of very similar magmatic compatibility) of Almirez bulk rocks (Table 2). Most prominent FME enrichments are evident for As, Sb, B, and W (figure a), while prominent FME depletions are evident for Rb, Ba, Zn, and \pm Sr (b). The diagrams reveal no coherent systematics as a function of rock types, thus demonstrating that bulk rock trace element contents are not a simple function of fluid-mediated trace element loss upon antigorite dehydration. We postulate that strongly variable FME enrichments between samples dominate these patterns, given that element distribution coefficients between bulk rock residue (olivine, orthopyroxene, chlorite, magnetite, hemo-ilmenite, pentlandite, pyrrhotite) and antigorite dehydration fluid remain constant to a first order. The concept of hydration enrichment numbers is detailed in the text. (For interpretation of the references to colour in this figure legend, the reader is referred to the web version of this article.)

stage of FME redistribution took place at the antigorite dehydration reaction, by processes elaborated upon below.

5.3.3. Selected FME systematics

The overall highest bulk rock hydration enrichment numbers (Fig. 10) are displayed for Sb (up to 560) and As (up to 650), followed by B (up to 200), W (up to 60), Cs (up to 46), Li (up to 30), and in part U, Bi, In, and Sn. We now address FME systematics with emphasis on those for which data have been unavailable to date for Almirez meta-peridotites (except for some bulk rock data in Peters et al., 2017), and some of these elements have remained largely unconstrained so far for orogenic serpentinites and their derivatives.

Boron represents the most characteristic element enrichment due to ocean floor serpentinitisation (e.g., Thompson and Melson, 1970; Bonatti

et al., 1984; Scambelluri et al., 2004a, 2014; Vils et al., 2008; Boschi et al., 2008; Kodolányi et al., 2012; Deschamps et al., 2010, 2013; Cannao et al., 2016; Peters et al., 2017, 2020). Bulk rock B concentrations of Almirez hydrous mantle lithologies vary between 2 and 14 $\mu\text{g g}^{-1}$, translating into B hydration enrichment numbers of between 20 and 200 (Fig. 10). Of these, Group II Atg-serpentinites that show modest trace element enrichment via post-melting magmatic refertilization display the most pronounced B enrichments; hence, these samples display the most prominent B metasomatism upon hydration. This cannot be recognised from PM-normalised trace element distribution diagrams (Fig. 3b) because of the prominently variable magmatic Th concentrations (0.012 to 0.190 $\mu\text{g g}^{-1}$; Table A1) that translate into prominently variable pre-hydration B concentrations; the B concentrations of our samples vary much less between 3 and 15 $\mu\text{g g}^{-1}$. This

reinforces our conclusion that consideration of simple PM-normalised trace element variation diagrams may not reliably describe the systematics and extents of hydration-related FME enrichments. Therefore, hydration enrichment numbers should be used in future to better constraining fluid-mediated FME enrichment systematics.

The hydration-mediated B enrichment is mirrored by all metamorphic rock-forming silicates, including the nominally anhydrous ones (Figs. 5, 6). A first conclusion therefore is that peridotites containing olivine and orthopyroxene with prominently elevated B concentrations relative those of olivine and orthopyroxene in common mantle peridotite readily identify a history of fluid metasomatism, either ocean floor hydration associated with B and additional FME enrichment or possibly fluid infiltration in hanging-wall peridotite in the forearc (e.g., Hyndman and Peacock, 2003). For our sample suite, highest B enrichments are observed for antigorite (also compare Deschamps et al., 2010), tremolite, Ti-clinohumite, and metamorphic olivine from both brucite and antigorite dehydration (Tables A3 to A15). Of these, antigorite and metamorphic olivine dominate the silicate mineral B inventory in bulk rock Atg-serpentinite while Ol is most important for Chl-harzburgite (Fig. 9). This reflects the combined effect of efficient B uptake in serpentine minerals and the fair compatibility of B in olivine (e.g., Scambelluri et al., 2004a; Tenthorey and Hermann, 2004; and many subsequent publications). In-situ B measurements thus offer an efficient tool for testing whether a given anhydrous peridotite may have a history of geochemical exchange with the hydrosphere. Elevated B concentrations relative to PM immediately reveal that peridotite olivine and orthopyroxene are metamorphic in their genesis or, alternatively, relic mantle minerals in partially hydrated orogenic peridotites are safely identified by their low B concentrations (compare e.g., Vils et al., 2011; Kodolányi and Pettke, 2011; Peters et al., 2020).

Hydration enrichment numbers for As and Sb of up to 650 and 560, respectively (Fig. 10), prominently exceed those for B in some of our samples (and B and As correlate notably for Chl-harzburgites; Fig. 4e). Positive As and Sb anomalies in PM-normalised representation (Fig. 3b) have often been interpreted to identify the involvement of a sedimentary fluid component during (early) prograde subduction hydration (compare Hattori and Guillot, 2003, 2007; Deschamps et al., 2011; Scambelluri et al., 2014, 2019; Cannao et al., 2016; Wu et al., 2021). However, extreme As and Sb enrichments can equally be generated during hydration on the ocean floor (Andreani et al., 2014; unfortunately without data for B). Indeed, As enrichments are prominent for Almirez hydrous peridotites (up to 82 PM) but well within the range reported for mid ocean ridge serpentinites (1–300 PM; compiled in Peters et al., 2017), and significantly below the extreme As enrichments of some orogenic serpentinites (up to 2000 PM) interpreted to result from early subduction transformations involving sedimentary fluids (e.g., Hattori and Guillot, 2007; Deschamps et al., 2013). The same reasoning also applies to Sb, with concentrations of up to 82 PM that is within the range of 1 to 100 PM reported for ocean floor and forearc serpentinites (Peters et al., 2017). These Sb enrichments also compare well with the up to 30 PM reported for orogenic chlorite harzburgites and garnet peridotites from Cima di Gagnone, Switzerland (Scambelluri et al., 2014) and up to 70 PM for Atg-serpentinites from Voltri (Cannao et al., 2016). We note, however, that concentrations of As and Sb of our data set do not positively correlate with each other (not shown), suggesting that their dominant enrichment processes seem to have been decoupled or that their ultimate sources are different. Since antigorite is the most relevant host for As and Sb in Atg-serpentinites (Fig. 9), and Group II Atg-serpentinites show hydration enrichment numbers in the range of those for Chl-harzburgites (Table 2), prominent As and Sb enrichments upon ocean floor hydration are readily identified. These systematics are highly relevant as they identify an early As and Sb signal in all the Almirez rocks; metamorphic sediment dehydration fluids from deeper plate interface melanges are thus not required to account for the prominent As and Sb enrichments in our Almirez sample suite. Whatever the ultimate sources of As and Sb enrichments are - a sediment-

equilibrated pore fluid component such as emitted from serpentinite mud mounds and/or a hydrothermal fluid component and/or just seawater (compare Noll Jr. et al., 1996; Hattori and Guillot, 2007; Deschamps et al., 2010; Kodolányi et al., 2012; Andreani et al., 2014; Debret et al., 2019) - the documented enrichment in As and Sb does not result from open system antigorite dehydration associated with external fluid infiltration.

The comparatively elevated Cs concentrations notably in the prograde hydrous silicates (Fig. 5) hint at involvement of a sedimentary fluid component (e.g., Savov et al., 2007; Kodolányi et al., 2012; Kahl et al., 2015; Peters et al., 2017; Albers et al., 2020). Bulk rock concentrations of Cs and Rb display a positive trend with a Cs/Rb ratio of up to 2 (Fig. 4f) as is indicative for oceanic serpentinites from trench to shallow forearc regions (Peters et al., 2017). For ocean floor serpentinites, those from forearc settings show the most prominent enrichments in Cs (and Rb), with concentrations even exceeding PM, while passive margin serpentinites are less enriched and MOR serpentinites show consistently <10 PM concentrations that can be as low as <0.1 PM for the East Pacific Rise (discussed in Peters et al., 2017). Comparison of marine bottom water Cs/Rb ratios (~0.003 by weight; molar Cs/Rb ratios ~0.002) with those of serpentine mud mound and seamount fluid seeps (0.008–0.090 by weight; molar Cs/Rb ratios 0.005 to 0.060; Hulme et al., 2010; Wheat et al., 2020) reveal a prominent relative Cs enrichment in seep fluids. We interpret this to represent the product of variable extents of fluid - sediment exchange having occurred while the original seawater resided in porosity, from where it got progressively squeezed out with increasing confining pressure in the trench to shallow forearc at the onset of subduction (compare Stevens et al., 2021). The fact that our antigorite measurements also display elevated Cs/Rb ratios (Fig. 5a) suggests that the process of serpentinisation cannot elevate the Cs/Rb ratios reported for seep fluids as discussed above. This inference is based on the assumption that the likely loss of Cs and Rb across the chrysotile/lizardite to antigorite transition does not prominently fractionate Rb from Cs; see discussion below. Alkali element enrichment patterns therefore indicate the involvement of “sedimentary fluids” during Almirez peridotite hydration as postulated before for diverse other localities (compiled in Deschamps et al., 2013; Peters et al., 2017). Because antigorite almost exclusively hosts the Cs and Rb inventory of Atg-serpentinites (Fig. 9a-c), we again conclude that this alkali element enrichment occurred near the ocean floor, from sedimentary pore fluids, most likely in a trench (to shallow forearc) setting associated with plate bending (e.g., Ranero et al., 2003), possibly in an accretionary-wedge setting.

Because there is no trend seen between bulk rock As with Rb or Cs (not shown), chalcophile and alkali element systematics seem to be decoupled, however. We caution that addition of Cs and As to bulk rocks upon retrograde hydration might be relevant (recall discussion above), thus suggesting a “sedimentary fluid” signature that was introduced to the rocks only upon retrogression (compare Fig. 9e,f), possibly by retrograde fluids equilibrated with surrounding paragneisses. Moreover, partial loss of these FME during shallow partial dehydration reactions can be expected to be different for chalcophile and alkali elements (see discussion below). Therefore, a possible correlation between chalcophile and alkali elements indicative of a common hydration environment may have become obliterated during the subduction to exhumation cycle.

For chalcophile elements other than As and Sb, data on hydrated peridotites are scarce or absent in the literature. Our hydration enrichment numbers for Almirez bulk rocks reveal no systematic difference in Zn concentrations between Atg-serpentinite and Chl-harzburgite, with Zn concentrations near primitive mantle values. In Atg-serpentinite, Zn is dominantly hosted in antigorite and in metamorphic Ol-1, and Zn is redistributed into all antigorite dehydration reaction product minerals (Fig. 9). Hydration enrichment numbers for Zn tend to be <1 for all Almirez rock types, thus suggesting loss of some Zn upon early dehydration reactions (in analogy to Rb and Cs; discussed below).

Intriguingly, Zn does not correlate with FME except for W (without rock-type dependent trend; not shown), the driver for which remains obscure. Very good correlation exists between In and Th (Fig. 4d), thus suggesting that the In inventory in our bulk rocks is largely controlled by magmatic processes with little to no addition upon peridotite hydration. Indeed, In hydration enrichment numbers based on Th (Table 2) vary narrowly between 0.7 and 3.0, thus suggesting that modest fluid-mediated addition of In may have occurred only for some samples. To the contrast, relating In to Ce, both predicted to have closely corresponding magmatic compatibility (see X-axis in Fig. 3b), the hydration enrichment numbers $(\text{In}/\text{Ce})_{\text{meas}}/(\text{In}/\text{Ce})_{\text{PM}}$ range between 0.7 and 14, indicating significant enrichment in In that is not related to Ce (i.e., the LREE) for Group II samples (Fig. 4g). We interpret this apparent discrepancy to reveal that the degree of magmatic incompatibility of In may be much larger than its current position in the primitive mantle normalised trace element distribution diagram suggests (Fig. 3; also compare Jenner and O'Neill, 2012), possibly approaching that of Th. Clearly, more data on the magmatic systematics of rarely measured (chalcophile) elements are needed to refine our hydration enrichment number approach introduced here for determining the extents of element enrichments via fluid-mediated processes.

The few significant data for Bi are below 10 ng g^{-1} , but result in HEN of between 1 and 32, corresponding to just above PM concentrations (and concentrations are of the same range as those reported for Erro Tobbio orogenic serpentinites; Peters et al., 2020). This suggests that Bi systematics in some samples are also affected by hydration enrichment processes. The most prominent silicate hosts for Bi are antigorite and chlorite (Fig. 9), again pointing to early Bi enrichment, and orthopyroxene in Chl-harzburgite. No Cd data are available for bulk rocks; however, we note that antigorite, chlorite, and metamorphic clinopyroxene of the different growth stages returned variable concentrations of the order of tens to hundreds of ng g^{-1} (highest concentration measured at $2 \mu\text{g g}^{-1}$ for Atg-2), and metamorphic olivine and orthopyroxene around 100 ng g^{-1} (Tables A3 to A15). We interpret the observed prominent concentration variations for a given mineral growth stage to indicate that Cd may be associated with submicroscopic inclusions in all metamorphic minerals (i.e., a nugget effect) and thus suggest that these Cd mineral concentration data should be considered with caution. The few Sn data so far reported for ocean floor serpentinites are of the order of a few tens of ng g^{-1} except for some higher outliers (Kodolányi et al., 2012; Jöns et al., 2010), and our data for Almirez are comparable. HEN range between 0.6 and 11 and are highest for Chl-harzburgite, and Sn displays a small positive anomaly in PM-normalised representation. This suggests that Sn may possess a contribution from ocean floor hydration too, a hypothesis supported by the observed positive trend between As and Sn concentrations (not shown). Due to lack of data, we cannot assess which silicate minerals are the most important sinks for Sn in our rocks. Data are too scarce for Tl (Table A3 to A15) for robust interpretation except for the fact that Almirez orogenic peridotites do not record enrichments relative to PM and that scattered chlorite and antigorite measurements returned Tl concentrations of the order of 1 ng g^{-1} . Altered MORB data displayed the highest enrichment factors relative to fresh MORB for Sb and Tl (Jochum and Verma, 1996). While prominent Sb enrichments are demonstrated for ocean floor and orogenic serpentinites, our Tl data reveal the absence of a comparable enrichment in Tl for the Almirez hydrous peridotites. On the other hand, the modest enrichment in Sn upon MORB alteration reported by Jochum and Verma (1996) is also present in our Almirez samples. Clearly, more data are required for chalcophile elements, most importantly in relation to the sulphur geochemical cycle (compare Alt et al., 2013).

Data for Pb in oceanic serpentinites are inconclusive. Some authors report bulk rock enrichments in Pb that are interpreted to be due to ocean floor serpentinisation (e.g., Deschamps et al., 2011), while data for other ocean floor serpentinites reveal little to no enrichment relative to elements of similar compatibility during mantle melting, except for serpentinites from forearc settings, consistent with in-situ mineral

measurements (e.g., Kodolányi et al., 2012). We hypothesize that high Pb concentration data for oceanic serpentinites might be largely caused by contamination during sampling (e.g., drilling); if correct, then Pb is not prominently enriched upon mantle hydration (in line with Niu, 2004 and bulk rock IODP serpentinite data presented in Pettke et al., 2018). Mineral data reveal that metamorphic clinopyroxene (Cpx-2), when present, is a relevant host for Pb in Atg-serpentine, while the Pb inventory in Chl-harzburgite is dominated by retrograde low-T serpentine (Fig. 9). Our data thus reveal that retrograde hydration may add significant fractions of Pb to bulk hydrous peridotite; hence, bulk rock Pb isotopic data of such samples should be interpreted with much caution and may simply be misleading when trying to constrain the history from hydration to peak metamorphism.

Prominent W enrichments in ocean floor serpentinites (Babechuk et al., 2010; Kodolányi et al., 2012; Peters et al., 2017) and in partially dehydrated equivalents (Scambelluri et al., 2014; Gilio et al., 2019, 2020; Peters et al., 2020) have become documented only recently, and W concentrations of Almirez rocks are comparable, with hydration enrichment numbers of between 1 and 100 (Table 2; Fig. 10). However, W abundances do not correlate with other FME; hence, W enrichment processes remain elusive. Because antigorite dominates the W inventory of Atg-serpentinities (Fig. 9a-c), we imply that W enrichment in Almirez hydrous peridotites mainly resulted from oceanic serpentinisation as concluded for the other FME. The oceanic enrichment process had to be very effective, since W concentrations in seawater are very low at below-levels (GERM reservoir data base, 2021); hence, an intermediate W enrichment step via adsorption to (sediment) particles may be required. Our data further reveal that Ti-clinohumite contains by far the highest W concentrations (Tables A3–A15), while oxide minerals only contain of the order of $0.1 \mu\text{g g}^{-1}$ W (Vieira Duarte et al., 2021). A possible correlation of W with other elements in bulk rocks might thus be masked by sporadic occurrence of tiny Ti-clinohumite crystals, i.e., a nugget effect for bulk rock samples. In Chl-harzburgite, orthopyroxene and inclusion-rich Ol-3 host most W (Fig. 9d,e) and here again, variable amounts of inclusions might thus add scatter to the W data. Finally, low-T retrograde serpentine can contain significant bulk rock W fractions, which again implies low-temperature fluid mobility of W.

Strong positive anomalies are observed for Li in metamorphic olivine (Fig. 6) that represents the most important host mineral for Li in all hydrous peridotite bulk rock types, along with antigorite (Fig. 8). Bulk rock samples display no significant Li anomalies for Group I samples while Group II samples display prominent positive anomalies (Fig. 3b). Hydration enrichment numbers of between 0.8 and 30 reveal that peridotite hydration processes can enrich Li, but that such enrichments may be masked by prominently variable Li enrichments during magmatic refertilization. This has been reported for ocean floor serpentinites where trench to forearc serpentinites tend to show largest degrees of enrichments (Kodolányi et al., 2012; Vils et al., 2008). These competing processes of Li enrichment render the interpretation of positive Li anomalies in PM-normalised representation very difficult, let alone the interpretation of Li isotopic ratios of hydrated peridotite bulk rocks. Wunder et al. (2010) reported opposite Li isotope fractionation trends between specific serpentine minerals and water. For chrysotile - water, heavy ^7Li tends to partition into the chrysotile, while for lizardite - water and antigorite - water, the heavy ^7Li stays preferentially in the fluid, with $\Delta^7\text{Li}$ values following a T-dependent fractionation trend. Because oceanic serpentinisation can produce variable chrysotile-lizardite mixtures, variability in $\Delta^7\text{Li}$ bulk oceanic serpentinite values are to be expected; hence, interpretation of orogenic serpentinite $\Delta^7\text{Li}$ data remains underconstrained because the starting $\Delta^7\text{Li}$ of bulk oceanic serpentinite remains a priori unknown.

5.3.4. Different types and origins of sedimentary fluids

Serpentinisation along with FME enrichments in MOR settings demonstrates that peridotite metasomatism can take place in virtually sediment-free environments, driven by seawater infiltration.

Sedimentary fluids represent another relevant serpentinising agent, generally invoked to account for elevated alkali trace element contents combined with enrichments in As and Sb as evident from the above discussion and as most recently reviewed in Scambelluri et al. (2019). The discussion above also used sedimentary fluids as source identification; however, what exactly are sedimentary fluids? Indeed, the term sedimentary fluids is used in the literature with highly diverse genetic connotations and resulting geological implications; hence, a clear definition and discussion of what exactly the term sedimentary fluids refers to is needed first in order to better constrain prevailing hydration environments.

Sedimentary fluids can be understood as any mixture of two end members, and the transition between endmember 1 and 2 is gradual with progressive burial (diagenesis) and initial subduction. Endmember 1 are pore fluids chemically equilibrated with the unconsolidated ocean floor sediment, i.e., chemically different from ambient seawater. Sedimentary pore fluids get progressively expelled via simple compaction with increasing burial when the sediments approach the subduction suture (e.g., accretionary wedges and beneath). Importantly, these fluids represent water that is not structurally bound to minerals. Consequently, such water can be freely exchanged, permeability permitting; hence, the processes of fluid liberation from a given rock package are independent of mineral transformations and can occur at any time, from ocean floor settings to shallow forearc depths.

Endmember 2 is lattice bound water in hydrous minerals of sedimentary rocks, the largest fraction contained in clay minerals and opal. Sediments approaching the subduction suture experience mineralogical transformations with increasing temperature (and less so pressure) that can be summarised as diagenesis preceding subduction metamorphism. Opal dehydration occurs first, at somewhere between 30 and 80 °C, followed by smectite dehydration and the smectite to illite transformation at ca. 80–150 °C (e.g., Hyndman and Peacock, 2003; Kastner et al., 2014). Sediment components are diverse as a function of geological setting, including clastic materials with volcanoclastic sediments from MOR and arc magmatism (the latter notably relevant in intraoceanic trenches) and their alteration products rich in clays, biogenic materials (siliceous and carbonate), and chemical precipitates (e.g., Plank and Langmuir, 1998). Because lattice-bound water contents in minerals tend to overall decrease with increasing T during diagenetic to metamorphic reactions, prograde mineral transformations are generally water-producing.

Fluid trace element concentrations present in the trench to shallow forearc environment - while variable in detail (that is beyond the scope of this paper) - share important characteristics. Pervasive presence in rocks maximises wetting of mineral surfaces, thus facilitating fluid-solid equilibration, for dehydration reactions specifically with the product mineral assemblage. Consequently, “sedimentary fluids” tend to be rock-buffered, and sedimentary fluids can therefore be expected to mirror sediment composition to a first order. Bulk sediment hydraulic gradients with increasing burial are inside-out, and fluid migration is likely pervasive, initially dominated by compaction-induced pore fluid expulsion, then sustained by diagenetic opal and smectite dehydration and smectite to illite transition (Tremosa et al., 2020). For cases where anisotropic deformation may induce preferred fluid migration pathways, e.g., along faults, focused fluid flow can predominate and pervasive fluid-rock equilibration may thus no longer be achieved; hence, the extent of sedimentary fluid imprint on rock can be expected to decrease away from the fault interface (e.g., Barnes et al., 2014).

Measurements of fluids emanating from serpentine mud volcanoes (e.g., Fryer, 2012) offer a window on their compositions (e.g., Hulme et al., 2010; Mottl et al., 2004), in addition to clasts and matrix materials “erupted” from such mounds that show a multistage hydration history (e.g., Savov et al., 2005, 2007; Kahl et al., 2015; Albers et al., 2020). Kahl et al. (2015) propose that early opal and smectite dehydration produce quartz-saturated fluids with high FME contents that cause the early pervasive serpentinisation in shallow parts near the trench. Later

serpentinisation stages occur at greater depths, are more localised, and the resulting serpentine growth stages possess lower FME concentrations that lack a prominent sedimentary geochemical signal (also reported by Albers et al., 2020). The Cs/Rb ratio of successive growth stages of serpentine minerals in these shallow environments is prominently elevated and evolves from 0.25 and 1 in early stages to near 0.1 in later stages, interpreted to be linked to increasing temperature of serpentinisation (Kahl et al., 2015; Albers et al., 2020). Because sediment pore waters have prominently elevated Cs/Rb ratios when compared to bottom seawater (Mottl et al., 2004), approaching that of typical subducted sediments ($Cs/Rb_{GROSS} \sim 0.06$; Plank and Langmuir, 1998), shallow, pervasive serpentinisation is expected to produce high Cs/Rb serpentinites. Our Almiraz bulk serpentinite Cs/Rb ratios vary narrowly between 0.6 and 1.7. Assuming that prograde dehydration did not prominently fractionate the Cs/Rb ratios, this Cs/Rb signature reinforces our implication that addition of a “sedimentary fluid” signature occurred early in the hydration history of Almiraz rocks, most likely in an ocean floor (including trench) setting. We propose sediment-equilibrated pore fluids as the likely source. Our conclusion is in line with halogen concentration data presented by Kendrick et al. (2013). These authors report that abyssal and passive-margin serpentinites display I/Cl and Br/Cl ratios close to seawater, while forearc serpentinites display a progressive shift in their I/Cl and Br/Cl ratios towards sedimentary pore fluids. We note that smectite and opal dehydration is widely accepted to cause ubiquitous pore water freshening (i.e., dilution of the pore water solute load) at convergent margins (e.g., Brown et al., 2001; Hüpers and Kopf, 2012). FME imprint from deeper dehydration sources thus seems not to have the capacity to significantly modify the initial FME systematics of serpentinite on the bulk rock scale.

Another relevant question concerns the mass proportions of pore fluids and mineral dehydration fluids released from sediments at shallow depths. Fluid-filled porosity in near-surface oceanic sediments amounts to tens of percent by volume, depending on sediment grain size and grain shapes. Porosity then exponentially decreases with burial depth (i.e., compaction) to be of the order of 20–40 vol% at 2 km depth (Kominz et al., 2011). In comparison, lattice-bound water in sediments is well below such amounts, and it also decreases with progressive mineral transformation. Sediment compaction thus releases the largest mass of fluid, also documented by Stevens et al. (2021) for sediments of the North Sumatra Subduction trench. Consequently, we consider sedimentary pore fluids to be much more relevant as a hydration agent than metamorphic dehydration fluids from sediments at depth exceeding some 20 km, an implication perfectly in line with our combined evidence for dominant FME enrichments in our samples prior to antigorite crystallisation.

Rate estimates on masses of subducted sediment and notably serpentinites are highly uncertain, and beyond the scope of this paper. It can be expected, however, that pore water expulsion dominates by mass over lattice-bound water liberation from sediments during subduction to some 10 km depth (e.g., Stevens et al., 2021). Moreover, diagenetic opal dehydration and smectite to illite transformation results in an overall dilution of pore fluid FME concentrations as reported above. Together, this suggests that sedimentary trace element signatures in serpentinites may largely be due to serpentinisation induced by sedimentary pore fluids expelled upon early compaction rather than via mineral dehydration fluids. Von Huene and Scholl (1991) have estimated the rate of pore fluid expelled from sediment at the onset of subduction to be $\sim 0.9 \text{ km}^3/\text{a}$. Assuming that all the sedimentary pore fluid would be consumed for serpentinisation, $\sim 3.3 \text{ km}^3$ serpentinite would be produced per year. At a global subduction rate of $\sim 3.4 \text{ km}^2/\text{a}$ (equalling the global oceanic plate production rate; Parsons, 1982), this would translate into a $\sim 1 \text{ km}$ thick serpentinite layer of the globally subducting oceanic lithosphere, including notably that from fast spreading settings. This simple calculation demonstrates the potential of sedimentary pore fluids for serpentinisation in oceanic to trench to shallow forearc settings.

Assuming that significant peridotite hydration does occur from

mixtures of sedimentary pore fluids and diagenetic dehydration fluids in trench settings, the question then arises how this happens. Existing serpentinites are unlikely to acquire a sedimentary fluid trace element signature because fluid rock chemical exchange is strongly limited for the serpentinite mineralogy that is already at equilibrium with water. Only prograde mineral transformations may offer an opportunity for addition of another FME source component to existing serpentinites, e.g., the transition between lizardite/chrysotile to antigorite (e.g., Deschamps et al., 2011; Zhang et al., 2019) when triggered by fluid-mediated SiO₂ advection (Evans, 2004; eq. 1b above). However, trace element data on coexisting lizardite/chrysotile and antigorite so far available suggest that alkali elements are lost from the system during this reaction (see below; Kodolányi and Pettke, 2011; Debret et al., 2014) occurring somewhere between 300 and 400 °C (e.g., Schwartz et al., 2013). Consequently, pristine peridotite hydration by sedimentary (pore) fluids remains to be the likely process for producing serpentinites with a sedimentary source signature.

Sedimentary fluids are often invoked to hydrate peridotite in a hanging wall mantle wedge setting (e.g., Hyndman and Peacock, 2003; Scambelluri et al., 2010; Deschamps et al., 2010, 2011; Zhang et al., 2019). Another possibility is hydration of fresh peridotite masses tectonically mingled into the plate interface regions where sediments can be assumed to be abundant. This second scenario is hard to conceptualise, however, because slab mantle rock slivers are likely to have been serpentinitised already in ocean floor to trench settings and then become concentrated in plate interface melanges. Regarding orogenic serpentinites, they are commonly associated with rodingites (for Almirez, e.g., Trommsdorff et al., 1998), thus unequivocally identifying ocean floor serpentinitisation as opposed to mantle wedge serpentinitisation; hence, most orogenic serpentinites that we can sample originate from the subducting slab. As a consequence, one can expect a predominance of slab serpentinites in the total mass of subducted serpentinites. This is in apparent conflict with numerous literature reports (e.g., Hattori and Guillot, 2003; Lafay et al., 2013; Scambelluri et al., 2014; Cannao et al., 2015, 2016; reviewed in Scambelluri et al., 2019) based on orogenic serpentinite trace element systematics that postulate sediment dehydration fluids from greater depths to have been involved in the genesis of orogenic serpentinites. This conflict can be defused by concluding that most serpentinites displaying sedimentary fluid trace element systematics are the product of oceanic serpentinitisation via sediment-equilibrated pore fluids, most likely in trench to shallow forearc settings, as opposed to deeper sediment dehydration fluids. Petrology combined with trace element systematics support this interpretation for Almirez hydrous ultramafic rocks as elaborated upon above. Another possibility is that much of the geochemical characteristics of hydrous peridotites interpreted to represent sediment dehydration fluid imprint can actually be produced from seawater alone (e.g., As and Sb enrichments to above PM concentrations) as discussed above, also consistent with the early FME imprint in these rocks. We interpret the combined evidence so far presented to indicate that oceanic peridotite hydration and associated metasomatism is much more relevant than so far acknowledged - be it by seawater or by sediment-equilibrated pore water - and serpentinitisation triggered by metamorphic sediment dehydration fluids generated along the subduction plate interface may be a much more special case (e.g., forearc peridotite hydration), notably when the bulk mass of subducted serpentinite is considered.

5.4. Fluid-mediated element loss with progressive subduction of hydrated ultramafic rocks

Assessing FME loss upon partial dehydration of subducting serpentinites is challenging because fluid/mineral element distribution coefficients are largely lacking for the relevant dehydration reactions. To circumvent this problem, the approach so far chosen in literature has been to compare data of reactant rocks with product rocks for a given metamorphic reaction, often from various localities across a mountain

range. Many studies implied an overall loss of certain FME to the dehydration fluid (e.g., Scambelluri and Philippot, 2001; Scambelluri et al., 2001, 2004b, 2015; Hattori and Guillot, 2003; Kodolányi and Pettke, 2011; John et al., 2011; Lafay et al., 2013; Zhang et al., 2019), in part corroborated by quantitative LA-ICP-MS measurement data obtained on fluid inclusion relics hosted in olivine crystallised as an antigorite breakdown product (e.g., Scambelluri et al., 2004a, 2004b, 2015).

Almirez has become the type locality to constrain fluid-mediated element losses or possibly gains across the antigorite dehydration reaction, by simple comparison of bulk rock compositions for reactant Atg-serpentinites and product Chl-harzburgites that crop out adjacent to each other. However, the work of Bretscher et al. (2018) revealed for Almirez that variable compositions resulting from variable extents of ocean floor hydration and associated metasomatism (also compare Fig. 3b) are the cause for the coexistence of antigorite dehydration reactant and product rocks next to each other in a coherent subducted rock unit. Our work corroborates these findings and demonstrates prominent trace element variations including FME in the same rock samples studied by Bretscher et al. (2018), resulting from combined pre-hydration magmatic processes and variable hydration-related FME enrichments. Obviously, the simple comparison between reactant and product bulk rock compositions to deriving fluid-mediated element fluxes across antigorite out may thus offer very first order trends at best. However, such an approach can be seriously misleading as will be demonstrated below.

The concept of hydration enrichment numbers introduced in this work strongly reduces the above limitations and ambiguities since intra-sample systematics are investigated and quantified rather than inter-sample variations; therefore, net FME loss (i.e., element loss dominates over element gain upon hydration) during progressive subduction can be identified more reliably. Our approach is generally applicable to cases where direct compositional measurements of fluid inclusion relics are unavailable. Fig. 10 displays hydration enrichment numbers < 1 notably for the FMEs Ba and Rb, thus revealing prominent deficits in LILE relative to the incompatible and fluid-immobile Th. Intriguingly, most of the Atg-serpentinite samples also display hydration enrichment numbers below 1 for Rb, Ba, Sr, and Zn, indicative of up to 94% loss for Rb, the highest apparent loss being recorded for Atg-serpentinite samples. Two scenarios are possible to account for these observations.

The most prominent prograde loss of Rb, Ba, Sr, and Zn may occur upon antigorite crystallisation from lizardite/chrysotile. The PM-normalised trace element distribution pattern for antigorite (Fig. 5a) indeed displays negative relative anomalies for Ba, Sr, and less so for Rb, thus indicating the possibility that these elements do not fit well into the antigorite structure and are therefore left over in the fluid associated with prograde antigorite crystallisation from lizardite/chrysotile. We interpret the decrease in FME concentrations across the lizardite/chrysotile to antigorite transition reported by Zhang et al. (2019) to corroborate our inference. In simple words, antigorite may not represent a sink for Ba, Sr, and Rb; hence, these elements may escape with the fluid.

Alternatively, HEN < 1 might also identify loss of Rb and Ba relative to Th from the melt prior to magmatic refertilization (in analogy to Eu that is scavenged by plagioclase fractionation prior to melt-rock reaction as discussed above). While Ba might be incorporated in plagioclase, plagioclase does not represent a sink for Rb. Therefore, this hypothesis is not likely.

Consequently, we interpret HEN < 1 for Rb, Ba, and Sr to be largely governed by loss from the rocks upon early prograde mineral reactions in the presence of fluid. Because HEN for Rb and Ba do not systematically differ between Atg-serpentinites and Chl-harzburgites (Fig. 10; however, ranges are large), the most prominent loss of Rb, Ba, and Sr seems to have occurred already prior to antigorite dehydration. This is consistent with in-situ measurement data for Rb, Sr, and B in ocean floor mesh serpentine that showed higher concentrations than antigorite crystallising therefrom (Kodolányi and Pettke, 2011), and with loss of B

and Li upon early subduction metamorphic lizardite to antigorite transition (Vils et al., 2011). For Zn we note that hydration enrichment numbers are commonly also below 1 (Fig. 10b), thus suggesting early fluid-mediated loss of Zn from Atg-serpentinite and Chl-harzburgite samples as for Rb, Ba, and Sr. Another possibility is a scenario in which the Atg-serpentinites now dehydrated to Chl-harzburgites initially contained prominently higher FME concentrations resulting from hydration metasomatism. This hypothesis is supported by high Sr and Ba concentrations in olivine-hosted fluid inclusion relics of Chl-harzburgites (Scambelluri et al., 2004b). These systematics demonstrate that part of the Sr and Ba inventory of reactant Atg-serpentinite was lost to the dehydration fluid, thus suggesting that the Sr and Ba concentrations of former Atg-serpentinite now reacted to Chl-harzburgite were considerably higher than those measured in still existing Atg-serpentinite.

Contrary to the example just presented, element gain upon peridotite hydration at the ocean floor dominates over likely and variable loss upon partial serpentinite dehydration for all other FME as revealed by $HEN \gg 1$ for our samples. In other words, hydration enrichment numbers above 1 cannot help in constraining prograde FME loss during specific dehydration reactions, simply because the initial FME enrichments of a given sample remain unconstrained. Hydration enrichment numbers thus provide a minimum value for the initial trace element enrichment upon peridotite hydration. The following evidence from the literature offers insight into which elements were likely lost in part from our rock samples along with Rb, Ba, Sr, and probably Zn during progressive subduction. Across the transformation of chrysotile/lizardite to antigorite, Kodolányi and Pettke (2011) documented about 90% loss of Cl, more than 80% of B, about 50% of Sr, and loss of some Rb, while Li remained uniform, based on in-situ measurements of neighbouring reactant and product serpentine minerals in one thin section. To our knowledge, no robust data are available for FME loss across the brucite+antigorite dehydration reaction. We note here that brucite seems not to be relevant on a bulk rock scale for the FME budget because of its rather low FME concentrations (e.g., Kodolányi et al., 2012). And antigorite consumed upon brucite dehydration only represents a variably minor fraction of total antigorite in Atg-serpentinites. Consequently, brucite dehydration can be expected to not significantly affect the trace element budget of Atg-serpentinites to a first order. Indeed, brucite dehydration veins in Atg-serpentinites from Erro Tobbio (Scambelluri et al., 1995) display bulk trace element compositions largely mirroring the enrichment patterns of host Atg-serpentinites (Peters et al., 2020). This is actually expected since vein mineralogy is identical to that of enclosing Atg-serpentinites; hence, both the host rock and the vein minerals represent the residual mineral assemblage after the rock-buffered dehydration fluid escaped from the system. While mineral compositions in host rock and vein material can be expected to be similar because these are governed by fluid mineral element distribution coefficients at reaction pressure - temperature - reactive bulk composition (PTX) conditions, compositional bulk variations between olivine-bearing Atg-serpentinite and brucite dehydration veins are likely because of significant variations in mineral modes between host rock and veins. Compositional data for bulk veins or vein minerals representing fluid drainage pathways from dehydration thus offer no direct constraints on the mobility of FME at the relevant hydration reactions unless fluid-mineral element distribution coefficients become known for these PTX conditions.

The antigorite dehydration reaction has attracted most interest as it represents the arguably most prominent fluid liberation step in deep subducting oceanic lithosphere, notably for slow-spreading lithosphere. Fluid inclusion relics from Almirez measured by LA-ICP-MS returned elevated signals for Ba, Rb, Cs, Pb, Sr, and LREE (Scambelluri et al., 2001), thus documenting that antigorite dehydration fluids have the capacity to mobilise some incompatible trace and light rare earth elements at subduction zone conditions. Antigorite + chlorite dehydration fluids were measured as fluid inclusions in experimental run product

olivine by Spandler et al. (2014) who reported significant fluid mobility of Cs, Ba, B, Sr, and Pb, consistent with experimental data obtained from diamond traps hosting antigorite dehydration fluid with variably high contents of Cs, Ba, B, Sr, Pb, Li, As, Rb, and U (Tenthorey and Hermann, 2004). Quantitative element concentration data for antigorite dehydration fluid inclusion relics from Almirez document significant loss of B, Sr, Ba, Rb, Cs, and Pb along with Na, K, Ca, (Scambelluri et al., 2004b), and the same elements plus Li, As, Sb, LREE, Tl, and U were mobilised at comparable temperatures along a cooler geotherm in case of antigorite dehydration at Cima di Gagnone (Scambelluri et al., 2015). This combined evidence implies that antigorite dehydration fluids mobilise significant fractions of the serpentinite budgets in Cs, Rb, Ba, Sr, Pb, B, Li, and As, consistent with data in this work for inclusion-bearing Ol-3 from spinifex textured Chl-harzburgites that show distinct enrichments in most of these elements relative to inclusion-free Ol-4 (Fig. 6). Consequently, the hydration enrichment numbers for these elements in Chl-harzburgite (Table 2; Fig. 10) represent variably prominent underestimates of their true extents of initial hydration enrichment.

For the case of Almirez, Chl-harzburgite bulk rock samples should thus have variably lower FME concentrations on average when compared to the adjacent Atg-serpentinites, given the assumption that these rocks received similar FME enrichments upon hydration. However, FME concentrations overlap or reveal even contrary trends for our sample suite. Average Chl-harzburgites (both textural types) tend to have prominently higher concentrations in Cs, Rb, U, In, Sr, and Li, along with the highest relative enrichment for fluid immobile Th, Ta, (Fig. A4) when compared to Atg-serpentinite. Conversely, the fluid immobile LREE display lower average concentrations in Chl-harzburgite when compared to Atg-serpentinite, resulting from the prominent melt-rock reaction enrichment of group 1 Atg-serpentinites (Fig. 3; discussed above). These compositional differences again emphasize that simple comparison between reactant and product rocks can lead to erroneous conclusions on fluid-mediated element loss across a given dehydration reaction because the initial variability in trace element budgets including FME of the individual rock samples may outweigh fluid-mediated element loss imposed upon partial dehydration. Our hydration enrichment numbers for the 5 serpentinite samples (compare Table 2; Fig. 10) illustrate this well. For example, Atg-serpentinite hydration enrichment numbers for Sb vary between 8 and 515, thus essentially encompassing the range of our entire sample set; hence, inter-sample variability in Sb enrichment dominates in our sample set. Literature claims (e.g., Garrido et al., 2005; Marchesi et al., 2013; Debret et al., 2021) for element enrichments associated with the antigorite dehydration reaction by simple comparison of reactant Atg-serpentinite and product Chl-harzburgite and invoking open system processes, i.e., enrichments via fluid advection, are thus likely to be incorrect, notably for fluid-immobile elements such as the HFSE. FME are certainly lost from subducting hydrous ultramafic rocks, but how much of the bulk rock total inventory is lost at a specific dehydration reaction via fluid escape can only be quantified reliably once element distribution coefficients between product phases including the aqueous fluid at relevant PTX will become available.

5.5. Trace element enrichment related to serpentinisation during prograde reactions upon subduction

Many studies (e.g., Hattori and Guillot, 2007; Deschamps et al., 2010; Lafay et al., 2013; Scambelluri et al., 2014, 2019; Cannao et al., 2015, 2016; Schwarzenbach et al., 2018a; Gilio et al., 2020; Wu et al., 2021) have advocated that fluid-mediated fertilisation of the hydrous mantle rocks occurred during progressive subduction, including upon antigorite dehydration (Garrido et al., 2005; Marchesi et al., 2013; Kendrick et al., 2018; Debret et al., 2021). We consider this to be well possible for ultramafic rock slivers embedded in melanges along the subduction plate interface (several of the above studies dealt with such

sample material). However, constraints on the extents of prograde element enrichment for any orogenic hydrous peridotites as derived from trace element concentration variations are vague at best given the strong limitations just discussed. Moreover, retrograde overprint may result in variably prominent FME additions to bulk rock data (detailed above) the potential for which is highest along high-permeability fault zones including the subduction plate interface. Because of all these uncertainties associated with trace element concentration systematics, we now explore how selected literature isotope data may help in identifying multiple source components in hydrous peridotites.

Isotope ratios such as $\delta^{34}\text{S}$ (Alt et al., 2012, 2013; Schwarzenbach et al., 2018a, 2018b) or $^{87}\text{Sr}/^{86}\text{Sr}$ signatures are promising for positively identifying fluid rock interaction upon early subduction following ocean floor serpentinisation. Among these, heavy radiogenic isotope systems are most promising because significant mass-dependent isotopic fractionation during the history from ocean floor hydration to subduction and exhumation is absent, contrasting classical light stable isotopes and even non-traditional stable isotopes like Zn (Debret et al., 2021). For example when measured radiogenic Sr isotope ratios are higher than that of seawater at the time of ocean floor serpentinisation, a crustal contribution has commonly been inferred (see e.g., Cannao et al., 2015, 2016, for examples), so the question remains at which stage during the hydration - subduction - exhumation cycle this crustal signature was added to the rock and what exactly it represents. We first note that diagenesis tends to elevate Sr isotopic ratios of impure marine carbonates relative to their seawater values (Banner, 1995). By inference, sediment-equilibrated pore fluids can thus be expected to be variably more radiogenic than ambient seawater; hence, sediment dehydration fluids may not be required to account for slightly elevated Sr isotopic signatures of subducted serpentinites. The modest elevations documented in the $^{87}\text{Sr}/^{86}\text{Sr}$ data set of Harvey et al. (2014) for Almirez ($^{87}\text{Sr}/^{86}\text{Sr} = 0.7075$ measured in Chl-harzburgite to 7087 measured in Atg-serpentinite) relative to then-existing seawater (~ 0.7075) can be accounted for by involvement of oceanic sediment-equilibrated pore fluids and therefore does not require interaction with subduction dehydration fluids. Very likely, interaction with oceanic water alone (seawater and sediment-equilibrated pore fluids) pervasively hydrated the Almirez peridotites, before these serpentinites entered the subduction-plate interface domain.

Combining bulk rock trace element data with Sr isotope systematics, Cannao et al. (2016) reported an example from Voltri Massif where massive serpentinites preserving oceanic hydration fingerprints are embedded in mylonitic serpentinites with “elevated” As and Sb contents (note that the scatter in FME concentrations of mylonitic serpentinites, their Table 1, often envelopes those of static serpentinites, however) along with more radiogenic Sr and Pb isotopic signatures. The authors concluded that acquisition of the sedimentary signature in localised deformation domains certainly occurred prior to eclogitic metamorphism and may have happened either in an outer-rise zone setting or in a shallow subduction channel domain. Strontium isotope data for lizardite and antigorite serpentinites from North Qaidam, Tibet, were interpreted to identify fluid-mediated radiogenic Sr addition upon the lizardite to antigorite transformation (Zhang et al., 2019). However, bulk sample inventories of Cs, Rb, Ba, and Li are higher in lizardite serpentinite than in Atg-serpentinite, which we interpret to indicate addition of this sedimentary Sr isotope signal along with sediment-indicative FME well before the lizardite to antigorite transition, likely from sedimentary pore fluids. In another example, Sr isotope systematics were interpreted to reveal significant crustal influence for Cima di Gagnone metaperidotites (Cannao et al., 2015) as has been proposed on the basis of Be enrichments in bulk rocks (Scambelluri et al., 2014). Yet another example reports on hanging wall peridotite infiltration by slab derived fluids with Sr isotopic compositions more radiogenic than that of contemporaneous seawater (Cluzel et al., 2020). It is this last scenario that can offer excellent opportunities to better constrain metaperidotite refertilization upon early subduction, provided that independent

constraints can be put forward for a mantle wedge peridotite hydration setting including forearcs.

Lead isotopes were also employed following the reasoning above. In this context we recall that Pb isotopic ratios are extremely delicate to interpret, because they are highly prone to retrogression - retrograde serpentine dominates the bulk rock Pb inventory of Chl-harzburgite (Fig. 9d,e) - and because measured Pb isotope ratios need to be corrected for in-situ radiogenic ingrowth since the establishment of variably extreme U/Pb abundance ratios upon ocean floor hydration (compare e.g., Niu, 2004; Pettke et al., 2018), the timing of which is often not well constrained either.

All the above examples used bulk rock isotope data, and many of the elements have been identified here to display highly complex histories starting with melt refertilization prior to oceanic hydration and ending with rehydration-associated addition upon exhumation. A much more reliable approach therefore is to use in-situ isotope data, because a direct link between petrology and isotope data can be established in the same way as for trace element systematics; however, potential elements are present at trace concentrations only, thus rendering this approach highly challenging. Sulphur and hydrogen/oxygen isotopes are an exception and address two complementary systems in the rocks, the silicates whose stabilities are dictated by the PTX evolution while the sulphides sensibly respond to the redox evolution of the rock in addition to PTX (e.g., Evans, 2012, and many subsequent contributions). Retrograde sulphide addition represents a serious danger for bulk rock $\delta^{34}\text{S}$ data (compare Schwarzenbach et al., 2018a; Su et al., 2019), so in situ measurements are required to address the prograde S isotope systematics in hydrous ultramafic rocks.

6. Lithosphere-scale model for slab serpentinisation and subduction evolution

Integration of the above findings allows to deducing a lithosphere-scale geochemical model for slow-spreading ocean floor encompassing peridotite evolution from melt depletion to magmatic refertilization to ocean floor hydration to modification upon partial dehydration during subduction and final exhumation, sketched in Fig. 11. To do so, we employ three end-member serpentinite settings and trace their histories.

- (1) Serpentinites formed near the ocean floor exemplified here by Almirez. These rocks formed at variably high fluid/rock ratios, and are fully serpentinised and moderately to strongly oxidised on average.
- (2) Serpentinites formed near the hydration front deeper in the lithosphere, e.g., near mid ocean ridge or at bend fault settings, or possibly in hanging wall wedge peridotites from fluids circulating along the subduction plate interface. These are exemplified by Erro Tobbio serpentinites (Peters et al., 2020). These rocks formed at overall low fluid/rock ratios at rock-buffered conditions, and are variably hydrated (i.e., may still contain relic mantle minerals) and moderately oxidised to reduced.
- (3) Serpentinite lenses embedded in oceanic sediments, tectonically assembled at the base of the accretionary wedge or possibly later during prograde subduction and typically located in the subduction plate interface melange (as exemplified by the Franciscan Complex or the Schistes Lustrés complex). These rocks are fully serpentinised, often strongly oxidised, formed predominantly from sediment-equilibrated fluids at variably high fluid/rock ratios, and generally possess prominent re-equilibration upon retrogression.

Ocean floor serpentinisation can occur near mid ocean ridges, at oceanic core complexes, along passive continental margins, and along transform faults (Fig. 11a, setting 1; e.g., Cannat, 1993; Agrinier and Girardeau, 1988; Früh-Green et al., 2018). With progressively deeper peridotite infiltration, the hydration environments evolve from fluid-

buffered (high fluid/rock ratio) and oxidising near the lithosphere - water interface towards more and more rock-buffered (low fluid/rock ratio) and weakly oxidising to strongly reducing conditions when approaching the hydration front (e.g., Alt and Shanks, 1998). Despite strong inter-sample variation documented here for Almirez and reported elsewhere, setting (1) can be characterised by variable but modest relative SiO₂ enrichment (displacing bulk rock data to below the melt depletion trend in a Al₂O₃/SiO₂ vs. MgO/SiO₂ diagram; Fig. A1) along

with CaO depletion (for Almirez rocks see Marchesi et al., 2013; Bretscher et al., 2018) and prominent enrichments in B, As, Sb, and W as quantified here by hydration enrichment numbers (Fig. 10). Lower, variable enrichment levels are recorded for Cs, Rb, Li, Bi, In, ±Pb, and importantly for the redox-sensitive U, thus documenting that fluid fO₂ was already approaching rock-buffered conditions for some Almirez samples.

When approaching the hydration front (setting 2), SiO₂-neutral,

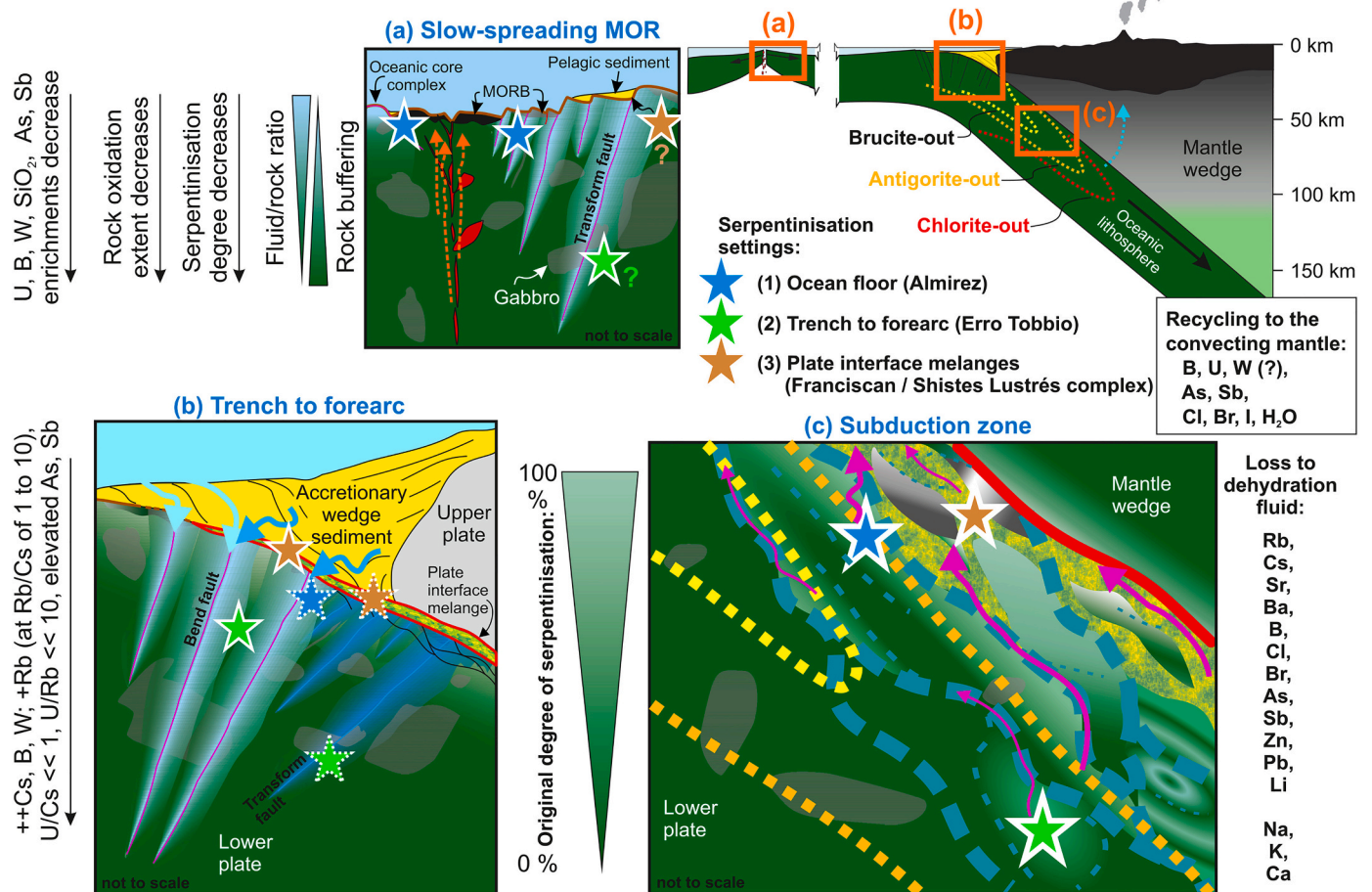


Fig. 11. Conceptual model for slow-spreading oceanic lithosphere from mid ocean ridge (MOR) to subduction. Three exemplary serpentinite units characteristic of relevant serpentinisation environments are portrayed: (i) Oceanic serpentinisation by seawater infiltration near the seawater-peridotite interface (Almirez, this work, blue star), (ii) serpentinisation near the hydration front, likely along deep transform faults or in bend faults in trench settings (Erro Tobbio, e.g., Peters et al., 2020, green star), and (iii) serpentinisation by sedimentary (pore) fluids dominantly in trench to forearc settings and in plate interface melange domains (e.g., Franciscan or Schistes Lustrés Complex, e.g., Lafay et al., 2013, brown star). (a) Initial serpentinisation takes place at the MOR, at oceanic core complexes (sketched to the left of the ridge), or along transform faults (sketched to the right of the ridge), following a complex history of melt depletion (in red; forming gabbros, dark green, and MORB, black) and magmatic refertilization (indicated with orange dashed arrows) in a magma-starved environment. (b) In the trench to forearc region, serpentinisation may occur along bend faults, and hydration fluids are likely dominated by sediment-equilibrated pore waters (dark blue arrows). Such hydration drives serpentinisation that may have started in a MOR environment. In this figure, only bend faults are emphasized; other faulting and thrusting is omitted for simplicity. Plate interface melange zones start to develop, drawn with sharp red boundaries for emphasis; however, gradual transition towards plate interiors are reality as depicted in figure (c). (c) In trench to forearc settings, ultramafic rock fluid interactions are dominated by sedimentary pore fluids and shallow dehydration fluids. Note that stars with a dashed border in figure (b) represent materials that may have been hydrated previously in abyssal settings of figure (a). (c) Peak metamorphic conditions for the three units in the subduction zone. Almirez is located precisely on the antigorite dehydration reaction (orange dashed line). Erro Tobbio is located at greater depth than the brucite dehydration reaction (yellow dashed line) and colder temperatures than Almirez as testified by the presence of up to 30% olivine in Atg-serpentinites. Schematic peak metamorphic location of Franciscan or Schistes Lustrés melange rocks (if they were subducted to this depth range) is indicated by the brown star. The melange zone of the plate interface domain is represented by the yellow-green patterned material concentrating former ocean floor rocks including metabasalts and possibly hosting partially intact ocean floor rock lenses. Thick blue dashed lines represent major, focused fluid migration pathways, including major intraslab tectonic lineaments (such as the Lower Shear Zone at Monviso; e.g., Angiboust et al., 2011), and thin blue dashed lines represent intra-unit high deformation zones. Dehydration fluid escape is indicated by pink arrows, containing fluid-mobile elements lost from the prograde ultramafic rocks as listed to the right of the plot. The text box entitled “Recycling to the convecting mantle” contains elements interpreted here to be recycled to the deep mantle in dehydrated former oceanic serpentinites, potentially producing geochemical anomalies in deep mantle sources, including the HIMU reservoir (e.g., Kendrick et al., 2017; Pettke et al., 2018). Ingress of slab fluids into the mantle wedge and associated metasomatism is omitted for simplicity. In all figures, exhumation-related structures and processes are omitted for clarity, as are mantle wedge details. (For interpretation of the references to colour in this figure legend, the reader is referred to the web version of this article.)

rock-buffered serpentinisation takes place forming prominent modes of brucite along with modest CaO loss (the Erro Tobbio case; compare Peters et al., 2020). Consequently, Atg-serpentinities beyond the brucite dehydration reaction show metamorphic olivine modes of up to 30% (compare Table 1). Enrichments are still very prominent for B and W, along with modest enrichments in Sb, As, and the other chalcophile elements Tl, Bi, Cd, In, Sn, and Pb. These geochemical characteristics exemplified by Erro Tobbio serpentinites are similar to those reported for Zermatt-Saas serpentinites (Gilio et al., 2019). Alkali and alkaline earth elements may also get slightly enriched, however, these are typically much more enriched from sediment-equilibrated pore fluids as are expected to prevail in trench to forearc environments (e.g., Kodolányi et al., 2012; Peters et al., 2017; Zhang et al., 2019, and discussion above). Indeed, Erro Tobbio Atg-serpentine trace element enrichment signatures of U/Cs < 0.2 and Rb/Cs of between 1 and 8 are characteristic of trench to shallow forearc hydration; hence, we place Erro Tobbio in the trench to forearc region in our model (Fig. 11b), towards the hydration front associated with bend faults or with reactivated transform faults or normal faults generated upon rifting of the passive margin during Tethys opening. Serpentinisation of Erro Tobbio ultramafic rocks on the ocean floor near a MOR setting (Fig. 11a) is suggested by the presence of rodingites (Scambelluri et al., 1995); however, Scambelluri and Tonarini (2012) also proposed significant hydration in a hanging wall wedge setting based on B isotope data. Similarly, the elevated Cs and \pm Rb concentrations found for Almirez rocks can be interpreted to indicate a second stage of serpentinisation associated with sediment-equilibrated fluid: if present we would favour a sedimentary pore fluid signal acquired in a trench to shallow forearc environment (indicated in Fig. 11b).

Settings 1 and 2 thus encompass a continuous serpentinisation process that evolves with decreasing water/rock ratio towards increasingly ultramafic rock buffered conditions away from the seawater lithosphere interface. To the contrast, the hydration environment prevailing in sediment melanges hosting comparatively small peridotite lenses (setting 3) is prominently different. Such melanges can be assembled during deeper forearc to plate interface tectonic mixing involving preferably serpentinites previously exposed on the ocean floor (Fig. 11b; e.g., Cooperdock et al., 2018) or possibly already in ocean-floor tectonic breccias associated with normal faulting at magma-poor, hyper-extended rifted margins (e.g., Beltrando et al., 2014; Ribes et al., 2019) that likely become reactivated upon subduction. Such ocean-continent transition (OCT) zones were typical for the ancient European margin of the Tethys, but they are omitted in Fig. 11 for simplicity as they represent a variant to the ocean floor hydration scenarios documented above. An important difference between OCT and MOR hydration settings is the omnipresence of detrital sediments and associated sediment-equilibrated pore fluids in OCT settings, along with shallow dehydration fluids when diagenesis progresses. Serpentinisation in an OCT setting, in forearc melanges, or possibly deeper along the plate interface offers ample opportunity for prograde metasomatism forming hybrid rocks (compare e.g., Bebout, 2007; Lafay et al., 2013; Wakabayashi, 2017; Wu et al., 2021). However, we note that such fluid rock interaction primarily concentrates along the lens margins or intra-lens deformation zones and may not pervasively affect larger serpentinite bodies (compare Gilio et al., 2019, 2020; Locatelli et al., 2019; Peters et al., 2020). Together, we consider the mass of such serpentinite bodies enriched in sedimentary FME to be prominently subordinate to the total serpentinite mass subducted. This is further amplified by a probable exhumation bias, because slab-internal serpentinites are more likely to be dragged down to complete dehydration, upon which buoyancy is lost and the meta-peridotites are recycled to the mantle. We concur with Agard et al. (2018) who suggest that serpentinite bodies associated with the plate interface zone have the highest possibility to eventually return to the surface. This recovery or exhumation bias towards highly hybridised plate interface rock melange materials hosting serpentinites that often display spectacular FME enrichments along with high degrees of

oxidation (e.g., Hattori and Guillot, 2007; Scambelluri et al., 2014; Deschamps et al., 2013; Lafay et al., 2013) thus parallels the sampling bias towards FME enriched, strongly oxidised serpentinites retrieved from the ocean floors (notably via dredging; e.g., Niu, 2004); hence, serpentinites formed in fluid-dominated environments are distinctly overrepresented in our sample record. We therefore infer that a more mass-balanced inventory of serpentinite compositions is required to better assess the potential impact serpentinite subduction may have on the recycling of specific trace element enrichments to the convecting mantle or on the composition of arc magmas.

With progressive subduction, serpentinites undergo a series of mostly dehydration reactions (the most relevant ones depicted in Fig. 11), all of which contribute to the fact that bulk serpentinite remains water saturated throughout most of its prograde subduction history up to spinel or garnet peridotite, in Atg-serpentinities further sustained by continuous prograde antigorite recrystallisation towards lower antigorite H₂O contents (Shen et al., 2020). Unless these fluids get interconnected, forming high-permeability domains for example along deformation zones, bulk serpentinites can be expected to largely escape FME-bearing subduction fluid infiltration, notably also because fluid migration (hydraulic) gradients imposed by continuous dehydration are overall inside out. This implies that the rock masses simply “sweat” with progressive subduction. Specifically for Almirez, the textural Chl-harzburgite variants are interpreted to represent the products of (i) static dehydration along with fluid expulsion represented by spinifex-textured Chl-harzburgite, while (ii) granular Chl-harzburgite characterised by equilibrium textures trace dehydration fluid migration pathways. The dehydration fluid FME inventory remains poorly constrained to date, however, but combined mineral composition and relic fluid inclusion data indicate significant mobility for LILE, alkali and alkaline earth elements, B, Sr, halogens, As, \pm Sb, \pm Li, \pm Pb at the lizardite/chrysolite to antigorite+H₂O and at the antigorite to olivine+orthopyroxene+chlorite+magnetite+H₂O reactions (Fig. 11c). Chlorite remains the major hydrous mineral after antigorite decomposition, and our data demonstrate that such chlorite contains supra-PM concentrations of B, As, Sb, Bi, Cs, and some transition metals (Fig. 5b).

Serpentine subduction has been invoked to be central to fluid-mediated partial melting in the mantle wedge to eventually trigger calcalkaline magmatism (e.g., Tonarini et al., 2011; Spandler and Pirard, 2013). Subducting slab isotherms are such that hottest temperatures are at the slab surface while slab interiors are much colder (Syracuse et al., 2010; dehydration boundaries sketched in Fig. 11 mimic slab isotherms). Consequently, antigorite dehydration taking place at temperatures below \sim 680 °C (for Almirez e.g., Bretscher et al., 2018) likely occurs in deeper forearc regions shallower than \sim 120 km (Syracuse et al., 2010). Importantly, this also dehydrates antigorite in hanging wall wedge serpentinite dragged down along the plate interface by wedge corner flow once slab and wedge are coupled. Antigorite dehydration at subarc depths is thus likely confined to intra-slab serpentinite masses of old oceanic lithosphere where the cold finger extends to much greater depth (compare the slab Moho geotherms of Syracuse et al., 2010), possibly triggering intraslab seismicity via dehydration embrittlement (e.g., Peacock, 2001). An appealing alternative is chlorite dehydration at subarc depths, because chlorite dehydration occurs at temperatures that exceed antigorite dehydration by up to 100 °C along typical geotherms. Given our data presented here for chlorite that shows low overall FME concentrations, such a chlorite dehydration fluid may carry a dilute geochemical signal only and, consequently, it is difficult to positively identify such a geochemical chlorite signal. Irrespective of this, intraslab hydrous peridotites offer great potential to carry water down to subarc depth to eventually trigger arc magmatism.

For cases of efficient exhumation of some of the larger serpentinite bodies (compare Hermann et al., 2000; Guillot et al., 2015; Agard et al., 2018) these may return to the surface displaying texturally distinct, retrograde overprint only as opposed to complete retrogression of ultramafic lenses in plate interface melanges (Schwarzenbach et al.,

2018a). Retrogression features can be avoided when performing in-situ measurements to decipher the complex rock history of magmatic depletion and refertilization, serpentinisation, and prograde subduction metamorphism. Almirez and Erro Tobbio metaperidotites cover well the typical magmatic range of peridotite types that get serpentinised (variable melt depletion combined with variably prominent magmatic refertilization), and serpentinisation processes cover the range from fluid-buffered and oxidising to rock-buffered and reducing. We therefore conclude that Almirez + Erro Tobbio serpentinites best represent the geochemical and petrologic characteristics of the largest mass fraction of subducted serpentinites globally. We propose that their extensive, combined major to trace element data set now available may serve as a model geochemical composition of average subducted serpentinite, to be used in future modelling of subduction zone petrology and geochemical cycling.

7. Conclusions

We present a comprehensive bulk rock and in-situ mineral major to trace element data set for coexisting Atg-serpentinites and Chl-harzburgites from Almirez, Spain, and combine this with literature data to better constrain lithosphere-scale geochemical processes of magmatic peridotite conditioning, oceanic hydration and metasomatism (serpentinisation), and modifications upon subduction and exhumation. We introduce here the novel concept of hydration enrichment numbers to quantify the combined effects of element addition upon peridotite hydration and element loss upon partial dehydration on an individual sample basis rather than solely employing primitive mantle normalised trace element distribution diagrams. This way, the prominently variable incompatible element concentrations imposed by magmatic processes (prior to variable extents of hydration metasomatism) are taken as the sample-specific baseline, thus offering a much more accurate quantification of element enrichments and/or depletions via fluid-mediated processes.

Detailed analysis of the geochemical effects of magmatic refertilization following melt extraction reveals that incompatible and fluid-immobile element concentration variations exceed one order of magnitude in our sample set. As a consequence, fluid mobile, incompatible element concentrations are inferred to also have varied by over an order of magnitude prior to hydration. For example, the U budget in several Atg-serpentinite and Chl-harzburgite samples from Almirez can be fully accounted for by magmatic refertilization, while there is clear evidence for U addition upon hydration in other samples. We even find indications that the sum of magmatic preconditioning influenced the extent of metasomatism upon ocean floor serpentinisation.

Hydration enrichment numbers are highest for Sb and As (up to ~600), followed by B, W, Cs, Li, Pb, Bi, In, and U for our Almirez sample set. Combined evidence supports early FME addition to Almirez rocks, including chalcophile elements such as As and Sb, thus suggesting a dominant hydration metasomatism from seawater on the ocean floor. We argue using geochemical systematics that addition of a sedimentary fluid component upon serpentinisation is possible but not required to explain our FME data set. If present, we favour sediment-equilibrated pore fluids in a trench (to shallow forearc) setting rather than prograde metamorphic sediment dehydration fluids along the plate interface as the possible source. This is because FME enrichment-depletion patterns in minerals indicate that serpentinites acquired their variable FME enrichments prior to the antigorite crystallisation reaction. Strong enrichments in As and Sb of hydrous peridotites should therefore not be taken at face value to demonstrate involvement of metamorphic sediment dehydration fluids. Other chalcophile elements including Pb, In, Bi, Cd, Sn, Tl, and Zn show variations that are generated by both magmatic refertilization and peridotite hydration and partial dehydration; hence, addition upon hydration is not so prominent as for As and Sb.

Because hydration enrichment numbers are well above 1 for the

classical FME B, As, Sb, W, Cs, Li, and Pb even in Chl-harzburgite samples, hydration-related enrichment predominates over prograde metamorphic loss for these elements up to and including the Atg-dehydration reaction. To the contrast, prominent LILE fractions are lost from serpentinites during early subduction dehydration as the hydration enrichment numbers <1 for Rb and Ba reveal. To complicate things, hydration metasomatism upon retrogression may even dominate the trace element inventory of some FME including LILE, alkali elements, and Pb and Sr, thus casting doubt on inferences drawn from bulk rock Pb and Sr isotope systematics on the peak metamorphic conditions. In fact, retrograde FME enrichments as measured in serpentine formed after metamorphic olivine and talc after metamorphic orthopyroxene possess a sedimentary flavour for the Almirez Chl-harzburgites, again cautioning that bulk rock data may lead to an overestimation of the sedimentary source contribution.

FME enrichments also need to be present in metamorphic rock-forming minerals (and not only in bulk rock data sets) to ensure that these represent a true signal from hydration to prograde subduction, having just mentioned the danger of retrograde geochemical refertilisation. Therefore, in-situ measurements are required. Our comprehensive mineral data set reveals that antigorite is a relevant host for nearly all FME (including B, As, Sb, Li, W, Cs, Bi, and U) in Atg-serpentinite, and that FME enrichment patterns are similar for all metamorphic silicate minerals in this rock. Inclusion-rich olivine from Chl-harzburgite contains much higher FME concentrations than does inclusion-free Ol from the same samples, thus revealing that a prominent fraction of FME is liberated upon antigorite dehydration and partially retained in the rock in the form of fluid inclusion relics in prograde minerals. This reveals that FME enrichments upon peridotite hydration early in the rock's history were prominent and variable for the present sample set.

A striking finding based on our data is the very prominent geochemical variability produced during magmatic preconditioning, serpentinisation, and prograde metamorphic dehydration, on centimetre to metre to probably kilometre scales. This understanding readily disqualifies approaches that estimate geochemical changes or fluxes across a dehydration reaction based on comparison of different rock samples representing reactant and product mineralogy of a given dehydration reaction. Rather, intra-sample approaches are needed, as exemplified here by in-situ mineral data, by hydration enrichment numbers, or by single sample scale forward modelling on the fate of oxides upon antigorite dehydration (Vieira Duarte et al., 2021).

Considering the total mass of serpentinite subducted, the most relevant settings for hydration and metasomatism are oceanic, from MOR to trench (to shallow forearc), by seawater and sediment-equilibrated pore fluids; mineral lattice-bound metamorphic dehydration fluids are considered here to be much less relevant. We interpret the fact that many studies report on metamorphic sediment dehydration fluids to be responsible for massive FME enrichments in hydrous ultramafic rocks to result from a sampling bias that likely parallels a recovery bias of subducted hydrous peridotites. Subducted rocks are preferably exhumed along the subduction plate interface, thus bringing back a large share of hydrous ultramafic rocks from interface melanges with a history of multiple hydration-dehydration metasomatic events in presence of sediment that took place during progressive subduction and upon retrogression during exhumation. To the contrast, large bodies of hydrous slab peridotites may simply become insufficiently buoyant once they passed antigorite dehydration and are therefore lost to the convecting mantle. We therefore propose that the comprehensive geochemical data set available for serpentinites from Almirez and Erro Tobbio (Peters et al., 2020) represent the best estimate of the trace element inventory of the largest mass of globally subducted serpentinite. Almirez represents the case of complete serpentinisation near the ocean floor at high water-rock ratios, variably oxidised and with strong FME enrichments. Erro Tobbio Atg-serpentinites represent rocks formed near the hydration front at rock-buffered, moderately oxidising to reducing conditions and with modest FME enrichments. Their composite

serpentinite composition should therefore be used in future geochemical modelling to assess the impact of serpentinite subduction beyond the mere addition of H₂O on the overall geochemical cycle at convergent plate boundaries, including what can be recycled to the convecting mantle.

Funding

This work was supported by the Swiss National Science Foundation [grant numbers 200021_160076 and 200021_160688 to TP].

Data availability statement

All new data for Almirez presented in this study are provided in Appendix Tables A1 to A 18.

Declaration of Competing Interest

The authors declare that they have no known competing financial interests or personal relationships that could have appeared to influence the work reported in this paper.

Acknowledgments

We thank Carl Spandler and Janos Kodolanyi for great field work, and Maria Schönbächler for sharing her MSc work with us. We thank members of our thin section preparation lab for their excellent work and Daniel Peters and Joerg Hermann for very fruitful discussions. We also thank the Sierra Nevada National Park authorities for providing the permit for fieldwork and sampling in the Sierra Nevada National Park in 2006. We highly appreciate the thoughtful reviewer comments by E. Schwarzenbach, S. Guillot, and anonymous, which helped to clarify several aspects in this manuscript, and the efficient editorial handling by A. Gomez-Tuena.

Appendix A. Supplementary data

Supplementary data to this article can be found online at <https://doi.org/10.1016/j.earscirev.2021.103896>.

References

- Agard, P., Plunder, A., Angiboust, S., Bonnet, G., Ruh, J., 2018. The subduction plate interface: rock record and mechanical coupling (from long to short timescales). *Lithos* 320, 537–566.
- Agranian, A., Lee, C.A., Li, Z.A., Leeman, W.P., 2007. Fluid-mobile element budgets in serpentinized oceanic lithosphere mantle: insights from B, As, Li, Pb, PGEs and Os isotopes in the Feather River Ophiolite, California. *Chem. Geol.* 245, 230–241.
- Agrinier, P., Girardeau, J., 1988. Hydrothermal alteration of the peridotites cored at the ocean/continent boundary of the Iberian Margin: petrologic and stable isotope evidence. *Proc. Ocean Drill. Prog. Sci. Results* 103, 225–234.
- Albers, E., Kahl, W.A., Beyer, L., Bach, W., 2020. Variant across-forearc compositions of slab-fluids recorded by serpentinites: implications on the mobilization of FMEs from an active subduction zone (Mariana forearc). *Lithos* 364.
- Allen, D.E., Seyfried, W.E., 2005. REE controls in ultramafic hosted MOR hydrothermal systems: an experimental study at elevated temperature and pressure. *Geochim. Cosmochim. Acta* 69, 675–683.
- Alt, J.C., Shanks, W.C., 1998. Sulfur in serpentinized oceanic peridotites: Serpentinization processes and microbial sulfate reduction. *J. Geophys. Res. Solid Earth* 103, 9917–9929.
- Alt, J.C., Garrido, C.J., Shanks III, W.C., Turchyn, A., Padrón-Navarta, J.A., López Sánchez-Vizcaíno, V., Gómez-Pugnaire, M.T., Marchesi, C., 2012. Recycling of water, carbon, and sulfur during subduction of serpentinites: a stable isotope study of Cerro del Almirez, Spain. *Earth Planet. Sci. Lett.* 327–328, 50–60.
- Alt, J.C., Schwarzenbach, E.M., Frueh-Green, G.L., Shanks, W.C., Bernasconi, S.M., Garrido, C.J., Crispini, L., Gaggero, L., Padron-Navarta, J.A., Marchesi, C., 2013. The role of serpentinites in cycling of carbon and sulfur: seafloor serpentinization and subduction metamorphism. *Lithos* 178, 40–54.
- Andreani, M., Munoz, M., Marcaillou, C., Delacour, A., 2013. Mu XANES study of iron redox state in serpentine during oceanic serpentinization. *Lithos* 178, 70–83.
- Andreani, M., Escartin, J., Delacour, A., Ildefonso, B., Godard, M., Dymant, J., Fallick, A. E., Fouquet, Y., 2014. Tectonic structure, lithology, and hydrothermal signature of the Rainbow massif (Mid-Atlantic Ridge 36 degrees 14' N). *Geochem. Geophys. Geosyst.* 15, 3543–3571.
- Angiboust, S., Agard, P., Raimbourg, H., Yamato, P., Huet, B., 2011. Subduction interface processes recorded by eclogite-facies shear zones (Monviso, W. Alps). *Lithos* 127, 222–238.
- Babechuk, M.G., Kamber, B.S., Greig, A., Canil, D., Kodolányi, J., 2010. The behaviour of tungsten during mantle melting revisited with implications for planetary differentiation time scales. *Geochim. Cosmochim. Acta* 74, 1448–1470.
- Banner, J.L., 1995. Application of the trace-element and isotope geochemistry of strontium to studies of carbonate diagenesis. *Sedimentology* 42, 805–824.
- Barnes, J.D., Beltrando, M., Lee, C.-T.A., Cisneros, M., Loewy, S., Chin, E., 2014. Geochemistry of Alpine serpentinites from rifting to subduction: a view across paleogeographic domains and metamorphic grade. *Chem. Geol.* 389, 29–47.
- Bebout, G.E., 2007. Metamorphic chemical geodynamics of subduction zones. *Earth Planet. Sci. Lett.* 260, 373–393.
- Beltrando, M., Manatschal, G., Mohn, G., Dal Piaz, G.V., Brovarone, A.V., Masini, E., 2014. Recognizing remnants of magma-poor rifted margins in high-pressure orogenic belts: the Alpine case study. *Earth Sci. Rev.* 131, 88–115.
- Bodinier, J.L., Godard, M., 2014. Orogenic, ophiolitic, and abyssal peridotites. In: Carlson, R.W. (Ed.), *Mantle and Core: Treatise on Geochemistry*, 2, pp. 103–167.
- Bonatti, E., Lawrence, J.R., Morandi, N., 1984. Serpentinization of oceanic peridotites: temperature dependence of mineralogy and boron content. *Earth Planet. Sci. Lett.* 70, 88–94.
- Boschi, C., Dini, A., Fruh-Green, G.L., Kelley, D.S., 2008. Isotopic and element exchange during serpentinization and metasomatism at the Atlantis Massif (MAR 30 degrees N): insights from B and Sr isotope data. *Geochim. Cosmochim. Acta* 72, 1801–1823.
- Boschi, C., Bonatti, E., Ligi, M., Brunelli, D., Cipriani, A., Dallai, L., D'Orazio, M., Fruh-Green, G.L., Tonarini, S., Barnes, J.D., Bedini, R.M., 2013. Serpentinization of mantle peridotites along an uplifted lithospheric section, Mid Atlantic Ridge at 11 degrees N. *Lithos* 178, 3–23.
- Bretscher, A., Hermann, J., Pettke, T., 2018. The influence of oceanic oxidation on serpentinite dehydration during subduction. *Earth Planet. Sci. Lett.* 499, 173–184.
- Brown, K.M., Saffer, D.M., Bekins, B.A., 2001. Smectite diagenesis, pore-water freshening, and fluid flow at the toe of the Nankai wedge. *Earth Planet. Sci. Lett.* 194, 97–109.
- Cannat, M., 1993. Emplacement Of Mantle Rocks In The Sea-Floor At Midocean Ridges. *Journal Of Geophysical Research-Solid Earth* 98, 4163–4172.
- Cannao, E., Agostini, S., Scambelluri, M., Tonarini, S., Godard, M., 2015. B, Sr and Pb isotope geochemistry of high-pressure Alpine metaperidotites monitors fluid-mediated element recycling during serpentinite dehydration in subduction melange (Cima di Gagnone, Swiss Central Alps). *Geochim. Cosmochim. Acta* 163, 80–100.
- Cannao, E., Scambelluri, M., Agostini, S., Tonarini, S., Godard, M., 2016. Linking serpentinite geochemistry with tectonic evolution at the subduction plate-interface: the Voltri Massif case study (Ligurian Western Alps, Italy). *Geochim. Cosmochim. Acta* 190, 115–133.
- Cluzel, D., Boulvais, P., Iseppi, M., Lahondere, D., Lesimple, S., Maurizot, P., Paquette, J. L., Tarantola, A., Ulrich, M., 2020. Slab-derived origin of tremolite-antigorite veins in a supra-subduction ophiolite: the Peridotite Nappe (New Caledonia) as a case study. *Int. J. Earth Sci.* 109, 171–196.
- Coleman, R.G., Keith, T.E., 1971. A chemical study of serpentinization, Burro Mountain, California. *J. Petrol.* 12, 311–328.
- Cooperdock, E.H.G., Raia, N.H., Barnes, J.D., Stockli, D.F., Schwarzenbach, E.M., 2018. Tectonic origin of serpentinites on Syros, Greece: geochemical signatures of abyssal origin preserved in a HP/LT subduction complex. *Lithos* 296, 352–364.
- Debret, B., Andreani, M., Godard, M., Nicollet, C., Schwartz, S., Lafay, R., 2013. Trace element behavior during serpentinization/de-serpentinization of an eclogitized oceanic lithosphere: a LA-ICP-MS study of the Lanzo ultrabasic massif (Western Alps). *Chem. Geol.* 357, 117–133.
- Debret, B., Koga, K.T., Nicollet, C., Andreani, M., Schwartz, S., 2014. F, Cl and S input via serpentinite in subduction zones: implications for the nature of the fluid released at depth. *Terra Nova* 26, 96–101.
- Debret, B., Albers, E., Walter, B., Price, R., Barnes, J.D., Beunon, H., Faq, S., Gillikin, D. P., Mattielli, N., Williams, H., 2019. Shallow forearc mantle dynamics and geochemistry: new insights from IODP Expedition 366. *Lithos* 326, 230–245.
- Debret, B., Garrido, C.J., Pons, M.L., Bouilhol, P., Inglis, E., Sanchez-Vizcaíno, V.L., Williams, H., 2021. Iron and zinc stable isotope evidence for open-system high-pressure dehydration of antigorite serpentinite in subduction zones. *Geochim. Cosmochim. Acta* 296, 210–225.
- Deschamps, F., Guillot, S., Godard, M., Chauvel, C., Andreani, M., Hattori, K.H., 2010. In situ characterization and behaviour of fluid-mobile elements in subduction zones. *Chem. Geol.* 269, 262–277.
- Deschamps, F., Guillot, S., Godard, M., Andreani, M., Hattori, K.H., 2011. Serpentinites act as sponges for fluid-mobile elements in abyssal and subduction zone environments. *Terra Nova* 23, 171–178.
- Deschamps, F., Godard, M., Guillot, S., Chauvel, C., Andreani, M., Hattori, K.H., Wunder, B., France, L., 2012. Behaviour of fluid mobile elements in serpentinites from abyssal to subduction environments: examples from Cuba and Dominican Republic. *Chem. Geol.* 312–313, 93–117.
- Deschamps, F., Godard, M., Guillot, S., Hattori, K.H., 2013. Geochemistry of subduction zone serpentinites: a review. *Lithos* 178, 96–127.
- Downes, H., 2001. Formation and modification of the shallow sub-continental lithospheric mantle: a review of geochemical evidence from ultramafic xenolith suites and tectonically emplaced ultramafic massifs of western and central Europe. *J. Petrol.* 42, 233–250.

- Elliott, T., Zindler, A., Bourdon, B., 1999. Exploring the kappa conundrum: the role of recycling in the lead isotope evolution of the mantle. *Earth Planet. Sci. Lett.* 169, 129–145.
- Evans, B.W., 2004. The serpentinite multisystem revisited: chrysotile is metastable. *Int. Geol. Rev.* 46, 479–506.
- Evans, K.A., 2012. The redox budget of subduction zones. *Earth Sci. Rev.* 113, 11–32.
- Früh-Green, G.L., Connolly, J.A.D., Plasz, A., Kelley, D.S., Grobety, B., 2004. Serpentinisation of oceanic peridotites: implications for geochemical cycles and biological activity. *Geophys. Monogr. Ser.* 144, 119–136.
- Fryer, P., 2012. Serpentine mud volcanism: observations, processes, and implications. In: Carlson, C.A., Giovannoni, S.J. (Eds.), *Annual Review of Marine Science*, Vol 4, p. 345.
- Früh-Green, G.L., Orcutt, B.N., Roumejon, S., Lilley, M.D., Morono, Y., Cotterill, C., Green, S., Escartin, J., John, B.E., McCaig, A.M., Cannat, M., Menez, B., Schwarzenbach, E.M., Williams, M.J., Morgan, S., Lang, S.Q., Schrenk, M.O., Brazelton, W.J., Akizawa, N., Boschi, C., Dunkel, K.G., Quemeneur, M., Whattam, S.A., Mayhew, L., Harris, M., Bayraktir, G., Behrmann, J.H., Herrero-Bervera, E., Hesse, K., Liu, H.Q., Ratnayake, A.S., Twing, K., Weis, D., Zhao, R., Bilinker, L., 2018. Magmatism, serpentinization and life: Insights through drilling the Atlantis Massif (IODP Expedition 357). *Lithos* 323, 137–155.
- Garbe-Schönberg, D., Müller, S., 2014. Nano-particulate pressed powder tablets for LA-ICP-MS. *J. Anal. At. Spectrom.* 29, 990–1000.
- Garrido, C.J., López Sánchez-Vizcaíno, V., Gómez-Pugnaire, M.T., Trommsdorff, V., Alard, O., Bodinier, J.-L., Godard, M., 2005. Enrichment of HFSE in chlorite harzburgite produced by high-pressure dehydration of antigorite-serpentinite: implications for subduction magmatism. *Geochem. Geophys. Geosyst.* 6 <https://doi.org/10.1029/2004GC000791>.
- GeoRem (Geological and Environmental Reference Materials), V18, 2021. <http://georem.mpch-mainz.gwdg.de>.
- GERM data base: Geochemical Earth Reference Model, 2021. www.EarthRef.org.
- Gilio, M., Scambelluri, M., Agostini, S., Godard, M., Peters, D., Pettke, T., 2019. Petrology and geochemistry of serpentinites associated with the ultra-high pressure Lago di Cignana Unit (Italian Western Alps). *J. Petrol.* 60, 1229–1262.
- Gilio, M., Scambelluri, M., Agostini, S., Godard, M., Pettke, T., Agard, P., Locatelli, M., Angiboust, S., 2020. Fingerprinting and relocating tectonic slices along the plate interface: evidence from the Lago Superiore unit at Monviso (Western Alps). *Lithos* 252/253, 105308.
- Godard, M., Jousset, D., Bodinier, J.-L., 2000. Relationships between geochemistry and structure beneath a palaeo-spreading centre: a study of the mantle section in the Oman Ophiolite. *Earth Planet. Sci. Lett.* 180, 133–148.
- Guillong, M., Meier, D.L., Allan, M.M., Heinrich, C.A., Yardley, B.W.D., 2008. SILLS: A MATLAB-based program for the reduction of laser ablation ICP-MS data of homogeneous materials and inclusions. In: Sylvester, P. (Ed.), *Laser Ablation ICP-MS in the Earth Sciences: Current Practices and Outstanding Issues*, Mineralogical Association of Canada, Short Course Series, vol. 40, pp. 328–333.
- Guillot, S., Schwartz, S., Reynard, B., Agard, P., Prigent, C., 2015. Tectonic significance of serpentinites. *Tectonophysics* 646, 1–19.
- Harvey, J., Garrido, C.J., Savov, I., Agostini, S., Padrón-Navarta, J.A., Marchesi, C., Sanchez-Vizcaíno, V.L., Gomez-Pugnaire, M.T., 2014. B-11-rich fluids in subduction zones: the role of antigorite dehydration in subducting slabs and boron isotope heterogeneity in the mantle. *Chem. Geol.* 376, 20–30.
- Hattori, K.H., Guillot, S., 2003. Volcanic fronts form as a consequence of serpentinite dehydration in the forearc mantle wedge. *Geology* 31, 525–528.
- Hattori, K.H., Guillot, S., 2007. Geochemical character of serpentinites associated with high- to ultrahigh-pressure metamorphic rocks in the Alps, Cuba, and the Himalayas: recycling of elements in subduction zones. *Geochem. Geophys. Geosyst.* 8 <https://doi.org/10.1029/2007GC001594>.
- Hermann, J., Muntener, O., Scambelluri, M., 2000. The importance of serpentinite mylonites for subduction and exhumation of oceanic crust. *Tectonophysics* 327, 225–238.
- Hulme, S.M., Wheat, C.G., Fryer, P., Mottl, M.J., 2010. Pore water chemistry of the Mariana serpentinite mud volcanoes: a window to the seismogenic zone. *Geochem. Geophys. Geosyst.* 11.
- Hüpers, A., Kopf, A.J., 2012. Effect of smectite dehydration on pore water geochemistry in the shallow subduction zone: an experimental approach. *Geochem. Geophys. Geosyst.* 13.
- Hyndman, R.D., Peacock, S.M., 2003. Serpentinization of the forearc mantle. *Earth Planet. Sci. Lett.* 212, 417–432.
- Jagoutz, E., Palme, H., Baddenhausen, H., Blum, K., Cendales, M., Dreibus, G., Spettel, B., Lorenz, V., Wänke, H., 1979. The abundances of major, minor and trace elements in the earth's mantle as derived from primitive ultramafic nodules. *Proc. Lunar Planet. Sci. Conf.* 10th, 2031–2050.
- Jenner, F.E., O'Neill, H.S., 2012. Analysis of 60 elements in 616 ocean floor basaltic glasses. *Geochem. Geophys. Geosyst.* 13.
- Jochum, K.P., Verma, S.P., 1996. Extreme enrichment of Sb, Tl and other trace elements in altered MORB. *Chem. Geol.* 130, 289–299.
- John, T., Scambelluri, M., Friche, M., Barnes, J.D., Bach, W., 2011. Dehydration of subducting serpentinite: Implications for halogen mobility in subduction zones and the deep halogen cycle. *Earth Planet. Sci. Lett.* 308, 65–76.
- Jöns, N., Bach, W., Klein, F., 2010. Magmatic influence on reaction paths and element transport during serpentinization. *Chem. Geol.* 274, 196–211.
- Kahl, W.A., Jöns, N., Bach, W., Klein, F., Alt, J.C., 2015. Ultramafic clasts from the South Chamorro serpentinite mud volcano reveal a polyphase serpentinization history of the Mariana forearc mantle. *Lithos* 227, 1–20.
- Kastner, M., Solomon, E.A., Harris, R.N., Torres, M.E., 2014. Fluid origins, thermal regimes, and fluid and solute fluxes in the forearc of subduction zones. In: Stein, R., Blackman, D.K., Inagaki, F., Larsen, H.-C. (Eds.), *Earth and Life Processes Discovered from Subseafloor Environments: A Decade of Science Achieved by the Integrated Ocean Drilling Program (IODP)*. Elsevier, Amsterdam, pp. 671–733.
- Kempf, E.D., Hermann, J., Reusser, E., Baumgartner, L.P., Lanari, P., 2020. The role of the antigorite plus brucite to olivine reaction in subducted serpentinites (Zermatt, Switzerland). *Swiss J. Geosci.* 113.
- Kendrick, M.A., Scambelluri, M., Honda, M., Phillips, D., 2011. High abundance of noble gas and chlorine delivered to the mantle by serpentinite subduction. *Nat. Geosci.* 4, 807–812.
- Kendrick, M.A., Honda, M., Pettke, T., Scambelluri, M., Phillips, D., Giuliani, A., 2013. Subduction zone fluxes of halogens and noble gases in seafloor and forearc serpentinites. *Earth Planet. Sci. Lett.* 365, 86–96.
- Kendrick, M.A., Hemon, C., Kamenetsky, V.S., Danyushevsky, L., Devey, C.W., Rodemann, T., Jackson, M.G., Perfit, M.R., 2017. Seawater cycled throughout Earth's mantle in partially serpentinized lithosphere. *Nat. Geosci.* 10, 222–U97.
- Kendrick, M.A., Scambelluri, M., Hermann, J., Padrón-Navarta, J.A., 2018. Halogens and noble gases in serpentinites and secondary peridotites: implications for seawater subduction and the origin of mantle neon. *Geochim. Cosmochim. Acta* 235, 285–304.
- Klein, F., Bach, W., Humphris, S.E., Kahl, W.A., Jöns, N., Moskowitz, B., Berquo, T.S., 2014. Magnetite in seafloor serpentinite-some like it hot. *Geology* 42, 135–138.
- Klein, F., Marschall, H.R., Bowling, S.A., Humphris, S.E., Horning, G., 2017. Mid-ocean ridge serpentinite in the Puerto Rico Trench: from seafloor spreading to subduction. *J. Petrol.* 58, 1729–1753.
- Kodolányi, J., Pettke, T., 2011. Loss of trace elements from serpentinites during fluid-assisted transformation of chrysotile to antigorite – an example from Guatemala. *Chem. Geol.* 284, 351–362.
- Kodolányi, J., Pettke, T., Spandler, C., Kamber, B.S., Gmeling, K., 2012. Geochemistry of ocean floor and fore-arc serpentinites: constraints on the ultrabasic input to subduction zones. *J. Petrol.* 53, 235–270.
- Kominz, M.A., Patterson, K., Odette, D., 2011. Lithology dependence of porosity in slope and deep marine sediments. *J. Sediment. Res.* 81, 730–742.
- Lafay, R., Deschamps, F., Schwartz, S., Guillot, S., Godard, M., Debret, B., Nicollet, C., 2013. High-pressure serpentinites, a trap-and-release system controlled by metamorphic conditions: example from the Piedmont zone of the western Alps. *Chem. Geol.* 343, 38–54.
- Locatelli, M., Verlaquet, A., Agard, P., Pettke, T., Federico, L., 2019. Fluid pulses during stepwise brecciation at intermediate subduction depths (Monviso Eclogites, W. Alps): first internally then externally sourced. *Geochem. Geophys. Geosyst.* 20, 5285–5318.
- López Sánchez-Vizcaíno, V., Rubatto, D., Gómez-Pugnaire, M.T., Trommsdorff, V., Müntener, O., 2001. Middle Miocene high-pressure metamorphism and fast exhumation of the Nevado-Filábride Complex, SE Spain. *Terra Nova* 13, 327–332.
- López Sánchez-Vizcaíno, V., Trommsdorff, V., Gómez-Pugnaire, M.T., Garrido, C.J., Müntener, O., Connolly, J.A.D., 2005. Petrology of titanite clinohumite and olivine at the high-pressure breakdown of antigorite serpentinite to chlorite harzburgite (Almirez Massif, S Spain). *Contrib. Mineral. Petrol.* 149, 627–646.
- Malvoisin, B., 2015. Mass transfer in the oceanic lithosphere: serpentinization is not isochemical. *Earth Planet. Sci. Lett.* 430, 75–85.
- Marchesi, C., Garrido, C.J., Padrón-Navarta, J.A., López Sánchez-Vizcaíno, V., Gómez-Pugnaire, M.T., 2013. Element mobility from seafloor serpentinization to high-pressure dehydration of antigorite in subducted serpentinite: insight from the Cerro del Almirez ultrabasic massif (southern Spain). *Lithos* 178, 128–142.
- McDonough, W.F., Sun, S.S., 1995. The composition of the Earth. *Chem. Geol.* 120, 223–253.
- Menzel, M.D., Garrido, C.J., Sanchez-Vizcaíno, V.L., Hidas, K., Marchesi, C., 2019. Subduction metamorphism of serpentinite-hosted carbonates beyond antigorite-serpentinite dehydration (Nevado-Filábride Complex, Spain). *J. Metamorph. Geol.* 37, 681–715.
- Mottl, M.J., Wheat, C.G., Fryer, P., Gharib, J., Martin, J.B., 2004. Chemistry of springs across the Mariana forearc shows progressive devolatilization of the subducting plate. *Geochim. Cosmochim. Acta* 68, 4915–4933.
- Müntener, O., Pettke, T., Desmurs, L., Meier, M., Schaltegger, U., 2004. Refertilization of mantle peridotite in embryonic ocean basins: trace element and Nd isotopic evidence and implications for crust-mantle relationships. *Earth Planet. Sci. Lett.* 221, 293–308.
- Müntener, O., Manatschal, G., Desmurs, L., Pettke, T., 2010. Plagioclase peridotites in ocean-continent transitions: refertilized mantle domains generated by melt stagnation in the shallow mantle lithosphere. *J. Petrol.* 51, 255–294.
- Navon, O., Stolper, E., 1987. Geochemical consequences of melt percolation - the upper mantle as a chromatographic column. *J. Geol.* 95, 285–307.
- Niu, Y., 2004. Bulk-rock major and trace element compositions of abyssal peridotites: implications for mantle melting, melt extraction and post-melting processes beneath mid-ocean ridges. *J. Petrol.* 45, 2423–2458.
- Niu, Y., Langmuir, C.H., Kinzler, R.J., 1997. The origin of abyssal peridotites: a new perspective. *Earth Planet. Sci. Lett.* 152, 251–265.
- Noll Jr., P.D., Newsom, H.E., Leeman, W.P., Ryan, J.G., 1996. The role of hydrothermal fluids in the production of subduction zone magmas: evidence from siderophile and chalcophile trace elements and boron. *Geochim. Cosmochim. Acta* 60, 587–611.
- Padrón-Navarta, J.A., Hermann, J., Garrido, C.J., López Sánchez-Vizcaíno, V., Gómez-Pugnaire, M.T., 2010. An experimental investigation of antigorite dehydration in natural silica-enriched serpentinite. *Contrib. Mineral. Petrol.* 159, 25–42.
- Padrón-Navarta, J.A., López Sánchez-Vizcaíno, V., Garrido, C.J., Gómez-Pugnaire, M.T., 2011. Metamorphic record of high-pressure dehydration of antigorite serpentinite to chlorite harzburgite in a subduction setting (Cerro del Almirez, Nevado-Filábride Complex, Southern Spain). *J. Petrol.* 52, 2047–2078.

- Palme, H., O'Neill, H. St.C., 2014. Cosmochemical estimates of mantle composition. In: *Treatise on Geochemistry*, second edition, 3, chapter 3.1, pp. 1–39.
- Parsons, B., 1982. Causes and consequences of the relation between area and age of the ocean-floor. *J. Geophys. Res.* 87, 289–302.
- Paulick, H., Bach, W., Godard, M., De Hoog, J.C.M., Suhr, G., Harvey, J., 2006. Geochemistry of abyssal peridotites (Mid-Atlantic Ridge, 15 degrees 20' N, ODP Leg 209): implications for fluid/rock interaction in slow spreading environments. *Chem. Geol.* 234, 179–210.
- Peacock, S.M., 2001. Are the lower planes of double seismic zones caused by serpentine dehydration in subducting oceanic mantle? *Geology* 29, 299–302.
- Peters, D., Pettke, T., 2017. Evaluation of major to ultra trace element bulk rock chemical analysis of nanoparticle pressed powder pellets by LA-ICP-MS. *Geostand. Geoanal. Res.* <https://doi.org/10.1111/ggr.12125>.
- Peters, D., Bretscher, A., John, T., Scambelluri, M., Pettke, T., 2017. Fluid-mobile elements in serpentinites: constraints on serpentinisation environments and element cycling in subduction zones. *Chem. Geol.* 466, 654–666.
- Peters, D., Pettke, T., John, T., Scambelluri, M., 2020. The role of brucite in water and element cycling during subduction - an underestimated one? *Lithos* 360–361, 105431.
- Pettke, T., Oberli, F., Audéat, A., Guillong, M., Simon, A.C., Hanley, J.J., Klemm, L.M., 2012. Recent developments in element concentration and isotope ratio analysis of individual fluid inclusions by laser ablation single and multiple collector ICP-MS. *Ore Geol. Rev.* 44, 10–38.
- Pettke, T., Kodolanyi, J., Kamber, B.S., 2018. From ocean to mantle: new evidence for U-cycling with implications for the HIMU source and the secular Pb isotope evolution of Earth's mantle. *Lithos* 316, 66–76.
- Plank, T., Langmuir, C.H., 1998. The chemical composition of subducting sediment and its consequences for the crust and mantle. *Chem. Geol.* 145, 325–394.
- Puga, E., Nieto, J.M., Díaz de Federico, A., Bodinier, J.L., Morten, L., 1999. Petrology and metamorphic evolution of ultrabasic rocks and dolerite dykes of the Betic Ophiolitic Association (Mulhacén Complex, SE Spain): evidence of eo-Alpine subduction following an ocean-floor metasomatic process. *Lithos* 49, 23–56.
- Ranero, C., Morgan, J.P., McIntosh, K., Reichert, C., 2003. Bending-related faulting and mantle serpentinization at the Middle America trench. *Nature* 425, 367–373.
- Ribes, C., Ghienne, J.F., Manatschal, G., Decarlis, A., Karner, G.D., Figueredo, P.H., Johnson, C.A., 2019. Long-lived mega fault-scarps and related breccias at distal rifted margins: insights from present-day and fossil analogues. *J. Geol. Soc.* 176, 801–816.
- Ruiz Cruz, M.D., Puga, E., Nieto, J.M., 1999. Silicate and oxide exsolution in pseudo-spinifex olivine from metultramafic rocks of the Betic Ophiolite Association: a TEM study. *Am. Mineral.* 84, 1915–1924.
- Rüpke, L.H., Morgan, J.P., Hort, M., Connolly, J.A.D., 2004. Serpentine and the subduction zone water cycle. *Earth Planet. Sci. Lett.* 223, 17–34.
- Salters, V.J.M., Stracke, A., 2004. Composition of the depleted mantle. *Geochem. Geophys. Geosyst.* 5.
- Savov, I.P., Guggino, S., Ryan, J.G., Fryer, P., Mottl, M.J., 2005. Geochemistry of serpentinite muds and metamorphic rocks from the Mariana Forearc, ODP Sites 1200 and 778–779, South Chamorro and Conical Seamounts. *Proc. Ocean Drill. Program Sci. Results* 195, 1–49.
- Savov, I.P., Ryan, J.G., D'Antonio, M., Fryer, P., 2007. Shallow slab fluid release across and along the Mariana arc-basin system: insights from geochemistry of serpentinitized peridotites from the Mariana fore arc. *J. Geophys. Res.* 112 (B9), 1–30.
- Scambelluri, M., Philippot, P., 2001. Deep fluids in subduction zones. *Lithos* 55, 213–227.
- Scambelluri, M., Tonarini, S., 2012. Boron isotope evidence for shallow fluid transfer across subduction zones by serpentinitized mantle. *Geology* 40, 907–910.
- Scambelluri, M., Müntener, O., Hermann, J., Piccardo, G.B., Trommsdorff, V., 1995. Subduction of water into the mantle - history of an Alpine Peridotite. *Geology* 23, 459–462.
- Scambelluri, M., Bottazzi, P., Trommsdorff, V., Vannucci, R., Hermann, J., Gómez-Pugnaire, M.T., López Sánchez-Vizcaíno, V., 2001. Incompatible element-rich fluids released by antigorite breakdown in deeply subducted mantle. *Earth Planet. Sci. Lett.* 192, 457–470.
- Scambelluri, M., Müntener, O., Ottoloni, L., Pettke, T., Vannucci, R., 2004a. The fate of B, Cl and Li in the subducted oceanic mantle and in the antigorite breakdown fluids. *Earth Planet. Sci. Lett.* 222, 217–234.
- Scambelluri, M., Fiebig, J., Malaspina, N., Müntener, O., Pettke, T., 2004b. Serpentinized subduction: implications for fluid processes and trace-element recycling. *Int. Geol. Rev.* 46, 595–613.
- Scambelluri, M., van Roermund, H.L.M., Pettke, T., 2010. Mantle wedge peridotites: Fossil reservoirs of deep subduction zone processes inferences from high and ultrahigh-pressure rocks from Bardane (Western Norway) and Ulten (Italian Alps). *Lithos* 120, 186–201.
- Scambelluri, M., Pettke, T., Rampone, E., Godard, M., Reusser, E., 2014. Petrology and trace element budgets of high-pressure peridotites indicate subduction dehydration of serpentinitized mantle (Cima di Gagnone, Central Alps, Switzerland). *J. Petrol.* 55, 459–498.
- Scambelluri, M., Pettke, T., Cannao, E., 2015. Fluid-related inclusions in Alpine high-pressure peridotite reveal trace element recycling during subduction-zone dehydration of serpentinitized mantle (Cima di Gagnone, Swiss Alps). *Earth Planet. Sci. Lett.* 429, 45–59.
- Scambelluri, M., Cannao, E., Gilio, M., 2019. The water and fluid-mobile element cycles during serpentinite subduction. *A review*. *Eur. J. Mineral.* 31, 405–428.
- Schönbacher, M., 1999. Die Hochdruckmetamorphose der Ultramafika und der angrenzenden Nebengesteine am Cerro del Almirez, Sierra Nevada, Südsanien (Teil 1). Diplomarbeit der Abteilung CX (Erdwissenschaften) der Eidgenössischen Technischen Hochschule (unpublished).
- Schwartz, S., Guillot, S., Reynard, B., Lafay, R., Debret, B., Nicollet, C., Lanari, P., Auzende, A.L., 2013. Pressure-temperature estimates of the lizardite/antigorite transition in high pressure serpentinites. *Lithos* 178, 197–210.
- Schwarzenbach, E.M., Caddick, M.J., Petroff, M., Gill, B.C., Cooperdock, E.H.G., Barnes, J.D., 2018a. Sulphur and carbon cycling in the subduction zone melange. *Sci. Rep.* 8.
- Schwarzenbach, E.M., Gill, B.C., Johnston, D.T., 2018b. Unraveling multiple phases of sulfur cycling during the alteration of ancient ultramafic oceanic lithosphere. *Geochim. Cosmochim. Acta* 223, 279–299.
- Schwarzenbach, E.M., Vogel, M., Fruh-Green, G.L., Boschi, C., 2021. Serpentinization, carbonation, and metasomatism of ultramafic sequences in the Northern Apennine Ophiolite (NW Italy). *J. Geophys. Res.* 126.
- Shen, T.T., Zhang, C., Chen, J., Hermann, J., Zhang, L.F., Padron-Navarta, J.A., Chen, L., Xu, J., Yang, J.S., 2020. Changes in the cell parameters of antigorite close to its dehydration reaction at subduction zone conditions. *Am. Mineral.* 105, 569–582.
- Snow, J.E., Dick, H.J.B., 1995. Pervasive magnesium loss by marine weathering of peridotite. *Geochim. Cosmochim. Acta* 59, 4219–4235.
- Spandler, C., Pirard, C., 2013. Element recycling from subducting slabs to arc crust: a review. *Lithos* 170, 208–223.
- Spandler, C., Pettke, T., Hermann, J., 2014. Experimental study of trace element release during ultrahigh-pressure serpentinite dehydration. *Earth Planet. Sci. Lett.* 391, 296–306.
- Stevens, D.E., Henstock, T.J., McNeill, L.C., 2021. Evolution of the thermal and dehydration state of sediments entering the North Sumatra Subduction Zone. *Geochem. Geophys. Geosyst.* 22, 4.
- Su, W., Schwarzenbach, E.M., Chen, L., Li, Y., John, T., Gao, J., Liu, X., Chen, F., 2019. Sulfur isotope compositions of pyrite from high-pressure metamorphic rocks and related veins (SW Tianshan, China): implications for the sulfur cycle in subduction zones. *Lithos* 348–349, 105212.
- Syracuse, E.M., van Keken, P.E., Abers, G.A., 2010. The global range of subduction zone thermal models. *Phys. Earth Planet. Inter.* 183, 73–90.
- Tenthorey, E., Hermann, J., 2004. Composition of fluids during serpentinite breakdown in subduction zones: evidence for limited boron mobility. *Geology* 32, 865–868.
- Thompson, G., Melson, W.G., 1970. Boron contents in serpentinites and metabasalts in the oceanic crust: implications for the boron cycle in the oceans. *Earth Planet. Sci. Lett.* 8, 61–65.
- Tonarini, S., Leeman, W.P., Leat, P.T., 2011. Subduction erosion of forearc mantle wedge implicated in the genesis of the South Sandwich Island (SSI) arc: evidence from boron isotope systematics. *Earth Planet. Sci. Lett.* 301, 275–284.
- Tremosa, J., Gailhanou, H., Chiaberge, C., Castilla, R., Gaucher, E.C., Gout, C., Fialpis, C., Claret, F., 2020. Effects of smectite dehydration and illitisation on overpressures in sedimentary basins: a coupled chemical and thermo-hydro-mechanical modelling approach. *Mar. Pet. Geol.* 111, 166–178.
- Trommsdorff, V., Evans, B.W., 1974. Alpine metamorphism of peridotitic rocks. In: *Schweizerische Mineralogische und Petrologische Mitteilungen*, 54, pp. 333–352.
- Trommsdorff, V., Evans, B.W., 1980. Titanian hydroxyl-clinohumite: formation and breakdown in antigoritic rocks (Malenco, Italy). *Contrib. Mineral. Petrol.* 72, 229–242.
- Trommsdorff, V., López Sánchez-Vizcaíno, V., Gómez-Pugnaire, M.T., Müntener, O., 1998. High pressure breakdown of antigorite to spinifex-textured olivine and orthopyroxene, SE Spain. *Contrib. Mineral. Petrol.* 132, 139–148.
- Ulmer, P., Trommsdorff, V., 1995. Serpentine stability to mantle depths and subduction-related magmatism. *Science* 268, 858–861.
- Vieira Duarte, J.F., Piccoli, F., Pettke, T., Hermann, J., 2021. Textural and geochemical evidence for magnetite production upon antigorite breakdown during subduction. *J. Petrol.* 62 (10), 1–29. <https://doi.org/10.1093/ptrology/egab053> (in press).
- Vils, F., Pelletier, L., Kalt, A., Müntener, O., Ludwig, T., 2008. The lithium, boron and beryllium content of serpentinitized peridotites from ODP Leg 209 (Sites 1272A and 1274A): implications for lithium and boron budgets of oceanic lithosphere. *Geochim. Cosmochim. Acta* 72, 5475–5504.
- Vils, F., Müntener, O., Kalt, A., Ludwig, T., 2011. Implications of the serpentine phase transition on the behaviour of beryllium and lithium-boron of subducted ultramafic rocks. *Geochim. Cosmochim. Acta* 75, 1249–1271.
- Von Huene, R., Scholl, D.W., 1991. Observations at convergent margins concerning sediment subduction, subduction erosion, and the growth of continental crust. *Rev. Geophys.* 29, 279–316.
- Wakabayashi, J., 2017. Structural context and variation of ocean plate stratigraphy, Franciscan Complex, California: insight into melange origins and subduction-accretion processes. *Progr. Earth Planet. Sci.* 4.
- Whitney, D.L., Evans, B.W., 2010. Abbreviations for names of rock-forming minerals. *Am. Mineral.* 95, 185–187.
- Wheat, C.G., Seewald, J.S., Takai, K., 2020. Fluid transport and reaction processes within a serpentinite mud volcano: South Chamorro Seamount. *Geochimica Et Cosmochimica Acta* 269, 413–428.
- Wu, K., Zhang, L.P., Yuan, H.L., Sun, W.D., Deng, J.H., Zartman, R.E., Guo, J., Bao, Z.A., Zong, C.L., 2021. Boron, arsenic and antimony recycling in subduction zones: new insights from interactions between forearc serpentinites and CO₂-rich fluids at the slab-mantle interface. *Geochim. Cosmochim. Acta* 298, 21–42.
- Wunder, B., Deschamps, F., Watenphul, A., Guillot, S., Meixner, A., Romer, R.L., Wirth, R., 2010. The effect of chrysotile nanotubes on the serpentine-fluid Li-isotopic fractionation. *Contrib. Mineral. Petrol.* 159, 781–790.
- Zhang, L., Sun, W.D., Chen, R.X., 2019. Evolution of serpentinite from seafloor hydration to subduction zone metamorphism: petrology and geochemistry of serpentinite from the ultrahigh pressure North Qaidam orogen in northern Tibet. *Lithos* 346.